SYNTHESIS AND CHARACTERIZATION OF IRON DOPED ZnO NANOPARTICLES VIA SOL-GEL PROCESS FOR POTENTIAL BIO-IMAGING APPLICATIONS

Ayabei Kipyator Shadrack

A Thesis Submitted in Partial Fulfilment of the Requirements for the Degree of Master of Science in Physics of Murang'a University of Technology

August, 2025

DECLARATION

Student Declaration

I hereby declare that this Thesis is my original work, and it has not been presented before for a degree award in this or any other university. I understand plagiarism, and I am aware of the university's policy in this regard. I understand that any false claim in this respect shall result in disciplinary action in accordance with the university's anti-plagiarism policy.

_____ _____

Ayabei Kipyator Shadrack Date

AS402/5002/2023

Supervisor's Approval

The undersigned certify that they have read and hereby recommend for acceptance of Murang'a University of Technology a thesis entitled **"Synthesis and Characterization of Iron Doped ZnO Nanoparticles via the Sol-Gel Process for Possible Bio-Imaging Applications."**

_____ _____

Dr. John Njagi Nguu, Date

Department of Physical and Biological Sciences,

Murang'a University of Technology

_____ _____

Dr. Jatani Ungula, Date

Department of Pure and Applied Sciences,

Kenya Methodist University

DEDICATION

This research is dedicated to Daudi Chelal and Cecilia Cheruiyot for their support and encouragement. To my siblings and friends, for the support, motivation, and inspiration I have received all through. I dedicate this research to you.

ACKNOWLEDGEMENT

I thank God for the grace and strength He has given me throughout the development of this thesis. I would like to thank my supervisors, Dr Njagi John and Dr Jatani Ungula, for their support and guidance. Your knowledge and expertise influenced my research in the right direction. To Dr Sharon Kiprotich, thank you for your guidance and encouragement throughout my studies.

I extend my acknowledgement to the Department of Physical and Biological Sciences at Murang'a University for the technical assistance and for granting me access to various laboratory equipment while working in the laboratory. To my colleagues and friends Nimrod, Bett, Nancy, Joan, Bethwel, James, Kebut, Duncan, R. James Fischer, Oliver, Laura, Flossy, Boniface, Kelvin, Daniel, Emmah, Hillary, Lincoln, Oudu, Evans, Frankline, Lincoln Koech, and Sammy Karani. I want to thank you for your support, love, and understanding during this process.

This thesis represents not only my hard work and dedication but also the collective effort of everyone who has supported me throughout my research. May God bless you.

ABSTRACT

Pure Zinc Oxide nanoparticles (ZnO NPs) have gained considerable attention for nanomedical applications due to their biocompatibility, strong UV emission, and wide band gap. However, their intrinsic limitations, including unpredictable cytotoxicity, low stability in biological environments, and lack of intrinsic imaging capability, restrict their direct application in the field of bioimaging. This work focused on optimizing the synthesis parameters of Iron (Fe) doped ZnO NPs by varying the Fe doping concentration, growth temperature, and Glutathione (GSH) capping concentration to investigate the effects on optical, structural, and photoluminescence properties for their possible use in bioimaging. Iron-doped ZnO NPs were synthesized via the sol-gel technique with Fe doping (0.15 - 0.55% Fe), growth temperature from room temperature (RT) to 95 °C, and GSH capping (0.002 – 0.014 M). X-ray diffraction (XRD) confirmed the retention of a single-phase hexagonal wurtzite structure for all synthesized samples with no secondary phases. At a doping level of 0.45% Fe, the crystallite size was minimized to 22 nm, peak intensity increased, and microstrain decreased, indicating optimum crystallinity. Variation in growth temperature showed sharper peaks and minimal lattice strain at 65 °C. Capping with GSH reduced peak broadening, reflecting enhanced surface passivation. Photoluminescence (PL) spectroscopy displayed near band edge (NBE) UV emission (410-470 nm) across all samples. The intensity of PL was optimized at 0.45% Fe, 65 °C, and 0.008M GSH due to reduced non-radiative recombination. Optical analysis through UV Vis spectroscopy and Tauc analysis revealed a tunable band gap of 3.67 eV for Pure ZnO, narrowed to 3.02 eV at 0.45% Fe and 65 °C, and to 3.0 eV at 0.008M GSH capping, hence improving visible light emission. Fourier transform infrared spectroscopy (FTIR) confirmed the successful incorporation of Fe into Zn-O and Fe-O bonds without any secondary phases. FTIR displayed strong Zn–O stretching (830-915 cm^{-1}) across all concentrations with slight shifts, confirming lattice distortion from Fe^{3+} substitution. No iron oxide peaks appeared, indicating Fe was incorporated without secondary phases. GSH anchoring of the GSH was confirmed by N-H, C=O, and COO- vibrations, which are indicators of strong bonding to the surface of the ZnO and have offered a better stability to the nanoparticles. The overall findings identified the optimum synthesis conditions to be 0.45 % Fe, 65 °C, and 0.008 M GSH capping. The resultant Fe: ZnO NPs are of high crystallinity, low defect density, band gap tunability, and enhanced PL, making them promising candidates for stable, efficient luminescence bioimaging.

TABLE OF CONTENTS

DECLARATION ..... **ii**
DEDICATION ..... **iii**
ACKNOWLEDGEMENT ..... **iv**
ABSTRACT ..... **v**
LIST OF FIGURES ..... **ix**
LIST OF TABLES ..... **xi**
ACRONYMS AND ABBREVIATIONS ..... **xii**
DEFINITION OF OPERATIONAL TERMS ..... **xiii**
CHAPTER ONE: INTRODUCTION **1**
1.1 Background Information of the Study 1
1.2 Statement of Problem 3
1.3 Objectives of the Study 4
1.3.1 General Objective 4
1.3.2 Specific Objectives 4
1.4 Research Questions 4
1.5 Significance of the Study 4
1.6 Scope of the Study 5
1.7 Contribution of the Thesis 5
1.8 Organization of the Thesis 6
CHAPTER TWO: LITERATURE REVIEW **7**
2.1 Introduction 7
2.2 Bioimaging in Nanomedicine 7
2.3 Similar Research in Bioimaging 9
2.4 Zinc oxide (ZnO) and Applications in Bioimaging 10
2.5 Iron as a Dopant in ZnO Nanoparticles 13
2.6 Effects of Iron Doping Concentration on ZnO NPs 14
2.7 Effect of Growth Temperature on Fe: ZnO NPs 15
2.8 Effect of Capping Agents on Fe: ZnO NPs 16
2.9 Synthesis Methods 17
2.10 Characterization Techniques 19
2.10.1 X-ray Diffraction 19
2.10.2 Ultra-Visible Analysis (UV-Vis) 20
2.10.3 Fourier Transform Infrared Spectroscopy (FTIR) 21
2.10.4 Photoluminescence Spectroscopy 22
2.11 Summary 23
CHAPTER THREE: MATERIALS AND METHODS **25**

3.1 Introduction 25
3.2 Materials 25
3.3 Experimental procedure 25
3.3.1 Synthesis of pure Zinc Oxide Nanoparticles 25
3.3.2 Synthesis of ZnO NPs at Varying Doping Concentration of Fe 26
3.3.3 Synthesis of ZnO NPs at Varying Growth Temperatures 26
3.3.4 Synthesis of ZnO NPs and Determining the Effect of Glutathione Concentration 27
3.4 Characterization and Analysis 28
3.4.1 X-ray Diffraction (XRD) 28
3.4.2 Fourier Transmission Infrared Spectroscopy (FTIR) 28
3.4.3 Ultraviolet-Visible Spectroscopy (UV- Vis) 29
3.4.4 Photoluminescence Spectroscopy 29
3.5 Summary 29
CHAPTER FOUR: RESULTS AND DISCUSSION 30
4.1 Introduction 30
4.2 Effects of Varying Doping Concentrations on the Structural and Optical Properties of Fe-doped ZnO Nanoparticles 30
4.2.1 X-Ray Diffraction (XRD) Analysis 30
4.2.2 Estimation of Strain 36
4.2.3 Photoluminescence Spectroscopy 38
4.2.4 Optical Analysis 41
4.2.5 FTIR Analysis 44
4.3 Effects of Varying Growth Temperature on Optical and Structural Properties of Iron-doped Zinc Oxide Nanoparticles 46
4.3.1 XRD Analysis 46
4.3.2 Estimation of Strain and Dislocation Density 49
4.3.3 Photoluminescence Analysis 50
4.3.4 Optical Analysis 52
4.3.5 FTIR Analysis 55
4.4 Effects of Glutathione Concentration Used as a Capping Agent on the Structural, Optical, and Photoluminescence Properties of Fe: ZnO NPs. 57
4.4.1 XRD Analysis 57
4.4.2 Photoluminescence Analysis 62
4.4.3 Optical Analysis 64
4.4.4 FTIR Analysis 67
4.7 Summary 69
CHAPTER FIVE: CONCLUSION AND RECOMMENDATIONS 71

5.1 Conclusion 71
5.2 Recommendations 73
5.2.1 Recommendations for Practice 73
5.2.2 Recommendations for Future 73
5.2.3 Recommendations for Policy 73
REFERENCES 74
APPENDICES 93

LIST OF FIGURES

Figure 2.1: Wurtzite Structure of ZnO with a Hexagonal cell. 11
Figure 2.2: Applications of ZnO NPs in Nanomedicine 12
Figure 3.1: Flow Chart Showing the Experimental Procedure for the Synthesis and Doping of ZnO NPs. 28
Figure 4.1: XRD Pattern for all Synthesized Samples of Fe: ZnO NPs at Varying Doping Concentrations 31
Figure 4.2: Variation of FWHM and Crystallite Size of Synthesized Fe: ZnO NPs at Varying Doping Concentrations. 35
Figure 4.3: (a) XRD most intense peaks at plane (101) of Fe: ZnO NPs. (b)Variation of FWHM and Relative intensity of peaks at varying doping concentrations of Fe: ZnO NPs. 36
Figure 4.4: Variation of Microstrain and Crystallite size of Fe: ZnO NPs at Varying Doping Concentrations. 38
Figure 4.5: Photoluminescence Spectra of Fe: ZnO NPs at Varying Doping Concentrations 39
Figure 4.6: UV-Vis absorbance Spectra of Fe: ZnO NPs at Varying Doping Concentrations 42
Figure 4.7: Tauc Plot of Fe: ZnO NPs Showing Band Gaps as Obtained Through Extrapolation of the Linear Curves. 43
Figure 4.8: FTIR spectra of Fe: ZnO NPs at Different Doping Concentrations. 45
Figure 4.9: XRD Pattern Showing Diffraction Peaks of Fe: ZnO NPs at Different Growth temperatures 46
Figure 4.10: Variation of FWHM and Crystallite size D (nm) of Fe: ZnO NPs at varying growth temperatures. 50
Figure 4.11: (a) Photoluminescence Spectra (PL) of Fe: ZnO NPs at Different Growth Temperatures and (b) Deconvolution of Fe: ZnO at 65 °C 50
Figure 4.12: Ultra Violet Visible (UV Vis) Absorbance Spectra of Fe: ZnO NPs at Varying Growth Temperatures 53
Figure 4.13: Tauc Plot Showing Extrapolated Band Gaps of Fe: ZnO NPs at Different Growth Temperatures 54
Figure 4.14: FTIR Spectra of Fe: ZnO NPs at Different Growth temperatures 56
Figure 4.15: XRD pattern for Fe: ZnO NPs and GSH-capped Fe: ZnO NPs at different GSH concentrations 57
Figure 4.16: Variation of FWHM and Crystallite size at different GSH Capping Concentrations 62

Figure 4.17: (a) PL spectra of synthesized GSH-capped Fe: ZnO NPs at varying GSH concentrations and PL deconvolution at 0.008M GSH capping (b). 64
Figure 4.18: Absorbance spectra of Synthesized GSH-Capped Fe: ZnO NPs at different GSH concentrations 65
Figure 4.19: Tauc Plot and band gap Extrapolation of Synthesized GSH-capped Fe: ZnO NPs 66
Figure 4.20: FTIR spectra of GSH-capped Fe: ZnO NPs at Different Capping Concentrations 68

LIST OF TABLES

Table 4.1: 2θ (Degrees), average d-spacing, and lattice parameters (a and c) of all synthesized samples (Pure ZnO, 0.15%Fe, to 0.55%Fe).....33
Table 4.2: Summarized FWHM (Degrees) of six XRD peaks and corresponding crystallite Sizes D (nm) for all synthesized samples (Pure ZnO, 0.15%Fe to 0.55%Fe). 34
Table 4.3: Variation of crystallite size D (nm) and strain of Fe: ZnO NPs at peak (101).....37
Table 4.4: FWHM and PL peak intensities of Fe: ZnO NPs at varying doping concentrations. 41
Table 4.5: Variation of Doping Concentration and Band Gap Energy of Fe: ZnO NPs 44
Table 4.6: FWHM and crystallite size values of all Fe: ZnO NPs samples at different growth temperatures. 48
Table 4.7: 2θ, d spacing, and lattice parameters a and c values of all planes for Fe: ZnO NPs at different growth temperatures. 48
Table 4.8: Calculated Micro-Strain and Dislocation density at peak (101) for Fe: ZnO NPs at varying Growth temperatures. 49
Table 4.9: Emission Wavelengths and PL Intensities of Fe: ZnO NPs at Different Growth Temperatures 51
Table 4.10: Band gap values of Fe: ZnO NPs at Varying Growth Temperatures 55
Table 4.11: Crystallite sizes, Microstrain, and Dislocation Densities of Synthesized GSH-Capped Fe: ZnO NPs.....59
Table 4.12: Showing lattice Parameters and Average d spacing of GSH-Capped Fe: ZnO NPs.....60
Table 4.13: Showing the Emission Wavelengths and PL intensities of GSH-Capped Fe: ZnO NPs at different GSH Concentrations. 64
Table 4.14: Showing Extrapolated Band Gap Values at each GSH concentration....67

ACRONYMS AND ABBREVIATIONS

CT	Computed tomography
DMS	Diluted magnetic semiconductor
EDX	Energy dispersive X-ray spectroscopy
Fe: ZnO	Iron-doped zinc oxide
FTIR	Fourier transmission infrared
FWHM	Full width at half maximum
GSH	Glutathione
MRI	Magnetic resonance imaging
NIR	Near infrared region
NPs	Nanoparticles
PEG	Polyethylene glycol
PL	Photoluminescence
PVA	Polyvinyl alcohol
PVP	Polyvinyl pyrrolidine
RT	Room temperature
TEM	Transmission electron microscopy
TM	Transition metal
UV-Vis	Ultraviolet-visible spectroscopy
XRD	X-ray diffraction

DEFINITION OF OPERATIONAL TERMS

Synthesis- The process of creating nanoparticles from raw materials using a chemical or physical method, such as gel, hydrothermal, and precipitation. It involves controlling reaction conditions to obtain the desired size, shape, and properties.

Characterization - The set of techniques used to analyze and measure the physical, chemical, optical, and structural properties of nanoparticles, such as XRD for structure, UV-Vis for band gap, and PL for emission properties.

Band Gap- The energy difference between the valence band and conduction band in a material. For nanoparticles, the band gap often changes with size and doping, influencing optical and electronic behavior.

Doping- The intentional introduction of small amounts of foreign atoms (dopants) into the crystal lattice to modify the material's properties, such as its band gap, conductivity, or luminescence.

Capping- The use of a stabilizing agent such as glutathione and citric acid that binds to the surface of nanoparticles during synthesis to control growth, prevent aggregation, and enhance stability.

Strain- The distortion or deformation in the crystal lattice compared to its ideal arrangement. It can be caused by doping, defects, or size effects in nanoparticles.

Crystal Lattice- The regular, repeating arrangement of atoms or ions in a crystalline material, which determines its symmetry and physical properties.

Photoluminescence (PL)- The emission of light from a material after it absorbs photons. In nanoparticles, PL reveals information about band gap transitions, defects, and surface states.

Crystallite Size- The size of a single coherent crystalline domain within a nanoparticle, usually determined from XRD data using the Scherrer equation. It's smaller than the particle size if the particle is made of multiple crystallites.

CHAPTER ONE

INTRODUCTION

1.1 Background Information of the Study

Nanomedicine, as a branch of science, has emerged as of great importance due to its focus on the use of smart materials. Smart materials have been used as modern-day materials for physical therapy, e.g., Hyperthermia, in vivo imaging, and as contrast agents (Kurul *et al.,* 2025). The developed nanomaterials are specifically particles with sizes that range between 1 to 100 nm. Zinc oxide nanoparticles (ZnO NPs) have garnered significant interest over the years with respect to typical NPs due to their distinct properties, such as non-toxicity and biocompatibility (N. Sharma *et al.,* 2016). Such properties have made ZnO NPs suitable for bio-imaging applications. ZnO NPs are considered smart materials since their reduced size makes them invasive to a lesser degree and implantable in the human body. Their physical-chemical properties can be modified to obtain new functionalities (Nguyen *et al.,* 2019). Nonetheless, pure ZnO NPs still lack the intrinsic imaging properties desired in bioimaging and have low stability when subjected to biological and aqueous media, hence fickle cytotoxic effects (Dey *et al.,* 2022)

Recently, researchers have found that the insertion of dopants in the crystalline structure of ZnO is the best way to customize the chemical properties. For example, doping with vanadium, V-doped ZnO NPs, has improved optical properties (Kayani *et al.,* 2020). Therefore, doping with an appropriate transition metal represents a better solution for addressing the limitations shown by the undoped counterpart. Doping has been greatly preferred since the introduction of a transition metal element makes ZnO NPs act like a diluted magnetic semiconductor (DMS) (Seshadri, 2005). Fe as a dopant has been incredibly influential because it exists in two different oxidation states (Fe^{2+} and Fe^{3+}). The two oxidation states play a key role by inducing different effects on electrical and structural properties because of the charge flowing within the system and their difference in ionic radius (George *et al.,* 2010).

Pure ZnO NPs lack intrinsic imaging properties, which are often used in biomedical applications. Doping the crystal lattice improves the corresponding properties by giving proper luminescent properties, and it's been widely applied in magnetic

resonance imaging (MRI) (Y. Liu *et al.,* 2011). Its dissolution in aqueous media is because ZnO dissolves and releases free Zn^{2+} cations, and tuning them by doping with Fe has shown that there is an increase in bactericidal activity of ZnO (Wang *et al.,* 2017). Doping decreases the dissolution rate because there are strong chemical bonds between the host ZnO lattice and the Fe dopant (Wang *et al.,* 2017). In its own pure form, ZnO wide bandgap is about 3.3 eV, meaning it can absorb UV light. Doping can increase the emission rate to the infrared region since Fe, a TM, acts as the optically active impurity (Lin *et al.,* 2006).

At low doping concentrations, ZnO NPs show ferromagnetic behaviour, but at a high doping concentration of Fe, ferromagnetic behavior gets subdued, while a paramagnetic nature is observed (P. K. Sharma *et al.,* 2009). Suppressed ferromagnetism at a higher dopant concentration is due to the enhanced antiferromagnetism interaction between Fe-Fe ions (P. K. Sharma et al., 2009). Particle size and the crystallinity of Fe: ZnO NPs increase with an increase in calcination temperature (Pal Singh *et al.,* 2016). At low temperatures, Fe: ZnO NPs are feebly ferromagnetic with low remanence and coercivity, while at high temperatures, ferromagnetic behaviour is confirmed with an increase in coercivity and remanence (Pal Singh *et al.,* 2016).

Capping agents or surface modifications can conjugate with molecules to avoid NPs aggregation by reducing their size, and morphology, and altering surface chemistry, hence enhancing stability (Javed *et al.,* 2016). Capping agents, divergently, have versatile properties that have been proven to perform an essential role in terms of enhancing the characteristics of NPs in ways that can make them the most suitable in nanomedical applications. When the GSH surfactant layer is more populated, together with a small core size, it stabilizes the NPs in aqueous media where collisions between NPs are reduced to produce a uniform magnetic media (Beato-López *et al.,* 2020). When GSH content is reduced, the relaxation times combined with superparamagnetic blocking temperatures are increased, which is associated with poor NPs stability (Beato-López *et al.*, 2020).

Despite these advances, a clear research gap remains. While Fe doping and GSH capping have individually shown promise in enhancing ZnO NPs' optical and

structural properties, there is limited systematic research combining Fe doping concentration, growth temperature, and capping concentration to maximize photoluminescence efficiency, stability, and bioimaging potential. This gap is particularly significant because current studies either focus on doping without considering temperature and capping effects, or on capping without comprehensive optical optimization. The motivation for this study is to address this gap by systematically investigating the effects of Fe doping concentration, growth temperature, and GSH capping concentration on the structural, optical, and photoluminescence properties of Fe: ZnO NPs. The aim is to identify synthesis conditions that optimize their performance for potential bioimaging applications, contributing new insights to nanomedicine.

1.2 Statement of Problem

Pure ZnO NPs have attracted interest in the field of bioimaging due to their anticancer activity and biocompatibility, and facile synthesis. They can generate reactive oxygen species (ROS) and release Zn^{2+}. These are mechanisms used particularly in antibacterial therapies and chemotherapy. However, they still face critical limitations for bioimaging applications, including poor colloidal stability in biological environments, low photoluminescence, and non-tunable optical properties such as wavelength and band gap.

To address this gap, this research tests these interrelated parameters. First is varying the Iron (Fe) doping concentration, growth temperature control, and surface capping using Glutathione. Doping with transition metals, in this case Fe^{3+}, has been found to be an effective way to tune the band gap of ZnO, as well as increase near band edge (NBE) emission and reduce non-specific dissolution in aqueous media. The temperature at which crystals grow alters the crystallite size, defect concentration, and optical properties, thereby altering the photoluminescence (PL) brightness and wavelength. Surface passivation with GSH, a biocompatible tripeptide containing thiol, amine, and carboxyl functional groups, is able to repress the defect states at the surface, increase colloidal stability, minimize undesired cytotoxicity, and modify the optical transitions.

1.3 Objectives of the Study

1.3.1 General Objective

To synthesize and characterize iron-doped zinc oxide nanoparticles via the sol-gel process for possible bioimaging applications.

1.3.2 Specific Objectives

i. To investigate the effects of varying the concentration of iron as a dopant on the material properties of ZnO NPs for possible bioimaging.
ii. To study the effects of varying the growth temperature on the material properties of Fe: ZnO nanoparticles.
iii. To determine the effects of Glutathione concentration used as a capping agent on the material properties of Fe: ZnO nanoparticles during synthesis.

1.4 Research Questions

i) What is the effect of varying the concentration of Fe as a dopant on the material properties of ZnO NPs?
ii) How does varying the growth temperature affect the material properties of Fe: ZnO NPs?
iii) What are the effects of Glutathione concentration used as a capping agent on the material properties of Fe: ZnO nanoparticles during synthesis?

1.5 Significance of the Study

Since its conception in the last three decades, nanomedicine has progressed significantly in the prevention and treatment of human disease. The focus on this field has resulted in the development of new nanomaterials, nanotherapeutics, and smart materials, which have improved diagnostics, contrast agents, and medical devices (Zhang *et al.,* 2020). Bioimaging helps in nanomedicine by confirming, assessing, and documenting the cause of many diseases, e.g., cancer, and its response to treatment. Being a non-invasive procedure, it aids in giving a bird's-eye view of the human body. The importance of the study is that it has the potential to improve the material properties of pure ZnO NPs by controlled doping with Fe, and growth temperature capping with glutathione. With optimization of these parameters, stable nanoparticles with an optimal photoluminescence and optical band gaps can be made. These are the most wanted properties for bioimaging processes. These developments can result in

more proficient and non-reactive imaging agents in the non-invasive diagnosis of diseases. Also, the discovery can generalize to the advancement of nanotechnology as it provides a flexible synthesis scheme that can be used in other doped metal oxide systems with regard to biomedical and optoelectronic uses.

1.6 Scope of the Study

This work focused on engineering the material properties of iron-doped Zinc Oxide NPs (Fe: ZnO NPs) and their potential applications in bioimaging. It entailed varying the concentration of iron (Fe) from 0.15% Fe to 0.55% Fe, Growth temperature from room temperature (RT) - 25°C to 95°C, and Glutathione (GSH) capping from 0.002 to 0.014 M to investigate their effects on the structural, optical, and photoluminescence properties of ZnO NPs. The growth temperature and GSH capping agent were also varied, and their effects on the material properties of Fe: ZnO NPs were examined. The study focused on finding the optimum conditions for the synthesis of Fe: ZnO NPs to be potentially applied in bioimaging. The study relied only on the data collected in the laboratory and work done by other researchers.

1.7 Contribution of the Thesis

The thesis contributions are highlighted below

i. Optimization of Synthesis Conditions of Fe-Doped ZnO Nanoparticles. The rational optimization gave the optimal synthesis conditions, 0.45% Fe, 65°C during growth, and 0.008M GSH capping, which drastically raised the crystallinity, optical tunability, and the PL intensity of the nanoparticles, rendering them far more useful in the field of bioimaging.
ii. Iron (Fe) Doping improves the structural and Optical properties, which are tremendously effective towards enhancing the structural integrity of ZnO NPs. XRD confirmed this since there were no secondary phases, and PL spectroscopy produced the result through increased near band-edge (NBE) emission, and the band gap was narrower, 3.67 eV to 3.02 eV. The Fe doping contributed to the balance of the defect concentration and crystallinity optimization, which solved the efficiency levels in light emission and lack of absorption bands for bioimaging.
iii. The Impact of nanoparticle stability and PL Performance of GSH Capping. This was based on the importance of GSH capping in increasing the surface stability

and biocompatibility of Fe: ZnO NPs. By finding the optimum capping concentration at 0.008M GSH, the results showed a decrease in defects, an enhanced colloidal stability, and increased PL intensity as a result of defect passivation and prevention of non-radiative recombination. Functionalization was confirmed at N-H, C=O, and COO^-.

1.8 Organization of the Thesis

This Thesis has been organized into five chapters, with the first chapter having the background information, statement of problem, objectives of the study, research questions, significance, justification, scope and limitation, contribution, and organization of the thesis.

Chapter two discusses the literature information of the study, which entails Bio-imaging, Zinc oxide nanoparticles, synthesis methods, iron as a dopant, and methods of characterization.

Chapter three highlights the materials, reagents, and procedure used in this research to obtain the nanoparticles. It also outlines the analysis techniques used.

Chapter four outlines the results per objective as obtained from analysis by XRD, UV-Vis, FTIR, and PL.

Chapter five outlines the conclusion of the study, the recommendations from this particular study, and the future.

CHAPTER TWO

LITERATURE REVIEW

2.1 Introduction

This chapter discusses bioimaging as one of the fields in nanomedicine, similar research that has been done on Fe: ZnO NPs applications in bioimaging. ZnO and its properties for bioimaging application, iron as a potential dopant for ZnO NPs, photoluminescence properties, effects of iron doping, growth temperature, and capping agents on material properties of Fe: ZnO NPs for bioimaging applications.

2.2 Bioimaging in Nanomedicine

Bioimaging is a field of interest in "nanomedicine," which refers to procedures involving tools that enter the body physically and allow researchers to lively observe specific biological processes. In medical sciences, bioimaging is used to investigate the typical anatomy and physiology and assemble research data (Z. Cheng *et al.,* 2024). Medical bioimaging began in the 1890s and has rapidly improved over the last 100 years. MRI and computed tomography (CT) are common biomedical procedures that utilize contrast when taking images of the body (Maysinger *et al.,* 2015). They are mostly carried out since they are non-invasive procedures. In this imaging technique, the part of the body that is underdiagnosis is usually traversed with a beam of wave that carries and reflects the radiation (Z. Cheng *et al.,* 2024). A specific detector is used to arrest the radiation and produce a depiction pattern (Santhi *et al.,* 2016). Cancer is one of the diseases treated by utilizing bioimaging, and it has risen to 2nd as the major cause of death after cardiovascular disease (LeCompte & Brawley, 2023). Due to this, designing policies for imaging in quest is of interest to ensure that there is precise imaging for fruitful cancer management, not only in vitro but in vivo simultaneously. The findings from imaging help in the prevention of diseases like cancer and its complications through early diagnosis to avoid future consequences.

Zinc oxide nanoparticles (ZnO NPs) have been of particular interest due to their high stability, intrinsic photoluminescent properties, non-toxicity, and biocompatibility, which makes them much more attractive to be used in bioimaging. They have a high bandgap of 3.3 eV and a high exciton binding energy of 60 meV, which makes them good UV emitters whose visible light can be tuned by doping. All these characteristics,

in addition to being able to synthesize them at low cost with scalable processes such as sol-gel, make ZnO a favorable candidate compared to other metal oxides in bioimaging. Zinc oxide NPs are potentially suitable for bioimaging applications compared to NPs of other metal oxides due to their high stability and inherent photoluminescent properties (Sahoo *et al.,* 2021). They also have a reduced size with a large surface area to volume ratio (Carofiglio *et al.,* 2020). The above properties make ZnO NPs comparable to most biological system characteristics. Although ZnO NPs are the most suitable for potential bioimaging applications, particle aggregation and the need for cell internalization demand attention (Jha *et al.,* 2023). The use of capping agents to maximize the stability of NPs in dispersion is possibly the right way of addressing it (Fan *et al.,* 2020).

In this work, glutathione (GSH) was selected as a capping agent since it has outstanding biocompatibility, antioxidant capacity, and multifunctional functional groups regardless of its ability to strongly bind to Zn2+ ions on the surface of nanoparticles in terms of the functional group present, including -SH -NH2 -COOH. It is a more favorable capping agent than others because GSH promotes colloidal stability and prevents aggregation, enhances dispersibility in aqueous media, and establishment conjugation of biomolecules to specific targets in bioimaging studies.

Apart from the above-mentioned properties, ZnO NPs can be tuned to improve their material properties. Incorporating a dopant in its crystal lattice is a valuable path to tune ZnO NPs' properties. Iron is the most suitable impurity due to its two oxidation states that induce distinct effects on the existing structural properties of ZnO NPs (Rosowska *et al.,* 2020). This work varied the concentration of iron and investigated the effect it has on the material properties of Fe: ZnO NPs.

Growth temperature is an important synthesis parameter because it affects nucleation, crystallinity, defect density, and particle size, which further affect photoluminescence intensity, emission wavelength, and bandgap tuning. By analyzing temperature fluctuation, the best growth conditions to achieve the highest PL emission and structural stability for bioimaging purposes can be determined.

2.3 Similar Research in Bioimaging

Liu et al., 2010 utilized the facile sol-gel method to dope Nd^{3+} into the hexagonal ZnO nanocrystals. This optimized their optical properties by exhibiting a sharp and intense new infrared region (NIR) luminescence of Nd^{3+}. They discovered that the Nd^{3+} ions can be effectively sensitized by ZnO nanocrystals, which improves their photoluminescence for use in optoelectronic devices. However, this previous work did not explore the effect of capping, the impact of aqueous synthesis conditions, and the influence of the optical and surface properties of ZnO NPs for bioimaging applications.

Sun *et al.,* 2021, doped zinc gallate (ZnGa2O4) with chromium (ZGC NPs), and their investigation showed that the NPs emission of NIR light continued for a long time. They noted that it was due to NIR persistent luminescent nanoparticles (PLNPs), which are the optical probes that can emit NIR light for an extended period even after the illumination of light has been stopped. The conclusion was that ZGCs were more versatile than their undoped counterparts in the field of high-sensitivity biosensing and bioimaging. Moreover, PLNPs can prevent autofluorescence completely, which is usually caused by light excitation, and as a result, improve the sensitivity of biosensing and bioimaging. (Kumawat *et al.,* 2022) synthesized and doped ZnO NPs with Europium (Eu) via the sol-gel process and co-precipitation, and discovered that Eu: ZnO NPs showed a band gap diminution due to the enhanced carrier impurities within the system. The NPs' blue emission in the photoluminescence (PL) spectra is enhanced with the integration of Eu in the crystal lattice of ZnO. A decrease in temperature leads to PL enhancement in intensity in the NPs with respect to the pure material. The change from horizontal to vertical nanostructures also resulted in PL enhancement. They concluded that the enhancements of the PL emission peak of ZnO NPs within the blue region are due to induction by Eu doping and thus contribute widely to bioimaging applications. Although both works demonstrated the influence of Eu^{3+} and Cr^{3+} doping on the optical properties of ZnO NPs, neither explored the effects of GSH capping and doping with Fe^{3+} in the modification of surface and optical properties of ZnO NPs for bioimaging applications. In another study, (Chen *et al.,* 2022) worked on the biodegradable sol-gel derived Erbium-doped Er: ZnO NPs for cell imaging. Their investigation utilized 5 % mol rare earth Er as the dopant with polyethylene

glycol surface modification via the sol-gel technique. They investigated their biodegradation behavior and specific fluorescence characteristics and discovered that the visible PL of Er: ZnO NPs is greatly improved compared to the undoped counterpart. After storing for a month, their variation in terms of particle size becomes less than 1nm, and their performance in fluorescence is retained. Their cytotoxic degradation showed that they are biocompatible and degradable, thus being used extensively in cell imaging. However, this work didn't explore the use of Fe as a dopant for ZnO NPs and the impact it has on defect formation and PL behavior with the help of a capping agent, which could aid in bioimaging applications.

Although other studies have already established that doping of ZnO NPs with rare-earth and transition metals can improve the photoluminescence of these NPs to achieve bioimaging, little has been done to show the combination of Fe doping and the systematic optimization of growth temperature, as well as GSH capping of the NPs. The interaction of the three parameters has not been exhaustively studied to achieve the greatest output of PL, stability, and control of the bandgap. This paper fills that void by bringing additional information to the Fe: ZnO NPs development to be used in bioimaging.

2.4 Zinc oxide (ZnO) and Applications in Bioimaging

ZnO is a n-type semiconductor material having a wide band gap of 3.37 eV at room temperature (RT) (Djurišić *et al.,* 2010). It has a high binding energy exciton of 60meV and displays two emission bands in the ultraviolet and visible regions at RT (Murkute *et al.,* 2019). ZnO's first ultraviolet emission is at 375 nm, and its extensive green emission spectral range is from 480 nm to 560 nm (Musa *et al.,* 2017). Zinc Oxide, under normal conditions, crystallizes in the wurtzite structure, displaying a hexagonal cell (Musa *et al.,* 2017) as shown in Figure 2.1. In this structure, the Zn atom has four oxygen atoms that surround it, and they are situated within the corners of a regular-shaped tetrahedron. Zinc Oxide spacing along the c-axis is moderately short compared to that of other Zn-O bonds. ZnO has a density of 5.6 g/cm^3 and a melting point of 1975°C (Mahmood *et al.*, 2016).

The choice of ZnO over other metal oxides in the study is based on its unique combination of characteristics preferred in bioimaging. One is its large direct bandgap

of 3.3 eV with a high exciton binding energy of 60 meV, which allows for strongly visible and tunable photoluminescence of ZnO or its composites. ZnO is also non-toxic and biologically compatible compared to other semiconductors like CdSe and PbS quantum dots in use. It is also an excellent chemical stability and environmental safety; these benefits place ZnO above other transition metal oxides, e.g., TiO_2, CeO_2, and Fe_2O_3, as a prime target in the production of safe and effective nanoparticles for bioimaging.

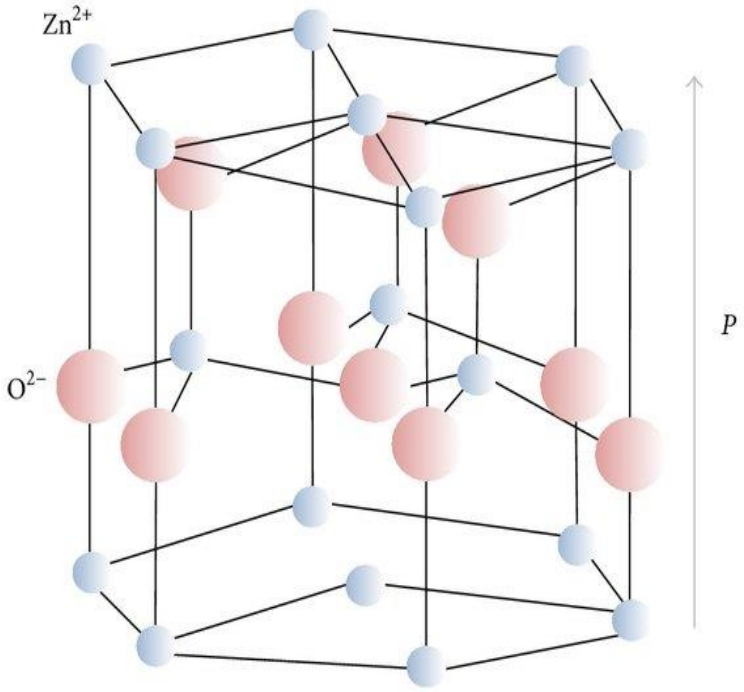


Figure 2.1: Wurtzite Structure of ZnO with a Hexagonal cell.

Source: (Mahmood *et al.,* 2016)

ZnO has been studied extensively for bioimaging and other nanomedicine applications, as shown in Figure 2.2, because its NPs are biocompatible, and due to this property, ZnO NPs have displayed a therapeutic mechanism against various microbial infections, diabetes, cancer, and inflammation (Deka *et al.,* 2022). It is also applied in imaging tools and sensors for potential aid in wound healing (Deka *et al.,* 2022).

For bioimaging and other biomedical technologies, pure ZnO NPs are fabricated through synthesis procedures that control certain defects and bring about the n-type conductivity.

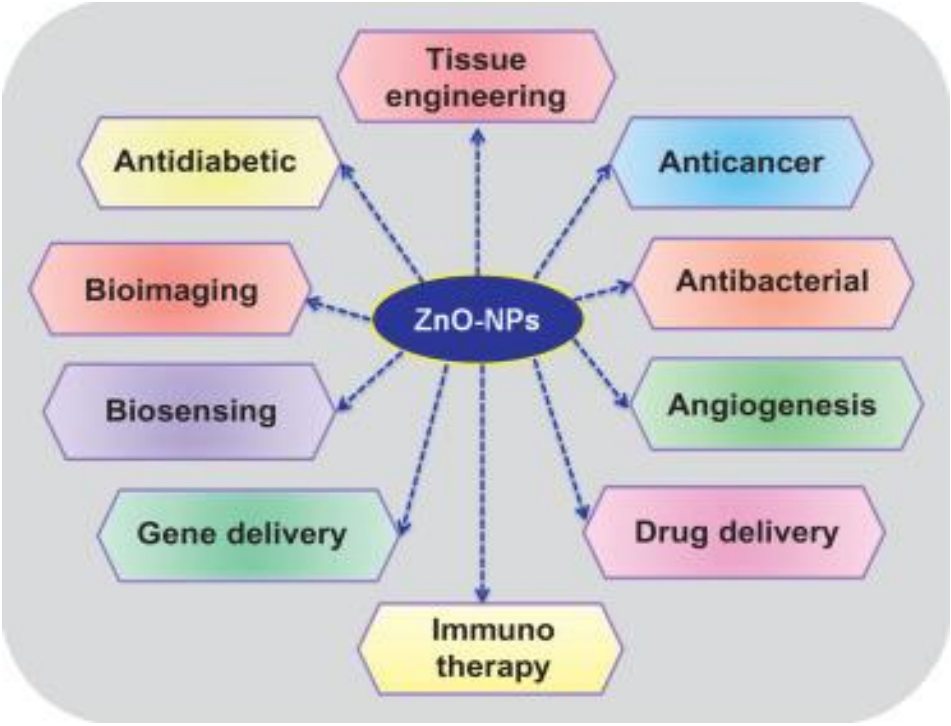


Figure 2.2: Applications of ZnO NPs in Nanomedicine

Source: (Carofiglio et al., 2021)

The procedure reduces the NPs band gap to 3.1 eV and generates a stronger emission from violet to the blue region at the same time, while minimizing defects, specifically those responsible for broad green emissions that are commonly observed (Eixenberger *et al.,* 2019). Moreover, (Zhu *et al.,* 2016) discovered that ZnO is applied in biosensors where an electrode architecture with a single-crystalline nanorod is directly grown on a metallic substrate. This particular substrate is aligned in one-dimensional ZnO nanostructures, providing not only large areas of scaffolds, which are regions for enzyme immobilization, but also direct routes for the transport of electrons to the current collector initially from redox enzymes. Through electrostatic interaction, ZnO nanostructures absorb proteins with low isoelectric points because they have high isoelectric points of 9.5 (Zhu *et al.,* 2016).

ZnO PL spectra have peaks at a wavelength of 407 nm, and they originate from a reintegration of the free excitations between the exciton–exciton interaction mechanism, or can occur because of intrinsic defects like zinc and oxygen interstitials simultaneously (Taunk *et al.,* 2015). ZnO exhibits an extensive blue emission of 484 nm, which is basically attributed to the recombination of radiation in the hole that is photo-generated by the electron that occupies the particular oxygen vacancy. Other factors include the surface states and the recombination of excited holes and electrons (Taunk *et al.,* 2015).

Under light irradiation, the lower intensity of PL shows that there is a lower rate of reintegration of electrons and holes, while a higher PL intensity shows that there is a higher integration rate of holes and electrons. The defects in the surface and sub-surface of ZnO are caused by their quick reaction formation process, combined with a large surface-to-volume ratio (Taunk *et al.,* 2015). Its PL spectra at RT have a UV emission at 3.31 eV combined with a green emission of 2.21 eV (Viswanathamurthi *et al.,* 2003). Both emissions are attributed to the near band-edge transition, joined with its radial combination with the only one ionized vacancy of oxygen that has a photo-induced hole (Viswanathamurthi *et al.,* 2003).

ZnO experiences both edge and green luminescence. The introduction of impurities like Magnesium (Mg) and Gallium (Ga) shifts the ZnO fundamental edge absorption towards the spectral range of shorter wavelengths (Gorokhova *et al.,* 2008). The edge luminescence (380-390 nm), which is linked to exciton-exciton states, is displayed near the UV spectral range with subnanosecond deexcitation moments. With the introduction of an iron impurity, the edge luminescence decay period is reduced to tens of picoseconds, and the maximum edge luminescence position varies depending on the free carrier concentration and the type of impurity used. These ZnO luminescence properties are dependent on the ideality of the crystal structure and the content of the numerous defects in the crystal (Rodnyi & Khodyuk, 2011).

2.5 Iron as a Dopant in ZnO Nanoparticles

Iron is a chemical element represented by the symbol Fe (*ferrum* in Latin). Its atomic number is 26. Fe is a metallic element and is located in the first transition series, and it is one of the group VIII elements in the periodic table. By mass, Fe is the most

common element on Earth, hence forms most of the Earth's inner and outer core. Iron is the fourth element in terms of being common on the Earth's crust since it is deposited mainly in a metallic state by meteorites. It is a ductile, lustrous, malleable, and silver-gray metal that exists in four different crystalline forms. As a dopant in metal oxide nanoparticle semiconductors such as ZnO, it is an important component because of its wide range of chemistry and its capacity to exist in two oxidation states, Fe^{2+} and Fe^{3+}. Doping of zinc oxide with iron may severely change the structural, optical, and electronic characteristics of the nanoparticle. The doping of Fe into the ZnO creates localized energy levels inside the bandgap that have an effect on the material properties in terms of photoluminescence, electrical conductivity, and magnetism. The changes are essential to optimize the functioning of ZnO nanoparticles, especially bioimaging, in which optical and magnetic characteristics play a central role. Nanoparticles of Fe-doped ZnO (Fe: ZnO) have attracted interest because of the possibility to enhance the photoluminescence of ZnO, resulting in higher imaging contrast and sensitivity. Also, Fe: ZnO nanoparticles can be functionalized, as this results in nanoparticle systems applicable in magnetic resonance imaging (MRI) applications, and also in drug delivery applications where the drug is delivered to a specific area by using the magic of magnetic attraction, as a result of iron being magnetic.

2.6 Effects of Iron Doping Concentration on ZnO NPs

ZnO NPs have offered a number of applications in multiple fields, like energy harvesting and nanomedicine (Jiang *et al.,* 2018). Doping has been utilized particularly to minimize the mentioned limitations of ZnO NPs since it has the ability to tune its properties. Doping is an approach where an impurity is introduced into the crystal lattice of a particular material. This method modulates NPs' response electrochemically and tunes their degradation in aqueous media (Carofiglio *et al.,* 2020).

Iron, a D-block element, modifies the properties of ZnO NPs. Its ferromagnetic nature is displayed when it interacts with the crystal lattice of ZnO (Carofiglio *et al.,* 2020). The electronegativity, ionic radius, and different oxidation states of iron can modify the electrical and optical properties of ZnO NPs. This approach of doping with iron

enhances the electrochemical response and stabilizes ZnO NPs. The electrical and structural properties of NPs are tuned by the two oxidation states of iron (Fe^{2+} and Fe^{3+}) because of the presence of charge carried in the system (Carofiglio *et al.,* 2020). When Silicon (Si) is doped with iron, its NPs depict strong photoluminescence and quantum yield in water, which has a notable contrast (Singh *et al.,* 2012). In the case of other compounds like calcium phosphates, in particular hydroxyapatite (HA), Iron as an impurity has a significant effect on NPs morphology. However, Fe^{3+} an oxidation state of iron, disrupts the apatite lattice, hence limiting its potential bioimaging in bioimaging (Pupilli *et al.,* 2024).

2.7 Effect of Growth Temperature on Fe: ZnO NPs

Different growth temperatures have a different impact on ZnO NPs; a change is observed in crystallinity, particle size, and their optical properties when the growth temperature is increased from 65 °C to 75 °C. (Manzoor *et al.,* 2015). A small nucleation time offers a better control of size distribution, although crystallinity gets compromised due to the faster growth dynamics at high temperatures, which introduces defects that decrease the crystal quality (Flannigan *et al.,* 2023).

Annealing temperatures also affect ZnO NPs, If the annealing temperature is increased with increasing crystallite size, and the micro-strain is decreased due to lattice relaxation, then agglomeration combined with an increasing particle size is observable with increasing temperature because of the high nucleation rate at a higher temperature (Ayon *et al.,* 2023). Also, the best photocatalytic performance of the NPs is depicted at higher temperatures of about 500 °C because of the uniformity and the high surface area of the small-sized NPs (Saha *et al.,* 2024)

ZnO NPs that are synthesized by using the sol-gel technique and then dried at 100 °C overnight, followed by further annealing in an air atmosphere at 350 °C for crystallization, form a hexagonal crystalline phase. These NPs display an optical band gap that is about 3.01 eV (Radoń *et al.,* 2017). The PL emission strong band is manifested in the sample in the visible region at 512 nm. Annealing at this high temperature of 350 °C not only enhances the crystalline quality but also removes impurities (Rathore *et al.,* 2024). This is aimed at varying the growth temperature of

Fe: ZnO NPs before introducing Glutathione for better control of the crystal structure and size of NPs, hence better interaction with GSH (Rizwan *et al.,* 2019).

2.8 Effect of Capping Agents on Fe: ZnO NPs

A capping agent or a stabilizer refers to a chemical that offers a coating of protection to the NPs in various media. It is essential in NP production because it ensures there is an enhancement of performance biologically by reducing toxicity and improving therapeutic effectiveness in biological cells (Bahari *et al.,* 2023). Capping agents do so by averting the aggregation of NPs and ensuring there is maximum colloidal stability, therefore avoiding unbridled growth of NPs (Restrepo & Villa, 2021).

Capping agents such as polyethylene glycol (PEG) and polyvinyl pyrrolidine (PVP) enhance the capabilities due to the functional group present at the surface(Javed et al., 2016). Antioxidant activities are higher in capped ZnO NPs with PEG and PVP than in their uncapped counterparts. The antioxidant activity is due to the molecular presence of the ester and carbonyl groups. The capping agents above play a key role in affecting biological activities by modifying the surface area and size (Akhil *et al.,* 2016). In another study, (Teodorescu *et al.,* 2018) concluded that polyvinyl alcohol (PVA), which is produced by the hydrolysis of polyvinyl acetate, is one of the best stabilizing agents. This is because being a synthetic polymer, it has effective biocompatibility combined with good hydrophilicity and biodegradability. It stabilizes the shape and size of NPs and protects them from agglomeration in aqueous media.

Honey is another capping agent with reducing and stabilizing properties on ZnO NPs (Bahari *et al.,* 2023). Honey is composed of groups of carbohydrates, amino groups, enzymes, vitamins, and hydroxide groups that help to complex zinc cations (Zn^{2+}) back to their initial molecular matrix (Molla *et al.,* 2025). The structure enables ZnO NPs to be coated and stabilized, hence preventing exorbitant crystal formation and agglomeration. The organic components of honey are the ones responsible for stability because they stick to the surface of NPs and prevent agglomeration (Bahari *et al.*, 2023). However, there is a need to study the reaction steps involved and the particular compounds responsible. This work employed Glutathione as a capping agent and varied its concentration for possible application in bioimaging.

2.9 Synthesis Methods

Green synthesis is one of the methods of synthesizing ZnO NPs, this method utilizes plant extracts for synthesis. Green synthesis is linked with large-scale production due to its compatibility with pharmaceutical applications, and it's also easy to access the required plant material at a low cost. However, this method offers limited control over the particle size and shape of NPs due to the complex nature of the biological components used. It is also variable and gives inconsistent results since the main components used are plant extracts, which vary in terms of growth conditions and species (Perveen *et al.,* 2020).

Chemical co-precipitation technique can also be used to synthesize Fe: ZnO NPs, it is a wet bottom-up chemical precipitation process that involves hydrolysis and an oxidizing process. The precursor solutions are mixed with stoichiometries proportions under strong stirring. The resulting precipitates are filtered and washed thoroughly, followed by drying at ambient temperature in air so that the obtained NPs are in powder form. The synthesized powder is calcined under normal atmospheric conditions (N. Sharma *et al.,* 2016). This method is scalable, hence it can be used for large-scale production and can produce NPs of high purity. However, there's agglomeration during synthesis affecting the properties of NPs produced, and this type of synthesis is also sensitive to reaction parameters like temperature and pH, demanding precise control in synthesis(Yadav *et al.,* 2018).

Solution chemical method is another method that can be used to synthesize Fe: ZnO NPs. This technique involves three different compounds as precursors. The parameters like pH and concentration of the solution formed are adjusted to favour the process. It is then refluxed at a certain temperature before drying. Freeze-drying and filtration procedures are applied in drying the synthesized samples. The resulting mixed solution is divided into two parts before drying. One part is washed with alcohol and dried using an oven at RT, while another part is submitted to a freeze dryer, where it is dried at RT Calcination of Fe: ZnO NPs is carried out at high temperatures (Wiengnon & Anuragudom, 2019). Although this method is versatile, homogeneous, and offers control of NPs properties like morphology and size, it is still a complex

method of synthesis that is time and energy-consuming because of the high temperatures required (Yadav *et al.,* 2018).

This study employed the sol-gel process to synthesize ZnO NPs. Sol-gel process is one practical method of synthesis and is regarded as the simplest because it can regulate particle size and morphology of NPs by monitoring reaction variables like temperature (Hasnidawani *et al.,* 2016). The sol-gel was beneficial due to its good size distribution of NPs, crystal shape control, low defects, and its ability to synthesize large crystals with high quality.

As shown in Figure 2.3, the sol-gel technique involves the following steps;

The first step involves the sol formation, where the precursor is hydrolyzed in water or ethanol for synthesis. An acid or base can be utilized in hydrolysis in place of water and alcohol. The amount of water used strongly affects the formation of the gel. A high water content leads to the generation of a high ratio of bridging (Parashar et al., 2020).

The second step involves the condensation of molecules, where water or alcohol is eliminated, and the linkage of ZnO is formed. Condensation occurs through the olation and oxolation processes, where hydroxyl and oxo bridges are involved, respectively. It results in an increase in the solvent viscosity, bringing about the formation of a porous structure (Schubert, 2015).

The third step involves aging of NPs; this process generates a continuous structural change and also changes the properties of the gel. As aging takes place, condensation occurs on the localized solution along the gel. This leads to an increase in thickness while porosity is decreased in the middle of colloidal particles (Parashar *et al.,* 2020).

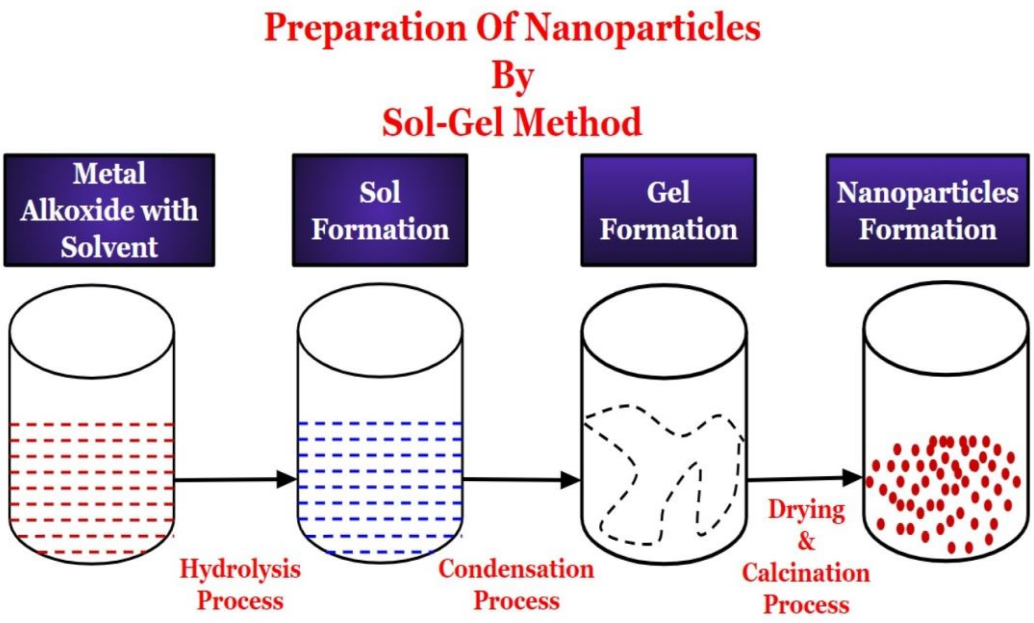


Figure 2.3: Steps in the Sol-Gel Technique

Source: (Bokov *et al.,* 2021)

The fourth step is drying, freeze drying, or thermal drying can be employed, each having different effects on the gel network. Lastly, Calcination is done so that the water molecules and residues are driven off the sample desired. Calcination temperature is an important parameter in the regulation of the pore size of NPs (Parashar *et al.,* 2020).

2.10 Characterization Techniques

Characterization of NPs is carried out after synthesis by utilizing several techniques: X-ray diffraction (XRD), Transmission electron microscopy (TEM), Photoluminescence spectroscopy, Ultra-visible analysis (UV-Vis), and Fourier transform infrared spectroscopy (FTIR).

2.10.1 X-ray Diffraction

X-ray diffractometer shown in Figure 2.4 is used to characterize the structure of ZnO NPs. It involves having the X-rays produced illuminate the sample, diffracted by the phase sample, and enter the detector. By moving the tube or sample detector to change the angle of diffraction, the intensity gets registered, and diffraction data is recorded

(Fakhari *et al.,* 2019). Once the patterns of Fe: ZnO NPs are recorded, the average crystalline size (D) of the synthesized NPs is calculated using the Scherrer formula

$D = k\lambda/B\ cos\theta$ where B is the full-width half maxima of the diffraction peak, θ is the Bragg's peak angle, and λ is the wavelength (N. Sharma et al., 2016).



Figure 2.4: ARL Equinox 100 X-Ray diffractometer (XRD) at Murang'a University of Technology.

2.10.2 Ultra-Visible Analysis (UV-Vis)

Ultraviolet visible (UV-Vis) spectroscopy, shown in Figure 2.5, is an efficient tool employed in quantifying how different wavelengths of light are absorbed, transmitted, or reflected through a sample. Under the method, the sample is compared to a blank sample to rate the extent of light that is absorbed or passes through a series of wavelengths. The optical properties of NPs can be vitally important in the information dispensed by the UV-Vis absorption spectra. In particular, the absorbance marks one of the main parameters since it provides information on the shift in the energy bandgap of the doped ZnO NPs. Nevertheless, the transmittance and reflectance could be determined with the help of the UV-Vis spectroscopy as well, thus complementing the knowledge of the optical properties (Ji *et al.,* 2018). Transmittance is used to measure the fraction of the light that enters the sample, and reflectance is applied to measure the light that reflects off the surface of the sample. Shifts in the absorption peak of

UV-Vis spectra can be observed in the case of doping ZnO NPs, and it pertains to changing the bandgap due to the effect of the said doping. The above changes are essential since they bestow comprehension of the impact of dopants on the optical behavior of ZnO NPs, which is concerned with the capacity of the material to absorb and reflect light of varied wavelengths. Focusing on the impact of doping on the electronic and optical characteristics of ZnO NPs and the possible applications such an approach has, including bioimaging, UV-Vis spectroscopy, becomes an imperative tool to use (Fathima *et al.,* 2020).



Figure 2.5: Evolution one plus UV-Vis spectroscopy at Murang'a University of Technology

2.10.3 Fourier Transform Infrared Spectroscopy (FTIR)

This technique is utilized in analysis to identify chemical and functional groups. It utilizes infrared light for scanning the test samples and observing chemical properties. FTIR as shown in Figure 2.6 works by transmitting infrared radiation within the sample, with some getting absorbed and the remaining radiation passing through. Radiation absorbed is transformed into vibrational or rotational energy by the molecules within the sample.

The signal that results at the detector displays a spectrum that is linked to the molecular sample's fingerprint. Each molecule within the sample generates a unique spectral fingerprint, and thus FTIR analysis is a great method for chemical identification. FTIR can also be used to identify and characterize unknown samples, identify any contaminants in materials, and identify oxidation and decomposition in samples. When ZnO NPs undergo calcination at different temperatures, their size distribution and morphology show that NPs grow as the temperature increases. Moreover, both the circular and hexagonal shapes are depicted by ZnO NPs at 500 °C – 600 °C (Zak *et al., 2011)*. At 700 °C, ZnO NPs become hexagonal in shape. All the above-mentioned characterization techniques show that ZnO NPs, when calcined at varied temperatures, exhibit a hexagonal wurtzite structure.

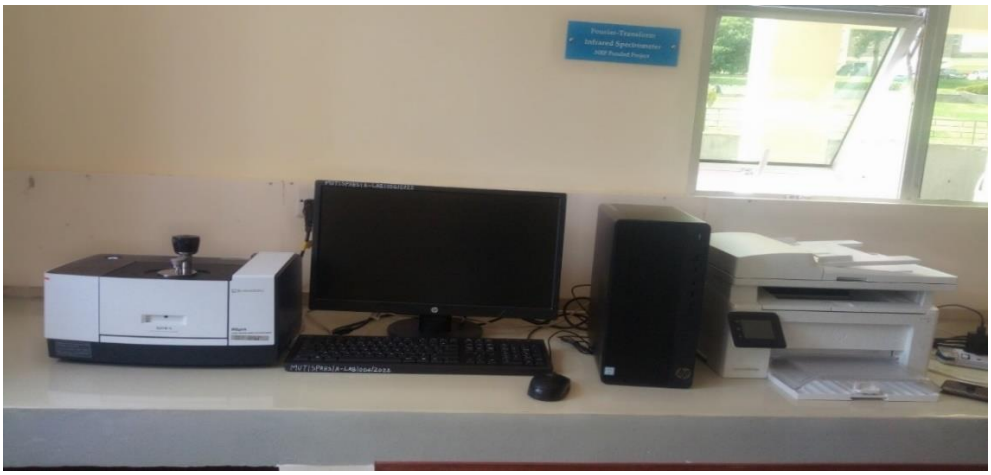


Figure 2.6: IR spirit Shimadzu Fourier Transform Infrared (FTIR) spectrophotometer at Murang'a University of Technology.

2.10.4 Photoluminescence Spectroscopy

Photoluminescence (PL) spectroscopy, as shown in Figure 2.7, is a technique that aids in learning about the light emitted by semiconductor nanoparticles. In this work, PL was employed to investigate the luminescence properties of iron-doped zinc oxide (Fe: ZnO) nanoparticles.

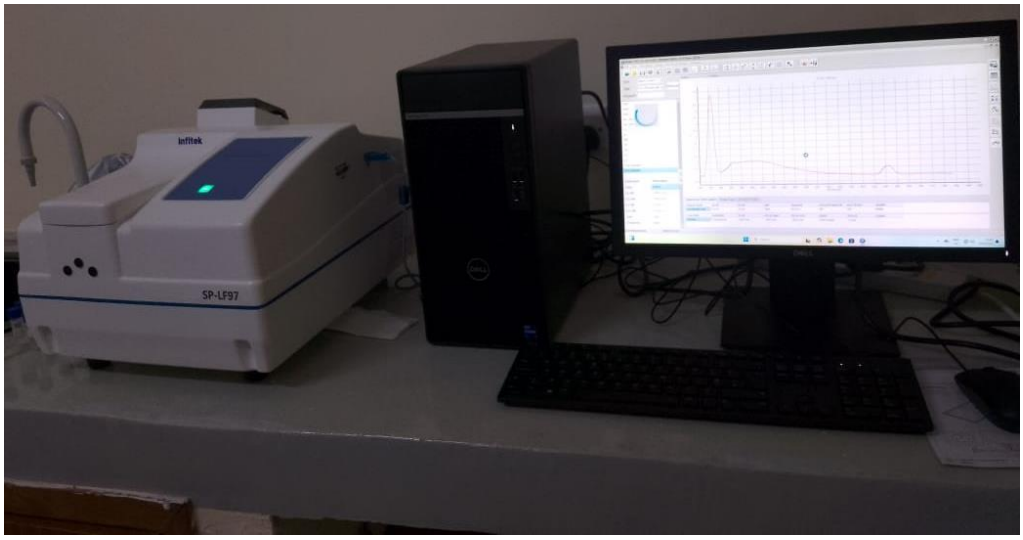


Figure 2.7: SP-LF97 model PL Spectroscopy at Murang'a University of Technology

The PL spectrometer relies on a laser or xenon lamp to illuminate the nanoparticle sample. By applying the excitation, electrons rise to higher energy levels (Jagannatha Reddy *et al.,* 2011). When electrons return to their starting position, they release photons that the spectrometer records and examines. The light emitted is spread through a monochromator and measured by a photomultiplier tube or a charge-coupled device (CCD) detector, resulting in a spectrum that displays the wavelengths and how strongly they are emitted. It provides information about the nanoparticles' bandgap energy, the way their crystals are formed, and any flaws in these crystals. Using PL analysis, we can measure the impact of iron doping on the luminescence emission, looking for changes in peak positions, intensity, and appearance of bands related to defect structures.

2.11 Summary

This chapter reviews bioimaging in nanomedicine with a focus on iron-doped zinc oxide nanoparticles (Fe: ZnO NPs) as promising agents due to ZnO's high stability, photoluminescence, biocompatibility, and low toxicity. It highlights the advantages of using glutathione (GSH) as a capping agent to enhance nanoparticle stability, dispersibility, and functionalization for targeted imaging. While previous studies have explored rare-earth and transition-metal doping in ZnO NPs, gaps remain in combining Fe doping, growth temperature optimization, and GSH capping to improve

photoluminescence, stability, and bandgap control. The review outlines ZnO's structural and optical properties, the role of Fe in modifying electronic, optical, and magnetic characteristics for enhanced imaging and potential MRI or drug delivery applications, the impact of synthesis temperature on crystallinity and emission, and the use of capping agents to prevent aggregation. It also compares synthesis methods, selecting the sol–gel process for its control over particle size and defect reduction, and describes characterization techniques including XRD, UV-Vis, FTIR, and PL spectroscopy for evaluating structural, optical, and surface modifications. The chapter positions the current study as addressing the unexplored interaction between Fe doping, growth temperature variation, and GSH capping to optimize Fe: ZnO NPs for bioimaging applications.

CHAPTER THREE

MATERIALS AND METHODS

3.1 Introduction

This chapter outlines the materials and reagents used, their purity, and the laboratory apparatus used. It also outlines the procedure used to synthesize Fe: ZnO NPs per objective and measurements used. It also summarizes the characterization techniques used during the analysis of the samples.

3.2 Materials

To synthesize and dope ZnO NPs using Iron, the following materials were used;

- Zinc acetate dihydrate (Zn $(CH_3COO)_2 \cdot 2H_2O$ (99.9%) as a precursor
- Iron (III) nitrate nanohydrate Fe $(NO_3)_3 \cdot 9H_2O$ (98%) as the source of Iron ions (Fe^{3+})
- Deionized water for dilutions
- Sodium hydroxide (NaOH) 99.9%
- Ethanol for dissolution
- Diethanolamine (DEA) (99.3%) as a complexing agent
- Glutathione (GSH), all supplied by Sigma Aldrich.

Deionized water was prepared in the Murang'a University of Technology research laboratory. All reagents were of analytical grade and were used directly without any special treatment. Laboratory equipment, including beakers, a pH meter, a measuring cylinder, and a stirring plate, was used.

3.3 Experimental procedure

3.3.1 Synthesis of pure Zinc Oxide Nanoparticles

To prepare pure ZnO NPs, the procedure from (Vishwakarma, 2020) was adopted with few modifications. The first step was sol formation, where 4.4 g of Zinc acetate dihydrate (Zn $(CH_3COO)_2 \cdot 2H_2O$) was dissolved in 100 mL of ethanol, followed by the addition of 2 mL Diethanolamine (DEA) and mixed with a magnetic stirrer for 1 hour. The second step was condensation, where 0.8 M Sodium hydroxide solution was added dropwise using a burette into the flask containing zinc acetate and ethanol for 1

hour under continuous stirring. The white suspension formed after NaOH was added was kept under continuous stirring at 65 °C for 2 hours. The sample was aged overnight at RT until a gel-like solution was formed. Finally, the sample was rinsed several times with DI water and dried in an oven at 100°C for 2 hours, and finally annealed at 500 °C for 1 hour. The sample was ground into fine NPs and kept in a sample holder for further analysis.

3.3.2 Synthesis of ZnO NPs at Varying Doping Concentration of Fe

Sol-gel technique was adopted from (Vishwakarma, 2020) to synthesize Fe: ZnO NPs by adding 4.4g of Zn $(CH_3COO)_2 \cdot (H_2O)$ to 100ml of ethanol in a clean beaker on a magnetic stirrer at room temperature. 2 mL of DEA was added after 15 minutes, and stirring continued until a transparent solution was formed. Various % moles of Fe (0.15, 0.20, 0.25, 0.3, 0.35, 0.4, 0.45, 0.5, 0.55) were added at a time, and stirring was continued for 30 minutes. 1.6 M NaOH was added dropwise using a burette to adjust the pH to 11 with the aid of a pH meter. The contents were then transferred to a hot magnetic stirrer set at 65 °C, and heating took place for 2 hours, where a gel-like solution was formed. The solution was covered in a clean foil and left to age overnight. The gel was rinsed several times with DI before drying in an oven at 100 °C for 2 hours to eliminate residual solvents and finally annealed in a muffle furnace at 500 °C for 1 hour. The sample was ground into fine NPs and kept in a sample holder for further analysis.

3.3.3 Synthesis of ZnO NPs at Varying Growth Temperatures

Synthesis of Fe: ZnO NPs was carried out by adding 4.4 g of Zn $(CH_3COO)_2 \cdot H_2O$ to 100 mL of ethanol in a clean beaker on a magnetic stirrer at room temperature. After 15 minutes, 2 mL of DEA and stirring continued until a transparent solution was formed. 0.45% Fe was added, and stirring was continued for another 30 minutes. 1.6 M NaOH was added dropwise using a burette to adjust the pH to 11 with the aid of a pH meter. The contents were then transferred to a hot magnetic stirrer set at RT as the first growth temperature, and heating took place for 2 hours, where a gel-like solution was formed. The solution was covered in a clean foil and left to age overnight. The gel was rinsed several times with DI before drying in an oven at 100 °C for 2hr to eliminate residual solvents and finally annealed in a muffle furnace at 500 °C for 1

hour. The sample was ground into fine NPs and kept in a sample holder for further analysis. The procedure was repeated for other growth temperatures (35, 45, 55, 65, 75, 85, 95 °C).

3.3.4 Synthesis of ZnO NPs and Determining the Effect of Glutathione Concentration

To synthesize Fe: ZnO NPs and GSH-capped Fe: ZnO NPs, 4.4 g of Zn $(CH_3COO)_2 \cdot H_2O$ was added to 100 mL of ethanol in a clean beaker on a magnetic stirrer at room temperature. DEA (2 mL) was added after 15 minutes, and stirring continued until a transparent solution was formed. 0.45% Fe was added, and stirring was continued for another 30 minutes. 0.002 M GSH was added and allowed to dissolve for 15 minutes. 1.6 M NaOH was added dropwise using a burette to adjust the pH to 11 with the aid of a pH meter. The contents were then transferred to a hot magnetic stirrer set at 65°C, and heating took place for 2 hours where a gel-like solution was formed. The solution was covered in a clean foil and left to age overnight. The gel was rinsed several times with DI water before drying in an oven at 100 °C for 2hr to eliminate residual solvents and finally annealed in a muffle furnace at 500 °C for 1 hour. The sample was ground into fine GSH-capped Fe: ZnO NPs and kept in a sample holder for further analysis. The procedure was repeated for other GSH concentrations (0.002, 0.004, 0.006, 0.008, 0.010, 0.012, and 0.014 M)

The steps for synthesis are shown in Figure 3.1

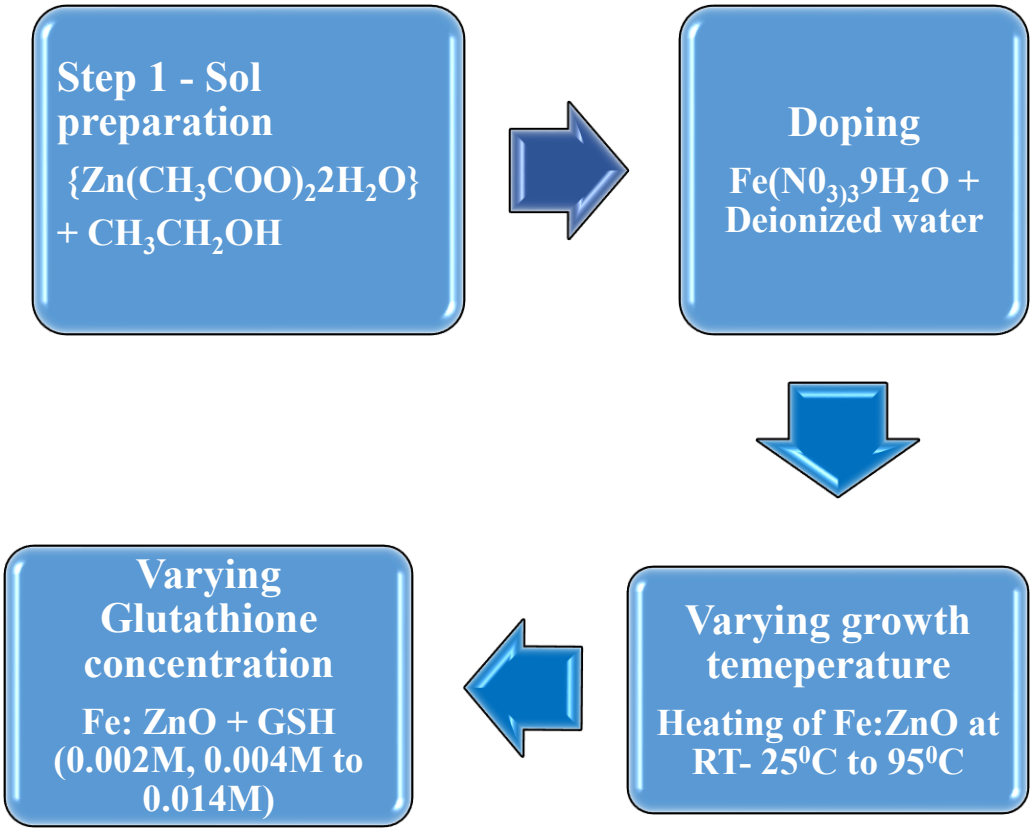


Figure 3.1: Flow Chart Showing the Experimental Procedure for the Synthesis and Doping of ZnO NPs.

3.4 Characterization and Analysis

3.4.1 X-ray Diffraction (XRD)

The X-ray diffraction technique was used to analyze the crystallographic structure and phase purity of Fe: ZnO NPs. For analysis, an X-ray diffractometer was used with Cu Kα radiation (λ = 1.5406 Å) at 40 kV and 0.9 mA was utilized. The recording of the diffraction patterns was done at a 2θ angle from 10° to 80°, using a step size of 0.02° and a scan speed of 2° each minute. XRD patterns were analyzed to confirm if the sample showed ZnO hexagonal wurtzite form, and shifts or new peaks were analyzed to confirm the presence of Fe. Crystallite sizes were determined with the help of the Debye-Scherrer equation using the FWHM of the main diffraction peaks.

3.4.2 Fourier Transmission Infrared Spectroscopy (FTIR)

This technique was utilized in identifying present functional groups from GSH on the surface of Fe: ZnO NPs. The amine (N-H) and thiol group (S-H) from GSH indicated

effective capping at different concentrations. The FTIR spectra of the pure and GSH-capped ZnO NPs were recorded over a range of 400- 4000 cm^{-1}.

3.4.3 Ultraviolet-Visible Spectroscopy (UV- Vis)

UV-Visible spectroscopy was used to analyze how the nanoparticles absorb light and calculate their bandgap energy. The absorbance measurements were performed using a dual-beam UV-Vis machine in the wavelength range between 200 and 800 nm. A nanometer-wide slit was set, and the scan speed was set to 200 nm per minute. A clean quartz slide was used as the reference for baseline correction.

3.4.4 Photoluminescence Spectroscopy

The bandgap transitions and defect-related luminescence features of Fe: ZnO nanoparticles were examined by using photoluminescence spectroscopy. A PL spectrometer with a 325 nm He-Cd laser was used to take the required measurements. The dispersed light passed through a monochromator with 1200 grooves per millimeter and was captured by a cooled sensor. Reading the spectra took place between 350 and 800 nanometers, using a 1 nm slit and an integration time of 2 seconds for best resolution and signal strength. The excitation wavelength was 300 nm.

3.5 Summary

This chapter outlined the materials used in this study and their purity. It entails the steps followed during synthesis per objective. The characterization techniques have been given according what they analysed and the specifications set to. XRD majored on the crystal structure, PL analyzed the emission behaviour, UV-Vis spectroscopy for optical analysis and FTIR for chemical bonding and functional groups present synthesized Fe: ZnO NPs and GSH capped Fe: ZnO NPs

CHAPTER FOUR

RESULTS AND DISCUSSION

4.1 Introduction

This chapter discusses results obtained from XRD, PL, and UV Vis analysis. The results have been discussed according to the specific objectives. It entails the effects of varying the doping concentration, growth temperature, and GSH capping concentration on the structural, optical, and photoluminescence properties of Fe: ZnO NPs.

4.2 Effects of Varying Doping Concentrations on the Structural and Optical Properties of Fe-doped ZnO Nanoparticles

4.2.1 X-Ray Diffraction (XRD) Analysis

The X-ray diffraction pattern obtained, as shown in Figure 4.1**,** was compared with the standard reference data from the Joint Committee on Powder Diffraction Standards (JCPDS), specifically card No. 01-070-8072, which matches well with the single-phase hexagonal wurtzite structure of ZnO. The analysis aimed to determine the changes in lattice parameters, crystallinity, or peak shifting arising from Fe incorporation into the ZnO lattice. The results confirmed that the synthesized samples retained the wurtzite hexagonal structure of ZnO, with no impurities, and the secondary phases of iron oxide were detected. This indicates that the dopant was successfully incorporated into the ZnO lattice without interfering with the phase purity, even at higher doping concentrations. The incorporation matches previous findings where low concentrations of transition metal dopants could enter the ZnO crystal lattice substitutionally (Panigrahy *et al.,* 2012).

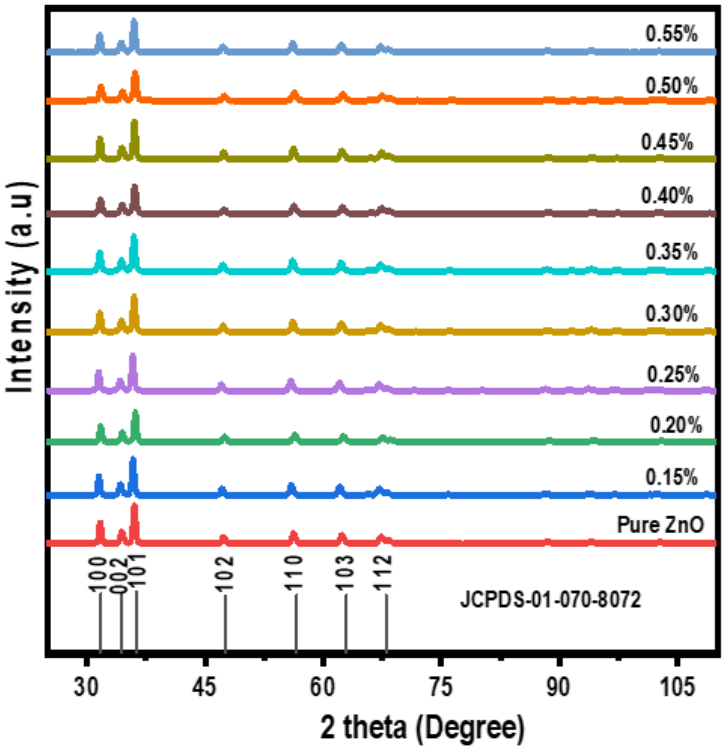


Figure 4.1: XRD Pattern for all Synthesized Samples of Fe: ZnO NPs at Varying Doping Concentrations

From Figure 4.1, it was observed that with an increase in Fe concentration, the intensity of major ZnO planes: (100, 002, 101) decreased gradually. This shows that there is a decrease in crystallinity due to the introduction of defects and strain by Fe^{3+} substitution, which matches what (Panigrahy *et al.,* 2012) reported. The diffraction peaks also shifted slightly towards the lower angles and were more pronounced at the (101) plane, suggesting the growth of tensile stress, as a result of Fe^{3+} distribution. This is in agreement with other studies done by (W. Cheng & Ma, 2009) that indicated that lower-angle shifts provided evidence of lattice expansion in doped ZnO. The interplanar d spacing and the average crystallite size were calculated using Bragg's equation and Debye-Scherrer formula, respectively. The results obtained are summarized in Tables 4.1 and 4.2. Equation 4.1 gives Bragg's equation (Abd-Elkader et al., 2023), and Equation 4.2 gives the Debye-Scherrer formula(Alagiri *et al.,* 2011).

$$n\lambda = 2d \sin\theta \quad (4.1)$$

Where n represents the order of diffraction (n=1), λ is the wavelength of the incident rays, d is the interplanar spacing between crystal planes, and θ is Bragg's angle, which is half of the 2θ.

$$\mathbf{D} = \frac{\mathbf{0.9\lambda}}{\boldsymbol{\beta COS\ \theta}} \qquad (4.2)$$

Where D is the crystallite size in (nm), λ is the wavelength1.5406Å (Cu Kα radiation) of X-rays (1.5406Å), β is the full width at half maximum (FWHM) of the peak in radians, and θ is the Bragg angle.

In Table 4.1, as compared to the JCPDS card for hexagonal wurtzite ZnO (JCPDS No. 01-070-8072), the diffraction peaks at 2θ values of 31.801, 34.421, and 36.299 are representative of the basic crystal planes (100), (002), and (101), respectively. For the pure ZnO, the observed 2θ values for planes (100), (002), and (101) are 33.942°, 36.704°, and 38.304°, respectively. The slight deviation from the standard values is attributed to broadening, size effects, and minor lattice distortions associated with the synthesized nanoparticles, as reported by (Thakur *et al.,* 2021).

The calculated lattice constants a and c of the synthesized pure ZnO sample were a 3.048Å and c 4.893 Å. These are very comparable to those of bulk ZnO, a=3.249A, c=5.206A from JCPDS 01-070-8072, with a slight reduction attributed to lattice shrinkage of nanoparticles. The Fe-doped ZnO synthesized in this study displayed small changes in the lattice parameters a = 3.039 to 3.063 and c = 4.885 to 4.918 A, and this was an indication that the Fe ions substituted the Zn in the ZnO lattice successfully. The minor deviations of the values in bulk are attributed to the strain and substitutional doping, as reported by (Samanta *et al.,* 2017).

When Fe was introduced, a shift in the diffraction peaks was observed systematically. At 0.15% Fe doping, the (100) peak is located at 33.788°, while at 0.55% Fe doping, the position of the (100) peak is at 33.892°. A similar trend can be observed for the (002) and the (101) peaks. These maxima indicate the coherent integration of Fe ions into the ZnO crystal lattice, leading to the formation of tensile lattice strain due to the substitution of relatively smaller ionic radii of Fe^{3+} (0.645 Å) for relatively larger ionic

radii of Zn^{2+} (0.74 Å), causing distortion and lattice strain due to a mismatch in ionic size, as earlier reported by (Sobiyi & Akinlabi, 2017). Such distortion interferes with interplanar spacing, leading to minor shifts in peaks, which is a typical indication of successful doping at the atomic level (Alagiri *et al.,* 2011). The lattice parameters displayed a slight variation with increased doping concentration. The observed contraction in both a and c is attributed to the substitution of Zn^{2+} by Fe^{3+} (Samanta et al., 2017).

Table 4.1: 2θ (Degrees), average d-spacing, and lattice parameters (a and c) of all synthesized samples (Pure ZnO, 0.15%Fe, to 0.55%Fe)

Plane	**100**	**002**	**101**	**102**	**103**	**200**	**Average d-spacing**	**a**	**c**
	2θ (Degrees)								
ZnO	33.94	36.70	38.30	49.61	58.49	64.63	2.048	3.048	4.893
0.15	33.78	36.53	38.13	49.40	58.82	64.37	2.054	3.061	4.915
0.2	34.01	36.75	38.41	49.74	58.65	64.80	2.043	3.041	4.886
0.25	33.75	36.51	38.10	49.36	58.21	64.31	2.058	3.063	4.918
0.3	33.90	36.66	38.26	49.56	58.44	64.56	2.050	3.051	4.898
0.35	33.88	36.64	38.24	49.53	58.41	64.54	2.051	3.052	4.901
0.4	33.98	36.73	38.34	49.66	58.55	64.68	2.046	3.044	4.890
0.45	33.94	36.71	38.31	49.62	58.51	64.64	2.047	3.047	4.891
0.5	34.03	36.76	38.39	49.71	58.62	64.75	2.044	3.039	4.885
0.55	33.89	36.64	38.25	49.54	58.41	64.54	2.051	3.051	4.901

As summarized in Table 4.2, the FWHM, β values observed reveals a decline (Pure ZnO- 0.3411, 0.15%- 0.3273) for peak (101) at lower concentrations of Fe (0.15 – 0.2 %), which may be attributed to a marginal increase in crystallinity, while FWHM values increase at higher Fe doping (0.3 – 0.5%), reflecting lattice strain and a decrease in crystallite size. This is aligned with (S. Kumar et al., 2021) findings, where Fe-doped ZnO nanoparticles achieved initial enhancements at low Fe doping levels. Still, the FWHM and crystallinity deteriorated at higher Fe levels due to the dopant's impact on the lattice. In a similar study, (Amin, 2023) found that FWHM values rise with the

Fe content of ZnO thin films and explained this as due to strain in the associated lattice. In addition, (Roy *et al.,* 2021) reported that the XRD patterns recorded for ZnO nanoparticles exhibited a decrease in crystallite size and broadening of the diffraction peaks as the level of Fe doping increased. Similarly, in another related study, (Salaken *et al.,* 2013) noted that maximum crystallinity was observed at low Fe doping levels. Still, high Fe doping levels were associated with increased FWHM values and inferior structural properties. These comparisons corroborate the findings in the present work, pointing out that although the minimal Fe doping can improve ZnO nanoparticle crystallinity, excessive Fe doping increases stress and defects in the material.

Table 4.2: Summarized FWHM (Degrees) of six XRD peaks and corresponding crystallite Sizes D (nm) for all synthesized samples (Pure ZnO, 0.15%Fe to 0.55%Fe).

Plane	**100**	**002**	**101**	**102**	**103**	**200**	**Crystallite size D (nm)**
	FWHMβ (Degrees)						
ZnO	0.33410	0.43184	0.34116	0.46806	0.47911	0.55375	22.96
0.15	0.32293	0.41740	0.32730	0.44009	0.45039	0.50825	23.81
0.2	0.31477	0.40740	0.32829	0.45869	0.47051	0.57393	24.19
0.25	0.32686	0.44740	0.33972	0.44734	0.46216	0.53234	22.95
0.3	0.34337	0.42899	0.34471	0.45995	0.46836	0.52105	22.70
0.35	0.35367	0.43152	0.34285	0.46120	0.46356	0.53241	22.47
0.4	0.38926	0.44758	0.38214	0.55087	0.52865	0.61008	20.68
0.45	0.33226	0.43498	0.38555	0.45971	0.46399	0.53681	22.01
0.5	0.39401	0.45574	0.37692	0.53688	0.53093	0.61095	20.59
0.55	0.34561	0.44673	0.34707	0.47877	0.47450	0.55600	22.33

Figure 4.2 depicts FWHM and crystallite size as a function of Fe doping concentrations in Fe: ZnO nanoparticles. A significant trend is observed here: as the Fe doping concentration increases, the FWHM values increase while the crystallite sizes decrease. This inverse correlation indicates that higher Fe doping levels cause increased distortions and defects to the lattice, which decrease crystallite size and broaden the diffraction peaks. This is consistent with (C. Liu *et al.,* 2012), who

reported that with the incorporation of Fe in ZnO nanoparticles, there was a decrease in crystallite size and higher FWHM values, suggestive of greater lattice stress and defects. Similarly, (C. Liu *et al.,* 2012) reported a decrease in crystallite size and an increase in FWHM due to doping of Fe, wherein the smaller ionic size of Fe^{3+} substituted for Zn^{2+} ions, causing strain and defects in the ZnO lattice.

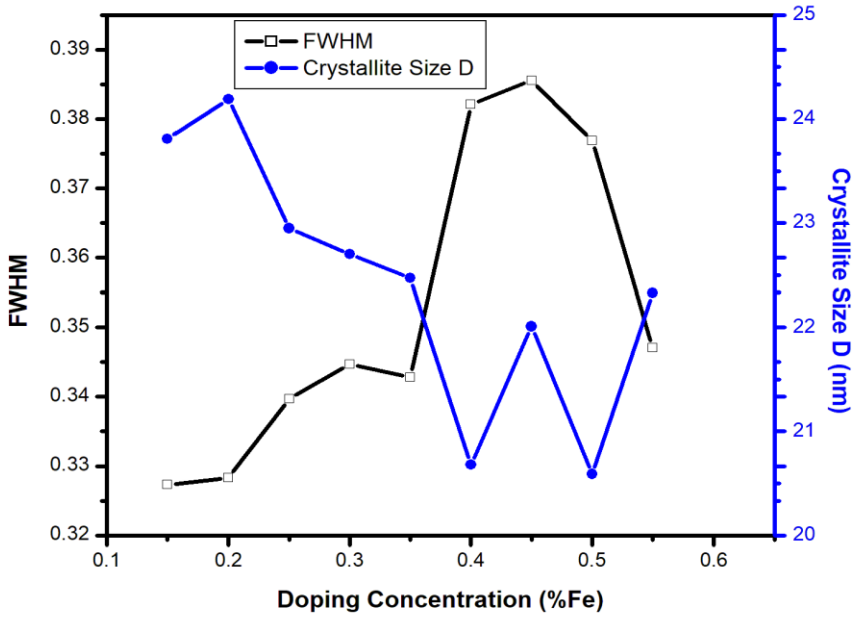
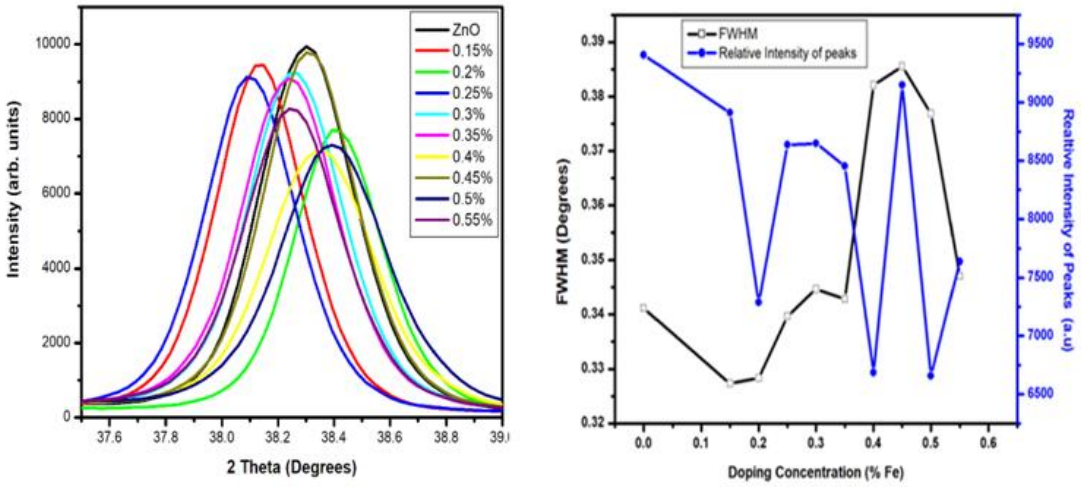


Figure 4.2: Variation of FWHM and Crystallite Size of Synthesized Fe: ZnO NPs at Varying Doping Concentrations.

Peak intensities give insight into the degree of crystallinity. Pure ZnO displays the highest intensity (9408.4 a.u), as shown in Figure 4.3 (a), which decreases when doped, especially at high concentrations (0.5% Fe and 0.55% Fe). This decline is attributed to strain-induced defects within the lattice, which scatter the X-rays and reduce the intensity and peak sharpness (Naik *et al.,* 2021). However, the intensity increases slightly at 0.45% Fe, suggesting a transient crystallinity enhancement, possibly indicating an optimal doping threshold where structural order is improved momentarily (Alsaad *et al.,* 2020). The variation of FWHM and peak intensity with increasing doping concentration in Figure 4.3 (b) indicates significant structural changes in the crystal structure of ZnO NPs, attributed to increased crystal defects, lattice strain, and a reduction in crystallite size, which is due to Fe^{3+} incorporation into

the ZnO lattice (Amin, 2023). The non-linear trend observed at 0.45 % Fe, where the size of crystallites temporarily increases and FWHM decreases, indicates the existence of optimum doping; however, it is possible to state that, in the studied case, the optimal doping is 0.45 % Fe. At this concentration, Fe^{3+} ions can partially passivate the defects or stabilize the lattice by filling the substitutional positions more homogeneously and thereby minimize strain. This short-term variance in microstrain increases the level of crystallinity prior to high levels of doping above 0.45 % Fe that cause more distortions and defects, resulting in a new drop in the size of crystallites and a rise in FWHM. This type of anomalous trend at the optimum level of dopants has also been reported in other transition metal-doped ZnO systems, which predicts enhanced order at a certain dopant concentration (Alsaad *et al.,* 2020).



(a) **(b)**

Figure 4.3: (a) XRD most intense peaks at plane (101) of Fe: ZnO NPs. (b)Variation of FWHM and Relative intensity of peaks at varying doping concentrations of Fe: ZnO NPs.

4.2.2 Estimation of Strain

The strain induced in NPs due to crystal imperfections and distortion was calculated using the Williamson-Hall method, shown by equation 4.3(Mote *et al.,* 2012).

$$\varepsilon = \frac{\beta}{4 \tan \theta} \qquad (4.3)$$

where ε represents the microstrain, β is the FWHM in radians, and θ is the diffraction angle of the most intense peak (101). The microstrain increased with an increase in doping concentration as summarized in Table 4.3, which is associated with enhanced lattice imperfections and distortions caused by Fe^{3+} incorporation into the ZnO lattice (Samanta *et al.,* 2017). The crystallite size and microstrain display an inverse relationship, as shown in Figure 4.4. As crystallite size decreases, microstrain increases at varying doping concentrations, indicating that Fe^{3+} incorporation causes lattice distortions(Winarsih *et al.,* 2024). These findings match previous research. For example, (Roy *et al.,* 2021) demonstrated that the increase in Fe doping in ZnO nanoparticles led to a decrease in crystallite size and increased microstrain, which indicates a dopant-induced effect. Moreover, (Parveen *et al.,* 2024) reported that an increase in microstrain and a decrease in crystallite size when Fe was incorporated into ZnO is attributed to growing internal stress induced by Fe substitution.

Table 4.3: Variation of crystallite size D (nm) and strain of Fe: ZnO NPs at peak (101)

Doping Concentration (%Fe)	**FWHM β (Degrees)**	**Crystallite Size D (nm)**	**Strain (ε)**
Pure ZnO	0.34116	22.96	0.004286
0.15	0.32730	23.81	0.004132
0.2	0.32829	24.19	0.004112
0.25	0.33972	22.95	0.004293
0.3	0.34471	22.70	0.004336
0.35	0.34285	22.47	0.004315
0.4	0.38214	20.68	0.004795
0.45	0.38555	22.01	0.004843
0.5	0.37692	20.59	0.004723
0.55	0.34707	22.33	0.004367

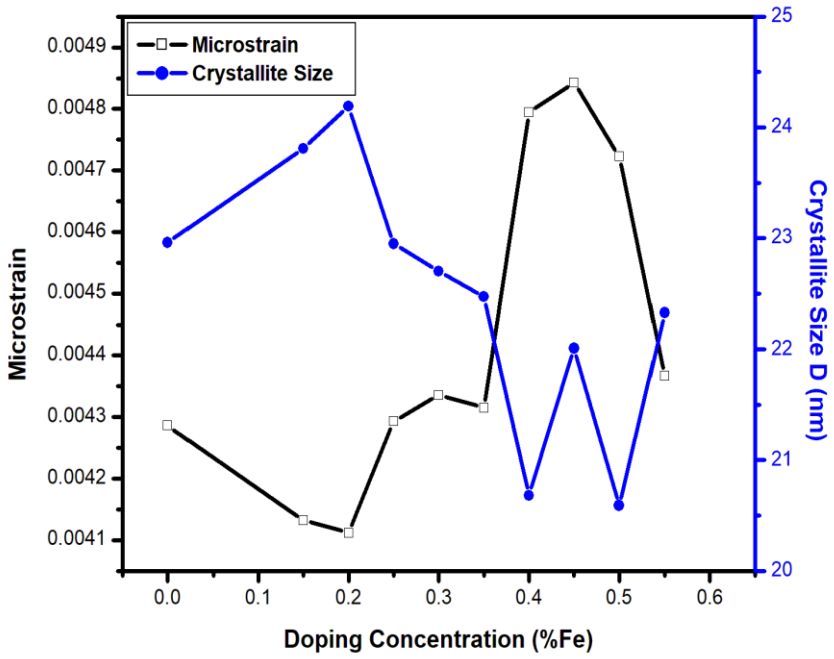


Figure 4.4: Variation of Microstrain and Crystallite size of Fe: ZnO NPs at Varying Doping Concentrations.

4.2.3 Photoluminescence Spectroscopy

Figure 4.5 below shows the photoluminescence spectra of Fe: ZnO NPs at an excitation wavelength of 300 nm, recorded at room temperature at an emission range of (250 to 800 nm). This analysis aimed to assess the influence of Fe doping concentration on the deep-level effect emissions and band edge emission of ZnO.

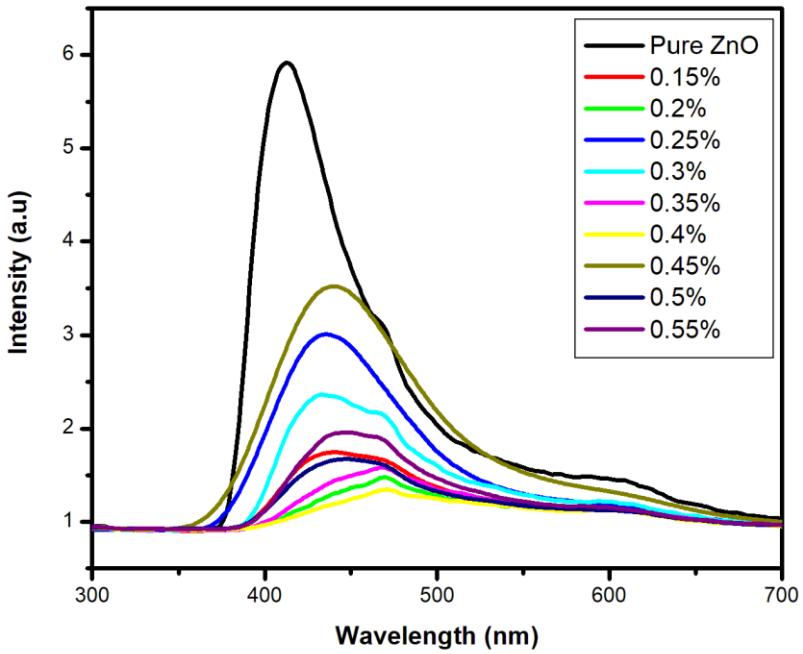


Figure 4.5: Photoluminescence Spectra of Fe: ZnO NPs at Varying Doping Concentrations

The PL spectra of Fe-doped ZnO nanoparticles display changes in emission characteristics with an increase in doping concentration. Pure ZnO exhibits a strong near-band edge emission NBE centered around 423 nm, which is generated from excitonic emission and a weak deep level emission DLE in the visible range 500-700 nm. The weak DLE band is due to intrinsic point defects such as oxygen vacancies and zinc interstitials (Vanheusden *et al.,* 1996). As Fe is added to the sample, the emission peaks increasingly shift toward lower energies, to 508 nm at 0.4 % Fe, due to the creation of intermediate defect energy levels within the bandgap associated with Fe^{3+} incorporation. The intensity of the PL signal, as shown in Table 4.4, is initially suppressed in the low doping concentration range of 0.15-0.3 % Fe due to the formation of non-radiative recombination centers. However, a clear increase in the intensity is observed in defect densities above 0.45 %, which could be attributed to the defect passivation or radiative recombination from newly introduced localized states.

The decrease in PL peak intensity found after Fe doping, especially in the 0.15- 0.3% Fe range, is attributed to the introduction of non-radiative recombination centers were introduced into the ZnO lattice. Fe^{3+} incorporation creates localized defect states under which carriers are trapped and over which near-band-edge (NBE) emission is

quenched. Depending on the doping concentration, these centers compete with the radiative pathways, which results in the quenching of the PL at low to moderate doping levels. Partial passivation of such non-radiative centers takes place as the concentration of the dopant decreases down to 0.45 % and we see an increase in intensity of the PL.

To accommodate the overlapping of contributions needed to reconstruct the NBE region, the PL curves were fitted using multi-Gaussian analysis. In case of pure ZnO, three bands were observed with maxima at around 381, 406, and 450 nm. These peaks are respectively due to free exciton (FX), donor-bound exciton (D^oX), and donor–acceptor pair (DAP) recombination. These approaches are in line with the earlier studies that confirm that ZnO-based nanomaterials exhibit multiple peaks (Djurišić & Leung, 2006). For 0.45% Fe-doped ZnO exhibited three emission peaks were observed at 402, 443, and 446 nm. They are attributed to donor-bound excitons (D^oX), donor-acceptor pair (DAP) transitions, and defect-related states. Measured redshift and broadening relative to pure ZnO indicate that Fe incorporation affects the recombination dynamics through the introduction of defect levels and modification of the local electronic environment(Das *et al.,* 2003).

In the present study, we found that the DLE band, which is usually broad and with a maximum occurring in the 550–650 nm range, was either reduced or practically not distinguishable in all the pure and Fe: ZnO samples. This can be attributed to improved crystalline quality and a decrease in intrinsic defect concentrations, and though it is also highly likely that the Fe doping passivates native defect sites(F. Yu *et al.,* 2019). This means that DLE is also suppressed when using ZnO-based systems doped with transition metals, with surface modifiers suppressing oxygen vacancies and surface states, which results in enhanced excitonic emissions (Kavita *et al.,* 2014). These trends are consistent with existing literature. (Mohamed Basith *et al.,* 2016) reported a redshift and quenching followed by enhancement of PL intensity in Fe-doped ZnO nanostructures and attributed the mechanisms to Fe-related defects and oxygen vacancies. Similarly, (Srinivasulu et al., 2017) mentioned that Fe doping helps to control PL emissions through shallow donor and acceptor levels, which enhance defect-driven radiative transitions. In other recent work, it was pointed out that

increasing the concentration of Fe increases the visible emission due to the formation of oxygen vacancies and Zn interstitials (Esbergenova *et al.,* 2024).

Table 4.4: FWHM and PL peak intensities of Fe: ZnO NPs at varying doping concentrations.

Doping Concentration (%Fe)	Emission Wavelength (nm)	FWHM, β (Degrees)	PL Intensity (arb.units)
Pure ZnO	422.64	47.259	4.1594
0.15	455.78	65.311	0.6879
0.2	489.94	113.01	0.3820
0.25	441.72	58.971	0.9226
0.3	450.63	65.594	1.2581
0.35	476.41	85.284	0.5182
0.4	507.55	146.30	0.3345
0.45	458.58	69.671	2.0359
0.5	456.94	66.815	0.6284
0.55	445.79	66.984	2.6767

The increased peaks of broader PL intensities in Fe-doped samples than the undoped counterpart can be attributed to the larger lattice disorder, higher defect concentration, and a wider range of the localized energy states. Broadening is caused by the presence of inhomogeneous strain, variations between the compositional fractions, as well as disparities in the defect surroundings contributed by the Fe^{3+} ions. Conversely, areas under the peaks of the undoped ZnO sample are much sharper since this sample is more crystalline and has fewer energy levels of defects. This tendency proves that the process of Fe doping alters the electronic structure of the material, with radiative recombination energies increasing in the range.

4.2.4 Optical Analysis

The absorbance spectra of pure and Fe: ZnO NPs are shown in Figure 4.6. The absorbance spectra displayed a strong absorption in the UV region (300 nm- 400 nm) with shifts in absorbance upon doping. The shifts indicate changes in the electronic transitions and impurity-induced states in the ZnO band structure. As doping

concentration increases, the absorption edge redshifts, which is attributed to the narrowing of the bandgap due to Fe^{3+} incorporation into the ZnO lattice, hence modifying the electronic environment (Iqbal *et al.,* 2021) .

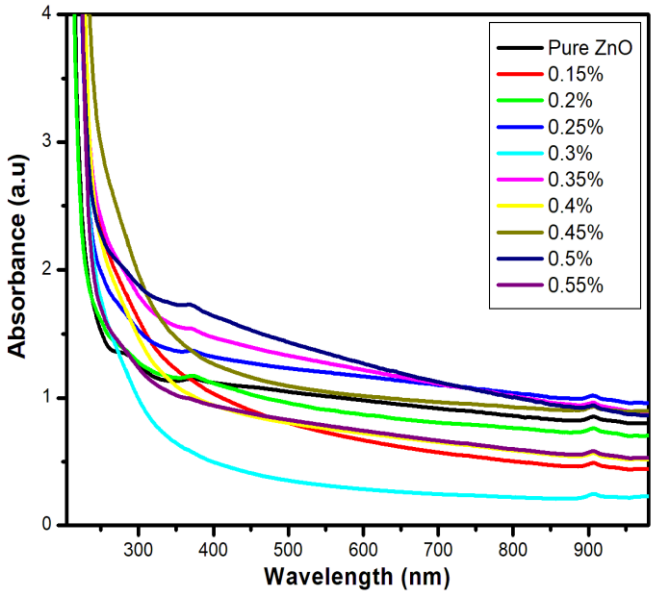


Figure 4.6: UV-Vis absorbance Spectra of Fe: ZnO NPs at Varying Doping Concentrations

To quantitatively calculate the optical bandgap (E_g), Tauc plots were constructed, and the Tauc relation was used. Equation 4.4 gives the Tauc relation(Madkhali, 2022)

$$(\alpha h\nu)^n = A(h\nu - E_g) \qquad (4.4)$$

Where α is the absorption coefficient, $h\nu$ is the photon energy, E_g is the optical bandgap, A is a constant, while n depends on the number of electronic transitions. $n=\frac{1}{2}$ for direct allowed transitions, while n =2 for indirect allowed transitions. Since ZnO is a direct bandgap semiconductor, $n=\frac{1}{2}$ was used. The Tauc plot was obtained by plotting $(\alpha h\nu)^2$ against photon energy ($h\nu$), and the optical band gap was obtained by extrapolating the linear portion of the curve to the x-axis where $(\alpha h\nu)^2 = 0$. Figure 4.7 shows the optical band gaps obtained through extrapolation and summarized in Table 4.5.

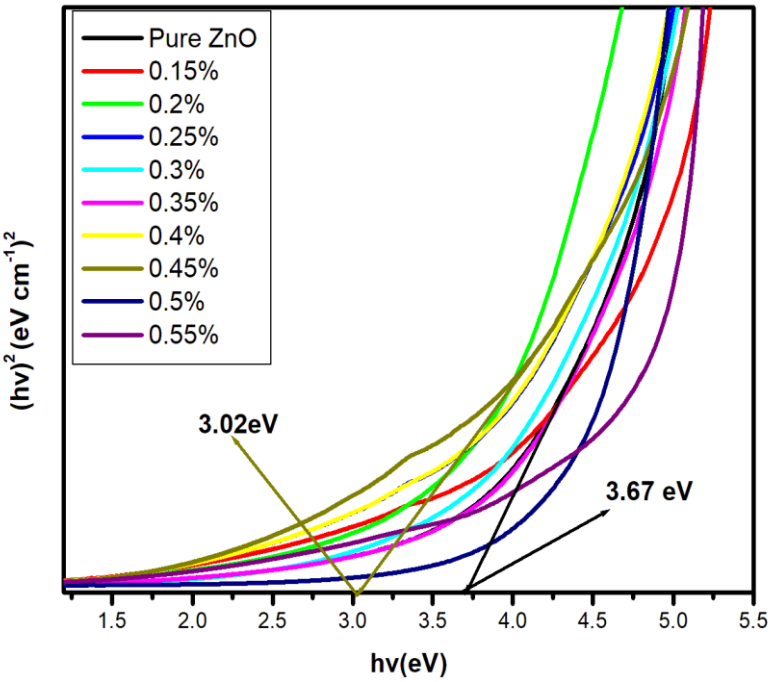


Figure 4.7: Tauc Plot of Fe: ZnO NPs Showing Band Gaps as Obtained Through Extrapolation of the Linear Curves.

The data in Table 4.5, obtained from the Tauc plot, demonstrate narrowing of the bandgap with increasing Fe doping concentration up to 0.45% (3.02 eV) and then a widening of the bandgap at greater concentrations of 0.55%. Similar findings have been reported, for example, (Raciti *et al.,* 2017) reported that the optical bandgap energy of pure ZnO nanoparticles was 3.82 eV, and decreased to 3.80 eV after doping with Fe, suggesting that Fe doping introduces defect levels in the bandgap, leading to a redshift in absorption and a decrease in bandgap energy. Another study done by (Ahammed *et al.,* 2018) reported a decrease in bandgap energy from 3.2 eV to 3.1 eV with an increase in Fe doping concentration, enhancing visible light absorption. At higher doping concentrations, the bandgap increases once again. This can be attributed to the Burstein-Moss effect, where filling the lower energy states in the conduction band due to high carrier concentration widens the bandgap (Ivchenko, 2024). This has been reported by (Srivastava *et al.,* 2014) where the bandgap of Fe-doped ZnO increased from 3.14 eV to 3.29 eV with increasing Fe doping concentration.

It is specifically pertinent in the case of bioimaging applications, where it is possible to control the bandgap of ZnO nanoparticles using Fe doping. This reduces the energy

bandgap and results in better absorption in the visible region, which could be useful for imaging. Nonetheless, excessive doping resulting in an enhanced bandgap can decrease the efficacy of ZnO nanoparticles in bioimaging.

Table 4.5: Variation of Doping Concentration and Band Gap Energy of Fe: ZnO NPs

Doping concentration (% Fe)	Band gap (eV)
Pure ZnO	3.67
0.15	4.25
0.2	4.20
0.25	3.97
0.3	3.91
0.35	3.84
0.4	3.50
0.45	3.02
0.5	4.32
0.55	4.48

The variation of pure ZnO band gap (3.67 eV) larger than the standard value for pure ZnO nanoparticles value of approximately 3.37 eV, can be explained using the quantum confinement effect, when the size of ZnO particles is smaller than the exciton Bohr radius of 2.34 nm, the bandgap of the material widens due to the tangling of the charge carriers(Manzoor *et al.,* 2015). Moreover, synthesis parameters, including synthesis routes, sol-gel method, and reaction temperature, affect the formation of these defects or an oxygen-rich atmosphere that strongly alters the bandgap (Nabil *et al., 2021)*.

4.2.5 FTIR Analysis

FTIR spectroscopy was used to identify the chemical bonding and functional groups in both pure and Fe-doped ZnO nanoparticles. In the 4000–400 cm^{-1} range, FTIR spectra in Figure 4.8 show several different absorption peaks and their positions and intensities change with increasing doping concentration, reflecting changes in the material's structure. Zn–O stretching vibrations associated with the wurtzite ZnO structure were identified from the main absorption band found between 900 and 1000

cm^{-1} in all the samples. It should be noted that as Fe concentration increased, the peak widened and shifted a little, associated with the replacement of Zn^{2+} with Fe^{3+} in the compound, which brings about lattice deformation and distortion due to smaller ionic radii (P. Kumar *et al.,* 2024). All samples display a wide band around 3155 cm^{-1} and this band is attributed to the O–H stretching vibration of hydroxyl groups or water adsorbed on the nanoparticles. Fe-doping caused a slight decline in the band intensity, which could be related to a lower amount of hydroxylation or altered surface chemistry caused by Fe ions. This behavior aligns with (Hu *et al.,* 2022), who reported that metal ion doping alters surface bonding sites in ZnO nanoparticles. Another peak seen at 1173 cm^{-1} indicates the H–O–H bending vibrations of molecular water. Bands between 1400 and 1500 cm^{-1} are attributed to either C–H bending or C=O stretching, which may be from organic substances or CO_2 in the air. Increased doping led to these bands having lower intensities, indicating more complete precursor decomposition during synthesis, as reported previously by (Davoodi & Shafeeyan, 2024). No specific oxides such as Fe_2O_3 or Fe_3O_4 were observed, confirming that Fe ions joined the ZnO structure without creating separate oxide phases that would change the purity of ZnO, which confirms the structural integrity of the doped samples (Reddy *et al.,* 2014).

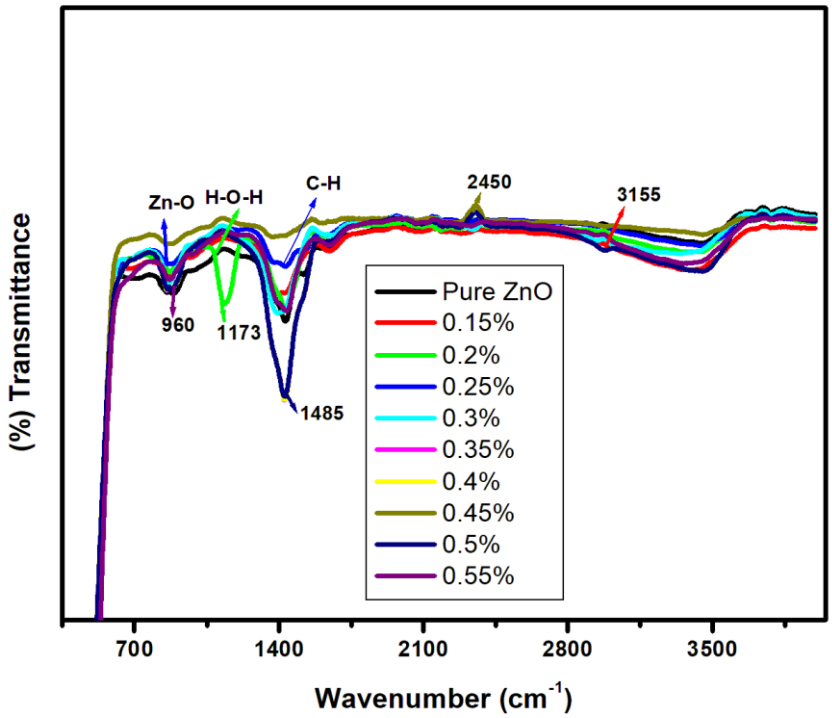


Figure 4.8: FTIR spectra of Fe: ZnO NPs at Different Doping Concentrations.

4.3 Effects of Varying Growth Temperature on Optical and Structural Properties of Iron-doped Zinc Oxide Nanoparticles

4.3.1 XRD Analysis

The X-ray diffraction pattern obtained, as shown in Figure 4.9**,** was compared with the standard reference data from the Joint Committee on Powder Diffraction Standards (JCPDS), specifically card No. 01-070-8072. All samples were synthesized from 0.45% Fe, and the growth temperature varied from room temperature (RT), 35°C, 45°C, 55°C,…….95°C, all exhibited distinct diffraction peaks corresponding to the hexagonal wurtzite phase of ZnO with no secondary phases detected. This indicates the successful incorporation of Fe^{3+} on the ZnO lattice without phase segregation.

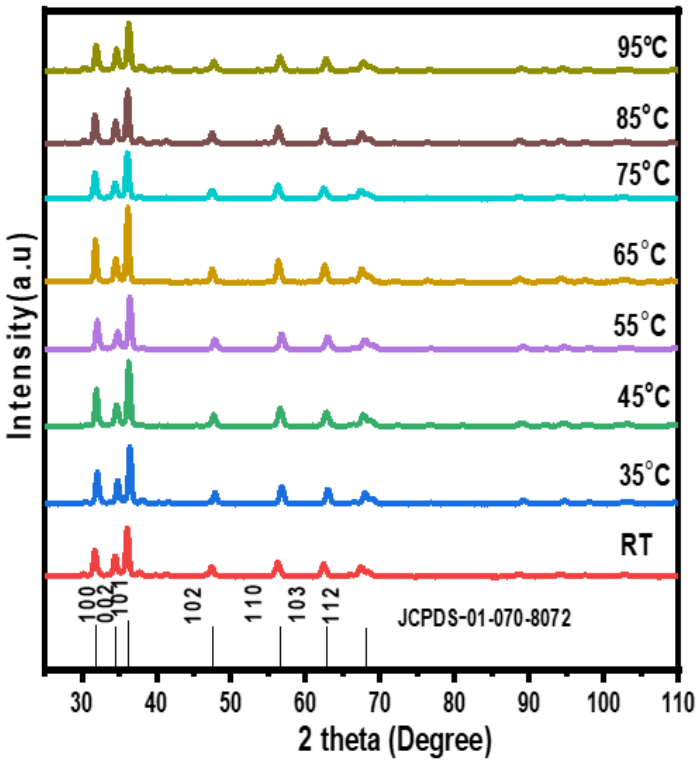


Figure 4.9: XRD Pattern Showing Diffraction Peaks of Fe: ZnO NPs at Different Growth temperatures

The most intense peak observed at plane (101) was analyzed in detail to study the crystallinity and lattice distortion across the temperature range. With increased growth temperature, a gradual intensification and sharpening of XRD peaks were observed between 55°C and 75°C, indicating enhanced crystallinity due to atomic diffusion and

grain growth at high temperatures (Mufti *et al.,* 2018). This trend is consistent with previously reported findings where elevated growth temperatures promoted crystallite growth and reduced structural disorder on Fe: ZnO NPs (Abd-Elkader *et al.,* 2023).

The interplanar d spacing and the average crystallite size were calculated using Bragg's equation and Debye-Scherrer formula, respectively. Equation 4.1 gives Bragg's equation (Abd-Elkader *et al.,* 2023), Equation 4.2 gives the Debye-Scherrer formula

The average crystallite size in Table 4.6 indicated a decrease from around 22.75 nm at room temperature to approximately 18.26 nm at 65°C, followed by a decrease at higher temperatures. These findings are corroborated by prior reports, (Aragón *et al.,* 2023) a similar trend was observed on Fe: ZnO NPs synthesized via hydrothermal methods, where the crystallite size decreased with growth temperature. Similarly, (Dasuki *et al.,* 2023) studied the effect of temperature on the ZnO nanostructures, confirmed that a decrease in growth temperature led to better crystallinity and sharper XRD peaks, attributed to better grain boundary diffusion in the nucleation stage. The results also indicate that as the growth temperature increases, the FWHM increases, corresponding to a decrease in crystallite size. This trend suggests enhanced crystallinity and grain growth at elevated temperatures, as reported by (Kaningini *et al.,* 2022) who discovered that higher growth temperatures improved the crystal quality of ZnO NPs, inducing a reduction in the FWHM value. The systematic shift in 2θ values in Table 4.7 to higher angles shows a decrease in lattice spacing (d), indicating a compressive strain within the ZnO lattice. Such strain is introduced when Fe^{3+} substitutes $Zn^{2+,}$ causing lattice contraction. A similar trend has been reported, for example, (Srinivasulu *et al.,* 2017) discovered that Fe: ZnO showed the same 2θ shifts to higher values with doping, indicating successful incorporation and lattice distortion.

Table 4.6: FWHM and crystallite size values of all Fe: ZnO NPs samples at different growth temperatures.

Plane	100	002	101	102	103	200	Crystallite Size D (nm)
	FWHM (Degrees)						
Room Temperature (RT)	0.41084	0.3727	0.3877	0.5399	0.5840	0.6036	22.75
35^0C	0.4234	0.3993	0.4032	0.5121	0.5413	0.5638	21.18
45^0C	0.4447	0.4352	0.4164	0.5547	0.5750	0.6376	20.65
55^0C	0.4043	0.4684	0.4270	0.5588	0.5737	0.6450	19.88
65^0C	0.3440	0.4412	0.4453	0.4985	0.5013	0.5688	18.26
75^0C	0.4137	0.4307	0.4276	0.6063	0.6192	0.6927	19.09
85^0C	0.3841	0.3941	0.4013	0.5088	0.5381	0.5442	21.64
95^0C	0.4318	0.4279	0.3851	0.5984	0.5897	0.6067	22.69

Table 4.7: 2θ, d spacing, and lattice parameters a and c values of all planes for Fe: ZnO NPs at different growth temperatures.

Plane	100	002	101	102	103	200	Average d-Spacing	a	c
	2θ (Degrees)								
Room Temperature	33.99	36.71	38.35	49.66	58.54	64.67	2.34	4.564	4.891
35^0C	34.30	37.06	38.71	50.09	58.04	65.22	2.32	4.524	4.847
45^0C	34.18	36.93	38.57	49.93	58.86	65.03	2.33	4.539	4.863
55^0C	34.30	37.04	38.70	50.08	59.04	65.20	2.32	4.524	4.850
65^0C	34.05	36.80	38.42	49.75	58.65	64.80	2.34	4.556	4.880
75^0C	34.01	36.71	38.37	49.67	58.57	64.69	2.34	4.562	4.891
85^0C	34.01	36.76	38.40	49.71	58.60	64.74	2.34	4.561	4.885
95^0C	34.17	36.91	38.56	49.92	58.84	64.99	2.33	4.540	4.865

4.3.2 Estimation of Strain and Dislocation Density

The strain induced in NPs due to crystal imperfections and distortion was calculated using the Williamson-Hall method, shown by equation 4.3, while dislocation density was calculated using the Williamson-Smallman relation as shown by equation 4.5.

$$\delta=\frac{1}{D^2} \quad (4.5)$$

Where δ is the dislocation density in nm^{-2}, and D is the crystallite size in (nm). The calculated values are shown in Table 4.8.

Table 4.8: Calculated Micro-Strain and Dislocation density at peak (101) for Fe: ZnO NPs at varying Growth temperatures.

Growth temperature ^{0}C	Micro-strain	Dislocation Density (nm^{-2})
Room Temperature (RT)	0.0051	0.0023
35	0.0047	0.0021
45	0.0048	0.0019
55	0.0049	0.0016
65	0.0044	0.0017
75	0.0052	0.0022
85	0.0047	0.0019
95	0.0051	0.0022

From the results in Table 4.8, Fe-doped ZnO NPs synthesized at various growth temperatures indicate that there is an inverse relationship between crystallite size and both microstrain and dislocation density. At a higher growth temperature of 55 °C, the crystallite size increases, but the microstrain and dislocation density decrease as shown in Figure 4.10, revealing improved crystallinity and fewer defects. This is in concordance with the work of (Hadimani *et al.,* 2018) who noted that as the substrate temperature is increased during deposition of Fe-doped ZnO NPs, the crystallite size increases while microstrain and dislocation density decrease due to enhanced atomic diffusion and grain growth at higher temperatures. Moreover, (Amin, 2023), observed reduced micro strain and dislocation density in Fe-doped ZnO nanoparticles decreased when the crystallite size increased due to substitution of Fe^{3+} entering the ZnO lattice, causing the lattice relaxation.

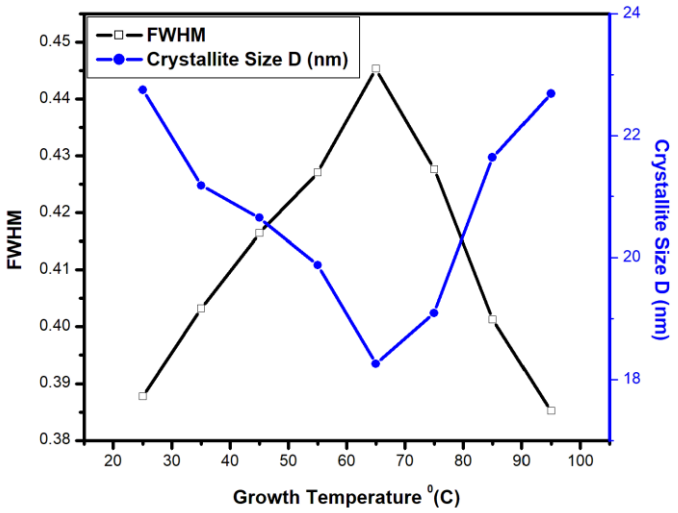


Figure 4.10: Variation of FWHM and Crystallite size D (nm) of Fe: ZnO NPs at varying growth temperatures.

4.3.3 Photoluminescence Analysis

Figure 4.11a shows the PL spectra of Fe: ZnO NPs at an excitation wavelength of 300 nm, recorded at room temperature at an emission range of 250 to 800 nm, and Figure 4.11b shows the Gaussian deconvolution of one of the synthesized samples at 65 °C. This analysis aimed to assess the influence of different growth temperatures on the deep-level effect emissions and band edge emission of ZnO.

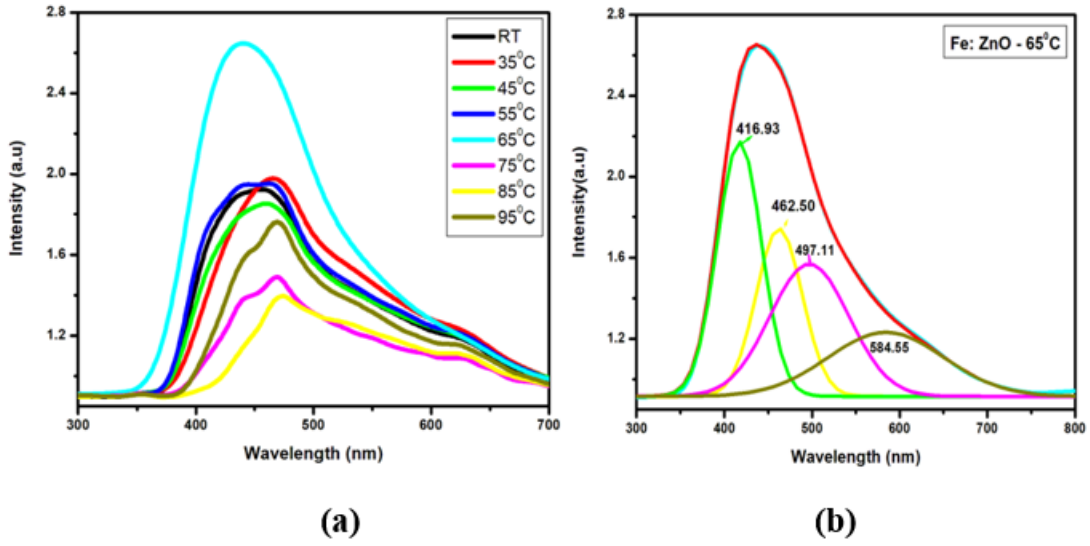


Figure 4.11: (a) Photoluminescence Spectra (PL) of Fe: ZnO NPs at Different Growth Temperatures and (b) Deconvolution of Fe: ZnO at 65 °C

PL spectra suggest that Fe-doped ZnO nanoparticles depict a temperature-dependent shift in both the emission wavelength and intensity. At lower growth temperatures (RT to 55 °C), the emission peaks were observed at 460–471 nm with moderate intensity ranging from 0.76 to 0.88 a.u, as shown in Table 4.9, which can be attributed to standard excitonic and defect-level transitions.

Table 4.9: Emission Wavelengths and PL Intensities of Fe: ZnO NPs at Different Growth Temperatures

Growth temperature ^{0}C	**Emission wavelength (nm)**	**PL Intensity**
RT	463.00	0.80492
35^{0}C	460.75	0.83990
45^{0}C	471.23	0.76596
55^{0}C	463.74	0.88127
65^{0}C	454.21	1.5083
75^{0}C	483.39	0.43535
85^{0}C	439.15	0.39656
95^{0}C	485.64	0.66529

Importantly, at 65 °C, the intensity of the PL reached 1.51 a.u and the emission wavelength shifted to 454.21 nm, indicating that the crystallinity increased and non-radiative defects were minimized. At higher temperatures (75 to 95 °C), a red shift to 483–485 nm and a decrease in intensity was found, which could be attributed to the generatively deep-level defects and non-radiative recombination. The findings match previous, for example (Gudla *et al.,* 2020) found increased PL intensity due to better crystallinity and reduced point defects in ZnO NPs synthesized at higher growth temperatures around 60°C. Moreover, (Dejene, 2022) investigated the ZnO nanocrystals and observed that when samples were synthesized at high growth temperatures (70 °C), PL red shifts and lower intensity were recorded due to defect clustering and thermal-induced stress.

The Gaussian deconvolution of the photoluminescence (PL) spectra of Fe: ZnO NPs prepared at different growth temperatures. It shows four distinctive emission bands,

which are associated with certain defects in the ZnO lattice. These emissions are concentrated around 417, 463, 497, and 585 nm. The 417nm emission is associated with zinc interstitials (Zn_i), which are shallow donor defects responsible for the near band-edge emissions (NBE). The peak at 463 nm is attributed to oxygen vacancies (V_O), commonly linked to green luminescence of ZnO. The 497 nm emission is associated with oxygen interstitials (O_i), and the 585 nm band is due to deep-level trap states resulting from Fe^{3+} ions (Mohamed Basith et al., 2016). These results match previous work on Fe: ZnO NPs. For example, similar defect-related emissions in Fe-doped ZnO NPs were reported by (Mohamed Basith *et al.,* 2016), who specified peaks corresponding to Zn_i, V_O, and Fe^{3+} trap states. The growth temperature dependence of PL intensity and peak position variation suggests that heat treatment has a controlling role in defect formation and distribution. The best growth temperature, at about 65 °C, leads to increased PL intensity, possibly because of the optimal defect concentration and crystallinity balance. Elevated temperatures can cause an increase in the presence of non-radiative recombination centers, which can decrease PL efficiency (Dejene, 2022).

4.3.4 Optical Analysis

Figure 4.12 shows UV– Vis absorbance spectra of the Fe-doped ZnO NPs synthesized at varying growth temperatures. The spectra reveal that the position of the absorption edge changed with the growth temperature. At lower growth temperatures (from 25 to 35 °C), the absorption edge moves to lower energies (blue shift), which means that the bandgap energy increases. This blue shift can be attributed to the Burstein–Moss effect, where an increase in the carrier concentration in the conduction band leads to the occupation of the lower energy levels, thus increasing the energy bandgap (Abd-Elkader *et al.,* 2023). When the growth temperature rises above 45°C, a shift in the absorption edge to a longer wavelength is observed, indicating a decrease in the bandgap energy. This red shift can be attributed to better crystallinity and fewer defects, which decreases the bandgap (Suchea *et al.,* 2009).

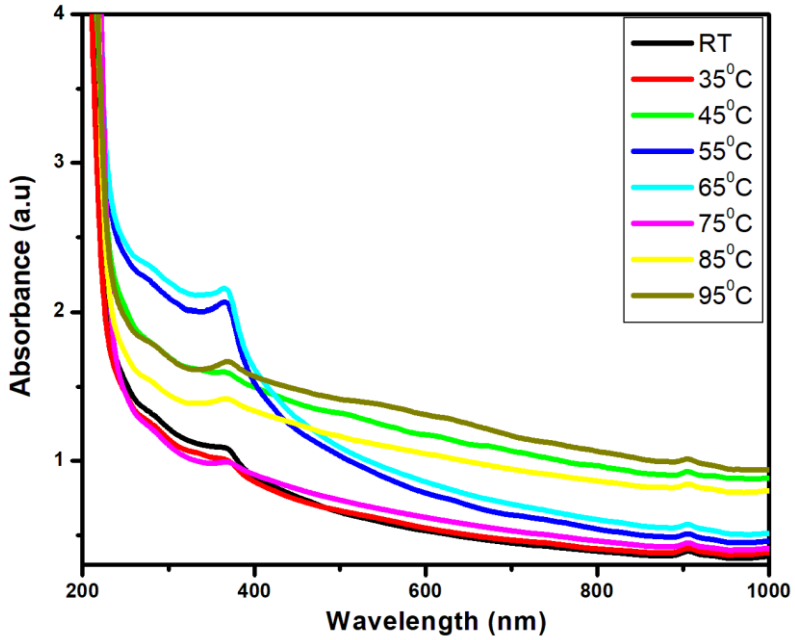


Figure 4.12: Ultra Violet Visible (UV Vis) Absorbance Spectra of Fe: ZnO NPs at Varying Growth Temperatures

To quantitatively calculate the optical bandgap (E_g), Tauc plots were constructed, and the Tauc relation was used. Equation 4.4 gives the Tauc relation (Madkhali, 2022). Where α is the absorption coefficient, hv is the photon energy, E_g is the optical bandgap, A is a constant, while n depends on the number of electronic transitions. $n=\frac{1}{2}$ for direct allowed transitions, while n = 2 for indirect allowed transitions. Since ZnO is a direct bandgap semiconductor, $n=\frac{1}{2}$ was used. The Tauc plot was obtained by plotting $(\alpha hv)^2$ against photon energy (hv), and the optical band gap was obtained by extrapolating the linear portion of the curve to the x-axis where $(\alpha hv)^2 = 0$. Figure 4.13 shows the optical band gaps obtained through extrapolation and summarized in Table 4.10.

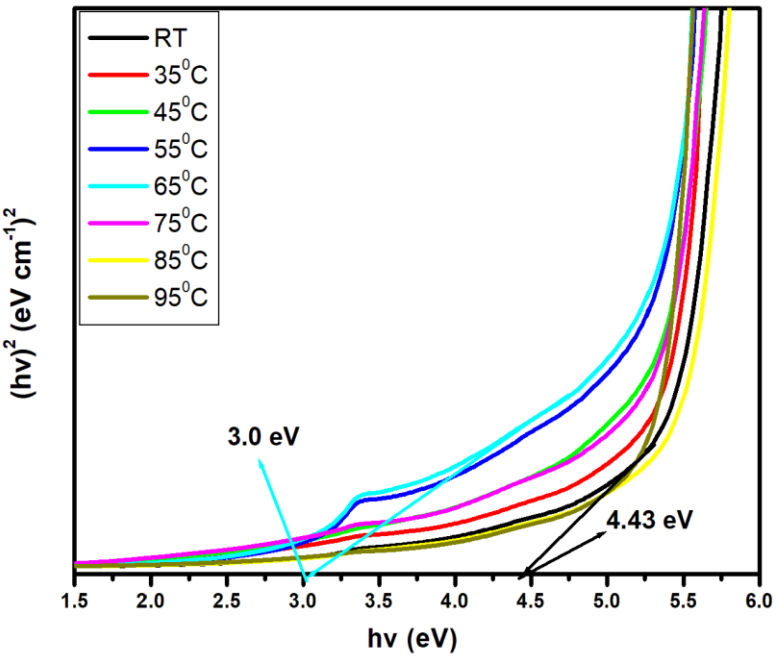


Figure 4.13: Tauc Plot Showing Extrapolated Band Gaps of Fe: ZnO NPs at Different Growth Temperatures

By extending the linear portions of the tauc plot to the photon energy axis, a clear dependence of band gap energies on the synthesis temperature is seen. The band gap was found to vary between the reference sample with room temperature synthesized Fe: ZnO (4.43 eV) to the highest value of 4.88 eV at 95 °C, and decreased sharply to a minimum of 3.0 eV at 65 °C. This non-monotonic behavior indicates the possibility of a relationship between the growth temperature, crystal quality, particle size, and dopant incorporation. The greater increase of the band gap at lower temperatures can be attributed to the quantum confinement effects by smaller crystallite size, which leads to a rise in the energy bandgap because of the restriction of motion of the charge carriers; This effect has been reported by (Ilican *et al.,* 2016). However, it should be noted that the observed blue shift at the low-temperature side can also partially originate from the Burstein–Moss effect, where the increasing carrier concentration, perhaps due to excess Fe doping, immerses the Fermi level in the conduction band and, thus, increases the optical gap (Chakrabarti *et al.,* 2016). The significant reduction in the band gap, as shown in Table 4.10 at about 55–65 °C, could also imply structural changes or increased surface defects that create mid-gap states that enable absorption sub-bandgap, thereby lowering the optical band gap (Munirah *et al.,* 2017). A similar

trend has also been observed by (Üzar, 2025) in Fe-doped ZnO NPs synthesized by hydrothermal and sol-gel methods, where the thermal treatment optimized the defects and homogeneity of Fe in ZnO lattice, resulting in the reduced band gap in the range of 3.2-3.6 eV.

Table 4.10: Band gap values of Fe: ZnO NPs at Varying Growth Temperatures

Growth Temperature ^{0}C	**Band gap (eV)**
Room Temperature (RT)	4.43
35	4.12
45	3.84
55	3.25
65	3.0
75	4.12
85	4.60
95	4.88

The overall tunable band gaps found in this study (3.0–4.88 eV) are wider than those already reported, which suggests the ability to achieve a significant level of structural and electronic variation by controlling the temperature. This tunability will be particularly important when applying Fe: ZnO nanocomposites for UV photodetectors, photocatalysts, and transparent conduction oxides; these applications have distinct band gap impedances that are critical to device performance *(Jenish et al.,* 2022).

4.3.5 FTIR Analysis

FTIR spectroscopy using Fourier Transform technology was utilized to study the chemical bonding and changes in functional groups in iron-doped zinc oxide Fe: ZnO NPs synthesized at different growth temperatures. Figure 4.14 shows the FTIR spectra, which indicate strong absorption bands linked to the ZnO structure and dopant incorporation. The wide absorption band near 917 cm^{-1} is attributed to Zn–O stretching vibrations, confirming the wurtzite structure of ZnO. In all synthesized samples, this band is observed, though its intensity and sharpness vary with temperature. At lower growth temperatures (RT to 45°C), the Zn–O peak appears broader and less intense, suggesting lower crystallinity and incomplete phase formation (Dejene, 2022). As the

temperature reaches 75–95 °C, the Zn–O vibration grows stronger and sharper, implying that the higher thermal energy ensures enhanced bond order, hence better lattice formation. A medium-strength peak observed at 1380 cm^{-1} is linked to acetate groups or C-O adsorbed during the synthesis and drying of the material. This decline occurs with rising temperature, and it enhances how firmly the organic remnants bind to the gel (Raja *et al.,* 2014). The band at 2390 cm^{-1} is associated with NO_3^- symmetrical vibrations and could be present in initial nitrate precursors or in small, adsorbed species (Cintrón & Hinchliffe, 2015). Most importantly, a peak observed at 3184 cm^{-1} is seen in all samples, which is attributed to O–H bending vibration of water or hydroxyl groups at the surface (Panwar *et al.,* 2015).

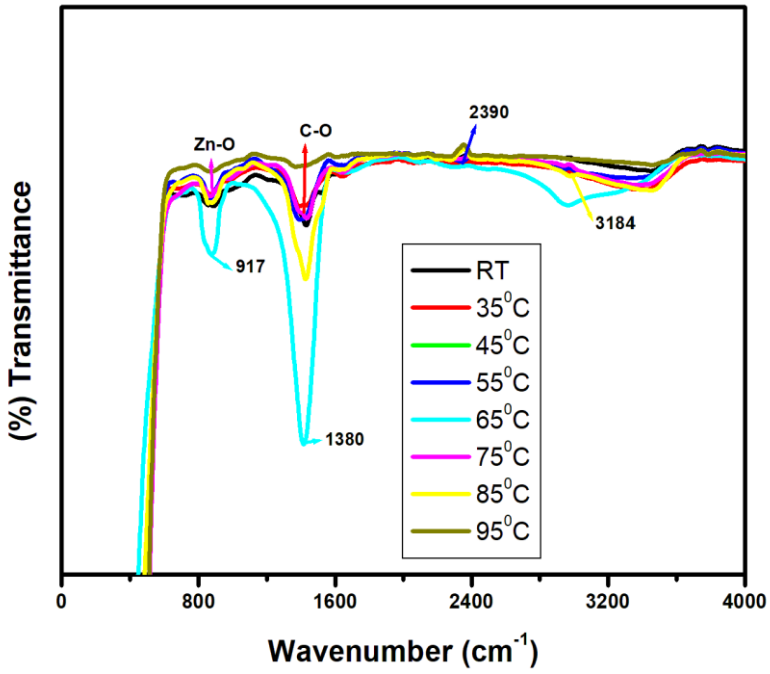


Figure 4.14: FTIR Spectra of Fe: ZnO NPs at Different Growth temperatures

Overall, as the growth temperature was raised gradually, the Zn–O bond was enhanced, minimizing organic impurities and iron incorporation without disrupting the ZnO lattice. These findings are in line with (Pratomo *et al.,* 2025), who concluded that doped ZnO synthesized at higher temperatures has a reduced number of defects and increased crystallinity. Likewise, (Shrivastava et al., 2018) noticed that metal–oxygen bonds became more intense as the temperature increased, confirming observed findings. All synthesized samples between 65–85 °C have surface hydroxyl groups,

do not display carbonaceous or nitrate residues at high temperature, and thus are considered ideal for bioimaging (Nyabadza *et al.,* 2023). Such conditions reach the best possible result for crystallinity, controlling the doping process and the surface properties of Fe-ZnO, especially for photostability, activities, and compatibility in biological systems used in imaging.

4.4 Effects of Glutathione Concentration Used as a Capping Agent on the Structural, Optical, and Photoluminescence Properties of Fe: ZnO NPs.

4.4.1 XRD Analysis

The structural and optical properties of sol-gel synthesized Fe-doped ZnO (Fe: ZnO) nanoparticles capped with various concentrations of glutathione (GSH) were examined using X-ray diffraction (XRD). Figure 4.15 shows diffraction patterns which substantiate the facts that all samples, irrespective of the GSH concentration, exhibited the hexagonal wurtzite phase of ZnO according to (JCPDS card no. 01-070-8072), no extra phase, such as iron oxide or GSH derivatives, were observed. This indicates successful incorporation of Fe without phase segregation and non-destructive performance of GSH as a capping agent.

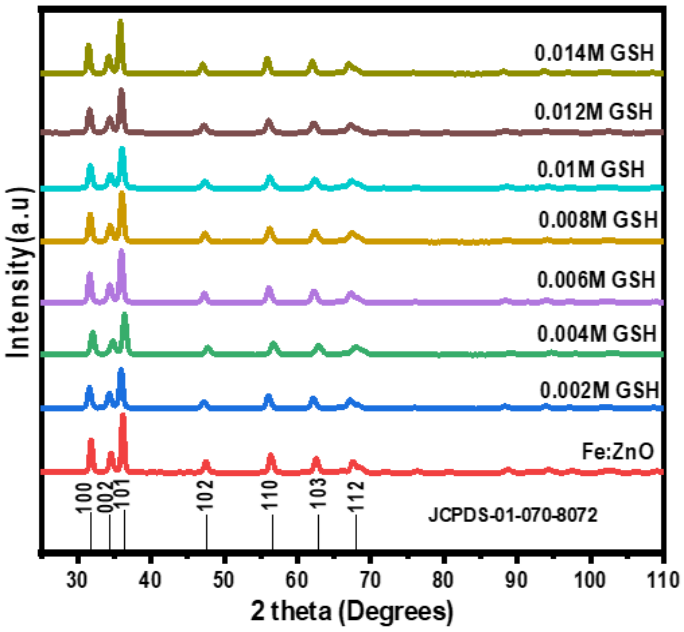


Figure 4.15: XRD pattern for Fe: ZnO NPs and GSH-capped Fe: ZnO NPs at different GSH concentrations

The summarized data in Table 4.11 show that the most intense diffraction peak observed at approximately 38° corresponds to the (101) plane, a dominant feature in the hexagonal wurtzite structure of ZnO. Notably, the 2θ position of this peak exhibited a gradual leftward shift—from 38.422° in uncapped Fe: ZnO to 38.065° at 0.014 M GSH concentration, indicating subtle lattice expansion. Such peak shifts usually emerge from internal strain or the substitution of host Zn^{2+} ions (0.74 Å) with smaller Fe^{3+} ions (0.64 Å), which cause slight distortions in the ZnO lattice. However, GSH molecules interacting with nanoparticle surfaces may induce additional tensile strain via steric hindrance or surface passivation, thereby expanding the lattice constants. These observations are consistent with findings of (Tsay & Huang, 2013), who attributed 2θ peak shifts to strain effects introduced by both dopant ions and organic capping agents. The crystallite size, interplanar d spacing were calculated using the Debye-Scherrer formula and Bragg's equation, respectively. The results obtained are summarized in Tables 4.11 and 13. Equation 4.1 gives Bragg's equation (Bett *et al.,* 2024), Equation 4.2 gives the Debye-Scherrer formula (Alagiri *et al.,* 2011).

The calculated average crystallite size (D) from the position of the (101) peak, the most intense, and based on the Scherrer equation, followed a nonlinear behavior with an increase in GSH concentration. Thus, the average crystallite size for the uncapped Fe: ZnO was characterized to be 21.51 nm, which reduced to the minimum of 15.9 nm for a GSH concentration of 0.008 M before increasing again to 21.9 nm at 0.014 M. These observations matches the results obtained by (Iyer *et al.,* 2020) who mentioned that GSH controls the growth of ZnO nanocrystals up to a certain extent, beyond which steric hindrance turns the control against the crystal growth. Moreover, the XRD patterns show that as the concentration of GSH increases, the crystallite size decreases gradually. Larger full width at half maximum FWHM at maximum intensity signifies smaller crystallite size and greater microstrain. For instance, the FWHM of the (101) peak, which was recorded as 0.40882° for the uncapped, was raised to 0.53444° at 0.004 M GSH and then gradually declined with the continuous increase of the GSH concentration, as shown in Figure 4.16. Thus, the trends towards higher values of surface energy and strain as shown at lower GSH concentrations due to smaller crystallite sizes, which are stabilized at higher GSH concentrations. Numerically, the

microstrain (ε) and dislocation density (δ) were also determined to analyse various internal defects and distortions resulting from an interaction with GSH. The strain was calculated using the Williamson-Hall method, shown by equation 4.3 (Mote *et al.,* 2012). And the dislocation was calculated using the Williamson-Smallman equation 4.5.

The values of strain varied from 0.0051 to 0.0066, and dislocation density reached its highest 0.004 M GSH (4.03 x 10^{-5} nm^{-2}) at a smaller size of crystallite size. This is logical as the particles that are smaller in size typically possess greater strain and dislocation density due to the larger surface area to volume ratio. Similar trends of crystallite size, strain, and defect density have been observed in Fe-doped ZnO NPs by (Jeyachitra *et al.,* 2018) where both Fe addition and surface capping affect the micro-strain in tune with the particle size.

Table 4.11: Crystallite sizes, Microstrain, and Dislocation Densities of Synthesized GSH-Capped Fe: ZnO NPs.

	Glutathione (GSH)	Fe: ZnO	0.002 M	0.004 M	0.006 M	0.008 M	0.01 M	0.012 M	0.014 M
2θ (Degrees)	100	34.05	33.84	34.26	33.87	33.94	33.95	33.86	33.73
	002	36.80	36.55	37.03	36.63	36.70	36.71	36.60	36.47
	101	38.42	38.18	38.66	38.22	38.29	38.30	38.20	38.06
β (Degrees)	100	0.4019	0.4897	0.5226	0.4506	0.4669	0.4950	0.4825	0.4268
	002	0.5103	0.5031	0.6803	0.5483	0.5903	0.6633	0.5956	0.5480
	101	0.4688	0.4395	0.4544	0.4990	0.5381	0.4745	0.4419	0.4159
Peak Intensity	100	4322.0	2705.6	2908.3	3846.8	3681.0	2983.6	3078.2	3825.6
	002	2427.5	1830.7	1696.4	2202.4	2018.3	1689.0	1784.1	2225.6
	101	7728.8	5172.5	5302.1	6855 5.8	6427.4	5241.2	0.48192	6946.2
D (nm)	100	20.66	21.95	21.96	16.14	14.63	18.91	20.36	23.50
	002	22.31	22.01	20.31	18.26	15.17	19.61	20.04	20.26
	101	21.56	22.04	19.68	20.20	17.90	19.20	20.29	21.94
Average D (nm)		21.51	22.00	20.65	18.20	15.90	19.24	20.23	21.90
δ		0.0000236	0.0000339	0.0000403	0.0000311	0.0000337	0.0000374	0.0000329	0.0000269
ε		0.005119	0.006172	0.006648	0.005906	0.006135	0.006464	0.006071	0.005514

Table 4.12: Showing lattice Parameters and Average d spacing of GSH-Capped Fe: ZnO NPs

Glutathione (GSH) concentration(M)	2θ (Degrees)	'a'	'c'	Average d spacing (Å)
Fe: ZnO	38.422	1.7834	2.8570	2.3409
0.002	38.180	1.7943	2.8745	2.3552
0.004	36.661	1.7728	2.8400	2.3270
0.006	38.221	1.7924	2.8715	2.3528
0.008	38.294	1.7891	2.8662	2.3485
0.01	38.307	1.7885	2.8653	2.3477
0.012	38.207	1.7931	2.8725	2.3536
0.014	38.065	1.7995	2.8828	2.3621

An increase observed in average interplanar d-spacing values, summarized in Table 13 based on Bragg's Law, exhibits the slight spacing increases with the rise of the GSH concentrations. The d-spacing rose from 2.3409 Å for uncapped Fe: ZnO to 2.3621 Å at 0.014 M GSH, which again suggests that GSH has a lattice-expanding effect that could be attributed to GSH adsorption on the ZnO surface or changes in the charge distribution at the boundary of the lattice (Jamdagni *et al.,* 2018).

This widening of XRD FWHM at lower GSH concentrations of less than 0.008 M is attributed to the effect of the lesser ability of nanoparticles to be stabilized on a surface. With low GSH, only partial nanoparticle surface capping occurs, and thus leads to aggregated nanoparticle deformation by creating a higher lattice strain and defect density (Vorontsov & Tsybulya, 2018). The absence of a uniform passivation also causes inhomogeneous nucleation, giving rise to a variation in the size of the crystallites and microstrain, which contribute to peak broadening. This is reduced when the concentration of GSH approaches 0.008 M, when there is an ideal surface coverage and defects are partially compensated.

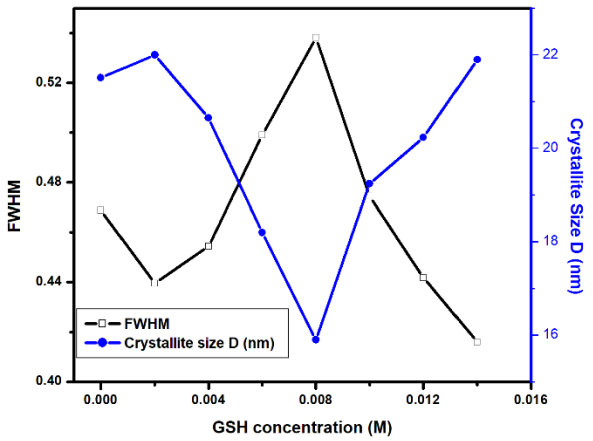


Figure 4.16: Variation of FWHM and Crystallite size at different GSH Capping Concentrations

4.4.2 Photoluminescence Analysis

Figure 4.17a shows the PL spectra of Fe: ZnO and GSH-capped Fe: ZnO NPs at an excitation wavelength of 300 nm, and Figure 4.17b shows the Gaussian deconvolution of one of the synthesized samples recorded at room temperature at an emission range of 250 to 800 nm. This analysis aimed to assess the influence of different concentrations of GSH capping on the deep-level effect emissions and band edge emission of Fe: ZnO and GSH-capped Fe: ZnO NPs.

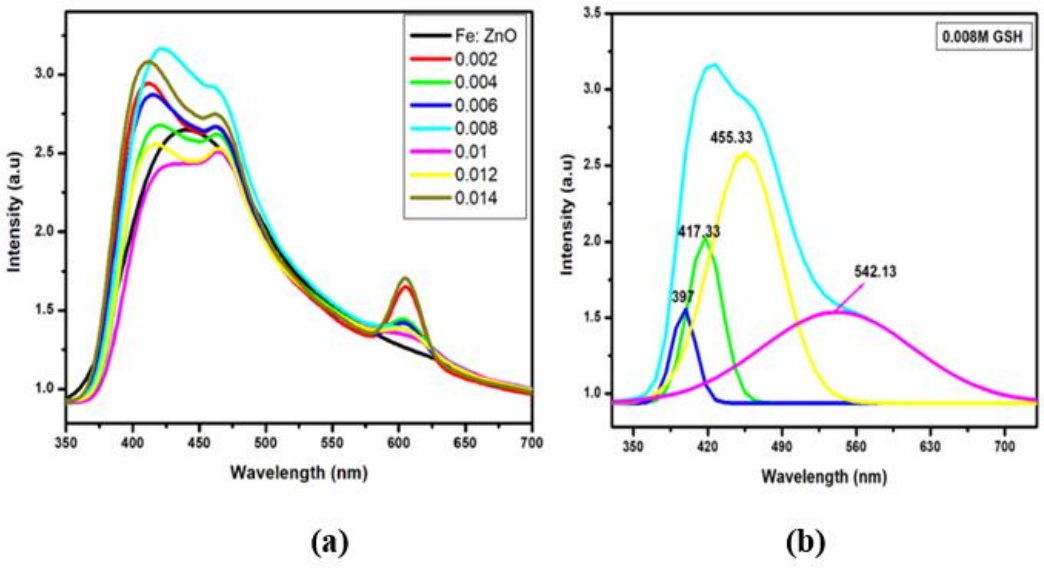


Figure 4.17: (a) PL spectra of synthesized GSH-capped Fe: ZnO NPs at Varying GSH concentrations and PL deconvolution at 0.008M GSH capping (b).

PL spectra of Fe: ZnO NPs and glutathione (GSH) capped Fe: ZnO at different GSH concentrations (0.002 M to 0.014 M) display a characteristic UV emission centered at 390–470 nm, originating from NBE excitonic recombination, and a weak emission peak in the visible region around 540–600 nm, originating from defect-related features. The Fe: ZnO sample exhibits a broad UV emission peak at 454.5 nm and a relatively low PL intensity (1.525 a.u) as shown in Table 4.13. This demonstrates that Fe doping enables a transition to excitonic radiative recombination but also suggests that Fe ions may lead to non-radiative recombination. Adding GSH initially results in an improvement in the PL intensity, steadily increasing up to 0.008 M (1.9973 a.u.), followed by a decline for higher concentrations as surface passivation becomes more pronounced. GSH, a thiol-containing tripeptide, serves as a surface passivating agent by interacting with its SH and carboxyl groups to reduce the density of surface defects (Yang *et al.,* 2025). The capping action minimizes undesirable non-radiative recombination channels while promoting radiative processes within the material, leading to an improvement in the PL intensity at concentrations below 0.008 M. The decrease in PL at higher GSH concentrations suggests that a thick capping film may restrict the mobility of surface carriers or cause energy migration and non-radiative decay (Yang *et al.,* 2025).

This PL peak broadness is attributed mainly to inhomogeneous broadening by the local lattice strain, surface defects, and size variations of the particles of Fe: ZnO NPs. The variations in the crystallite size distribution led to minor variations in the bandgap energy, and overall, the result is a wider emission profile. Also, GSH capping alters surface states and, below the optimal conditions, forms defect sites because of imperfect passivation, leading to multiple overlapping radiative transitions. These aspects, together with the phonons-electron interaction in the nanoscale materials, result in a broader PL emission spectrum than in bulk materials.

PL deconvolution spectra of 0.008 M GSH-capped Fe: ZnO show distinct peaks at 397 nm, 417, 455, and 542 nm that correspond to different recombination mechanisms. The emission peaks at 397 and 417 nm are generally attributed to excitonic recombination and shallow donor defects such as zinc interstitials, whereas the green-yellow emission observed at 542 nm can be linked to deep-level emissions originating

from oxygen vacancies and interstitials (Sarf & Kızıl, 2021). The redistribution of the NBE peak with different GSH concentrations could be a consequence of changes in surface electronic properties or the presence of weakly-bound electron structures (Verma *et al.,* 2015). This behavior has been observed in previous studies focused on varying the surface modification of ZnO NPs. Recently, (Ruiz Peralta *et al.,* 2012) found that the PL intensity of ZnO nanocrystals could be increased after treatment with glutathione. They explained that this was likely due to the interaction between glutathione and defect sites, thereby improving charge carrier recombination. Moreover, Fe impurities present in the ZnO lattice lead to the formation of states below the conduction band, contributing to efficient carrier localization and ultimately, regulating luminescence behavior (Y. Sun *et al.,* 2023).

Table 4.13: Showing the Emission Wavelengths and PL intensities of GSH-Capped Fe: ZnO NPs at different GSH Concentrations.

GSH Concentration (M)	Emission Wavelength (nm)	PL Intensity (a.u)
Fe: ZnO	454.51	1.5250
0.002	441.96	1.6142
0.004	450.77	1.5386
0.006	445.67	1.7170
0.008	446.34	1.9973
0.010	456.47	1.3771
0.012	451.28	1.4207
0.014	440.33	1.7366

4.4.3 Optical Analysis

The absorption spectra and Tauc plots of both Fe: ZnO and GSH-capped Fe: ZnO NPs were examined using UV- Vis spectroscopy. Figure 4.18 shows the absorbance spectra demonstrating a strong absorption in the UV part of the UV-Vis range, and a part of this absorption is seen in the visible spectrum, especially for samples capped with GSH. Among the samples tested, 0.008 M GSH capped Fe: ZnO exhibits the highest absorbance across all wavelengths, showing more defects on its surface and better

binding of GSH to the NPs. Such behavior has been reported by (Sandmann et al., 2015) who observed the same rise in absorbance for ZnO cysteine-functionalized NPs and attributed it to surface binding and the creation of more defects on their surfaces. In addition, the same behavior in absorbance has been found by (Fan *et al.,* 2020), where GSH-modified ZnO quantum dots demonstrated a broadening and strengthening in absorption caused by the transfer of electrons from the ligand to the metal and the appearance of new energy states below the bandgap.

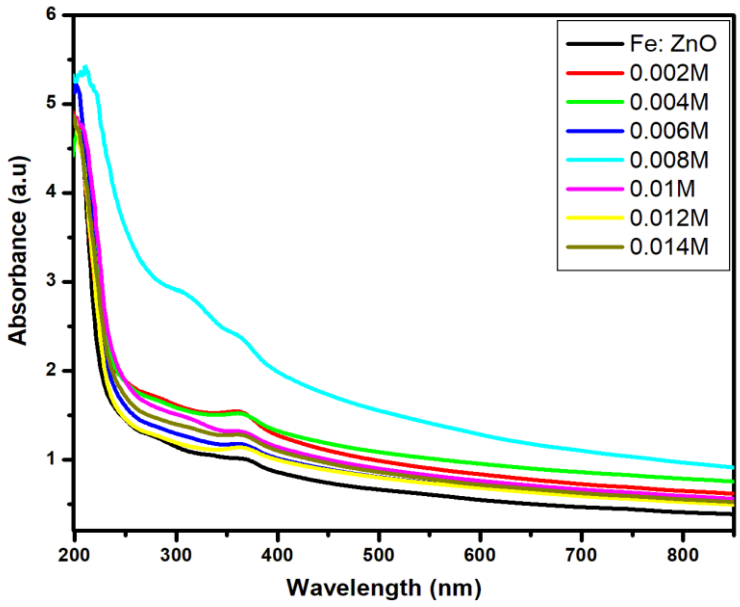


Figure 4.18: Absorbance spectra of Synthesized GSH-Capped Fe: ZnO NPs at different GSH concentrations

To calculate the optical bandgap (E_g) quantitatively, Tauc plots were constructed using the Tauc relation. Equation 4.4 gives the Tauc relation (Madkhali, 2022).

Where α is the absorption coefficient, hv is the photon energy, E_g is the optical bandgap, A is a constant, while n depends on the number of electronic transitions. $n=\frac{1}{2}$ for direct allowed transitions, while n = 2 for indirect allowed transitions. Since ZnO is a direct bandgap semiconductor, $n=\frac{1}{2}$ was used. The Tauc plot was obtained by plotting $(\alpha hv)^2$ against photon energy (hv), and the optical band gap was obtained by extrapolating the linear portion of the curve to the x-axis where $(\alpha hv)^2 = 0$. Figure 4.19 shows the optical band gaps obtained through extrapolation.

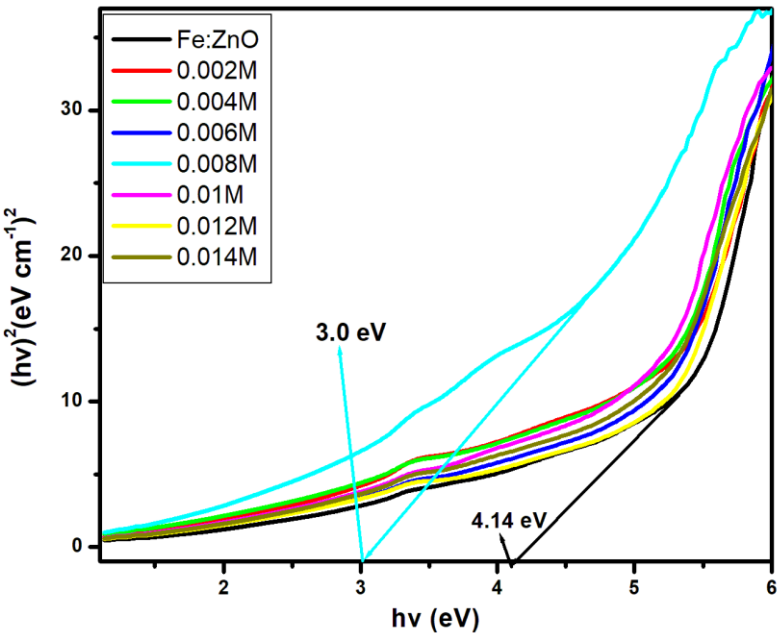


Figure 4.19: Tauc Plot and band gap Extrapolation of Synthesized GSH-capped Fe: ZnO NPs

From the extrapolation in Figure 4.19, the bandgap of Fe: ZnO NPs, measured at 4.14 eV, as shown in Table 4.14, is slightly blue-shifted from that of the standard value of pure ZnO (3.37 eV). This change is attributed to the Burstein–Moss effect and Fe^{3+} atoms being substituted for Zn^{2+} in the material, which introduces localized states within the band structure (X. Yu *et al.,* 2014). When GSH is introduced, the bandgap swiftly drops from the original value to 0.008 M (3.0 eV), then changes in a non-consistent pattern. As the concentration of GSH capping increases, the bandgap is observed to narrow. This indicates better passivation of surface defects and less chance of recombination, which enables optical transitions below the semiconductor bandgap (Choudhury et al., 2016). The GSH molecule, with its –SH and $–NH_2$ groups, can coordinate with the Zn^{2+} ions on the surface of the nanoparticle and modify its potential, which leads to localized states within the gap around the Fe: ZnO NPs (C. Liu *et al.,* 2017). Similarly, the sharpest change in redshift and maximum bandgap narrowing (3.0 eV) was recorded at 0.008 M GSH, which is consistent with the strongest light emitted as seen in PL analysis. This suggests that 0.008 M is the optimal capping concentration to increase light absorption and allow switching between defect states that are important for bioimaging fluorescence. Similar findings have been

reported by (Yang et al., 2025) found that GSH-capped ZnO quantum dots had a narrow band gap and stronger photoluminescence at optimum capping. However, when 0.008 M, the bandgap increases again (4.12 eV at 0.012 M) for the same reason as before: the GSH molecules cover the surface of the nanoparticles so much that an insulating layer forms, limiting the quantum confinement effect (Janek *et al.,* 2020). This also shows a link between the reduced PL brightness at high GSH levels.

Table 4.14: Showing Extrapolated Band Gap Values at each GSH concentration

GSH capping concentration (M)	Band gaps (eV)
Fe: ZnO	4.14
0.002	3.92
0.004	3.85
0.006	3.77
0.008	3.0
0.01	3.82
0.012	4.12
0.014	4.0

The GSH coating allows the Fe: ZnO NPs band gap to be lowered from 4.14 eV to 3.0 eV, supporting their use in customized bioimaging. A smaller bandgap allows visible light to be absorbed, so excitation can be performed with low-energy sources that are useful for live imaging (Julita *et al.,* 2022). The ability of GSH as a capping agent to improve both the solubility and compatibility of NPs, as well as impact the way the material absorbs light, makes it an effective choice for optoelectronic and biomedical devices (Zheng *et al.,* 2007).

4.4.4 FTIR Analysis

The surface chemistry and molecular effects of Glutathione (GSH) capped Fe: ZnO NPs at different GSH concentrations were studied using FT-IR spectroscopy. Prominent vibrations observed in the FTIR spectra in Figure 20 at 400- 4000 cm^{-1} are attributed to Zn–O and Fe–O interactions. GSH features and surface hydroxylation are key elements in maintaining nanoparticle stability and can be functionalized for bioimaging purposes.

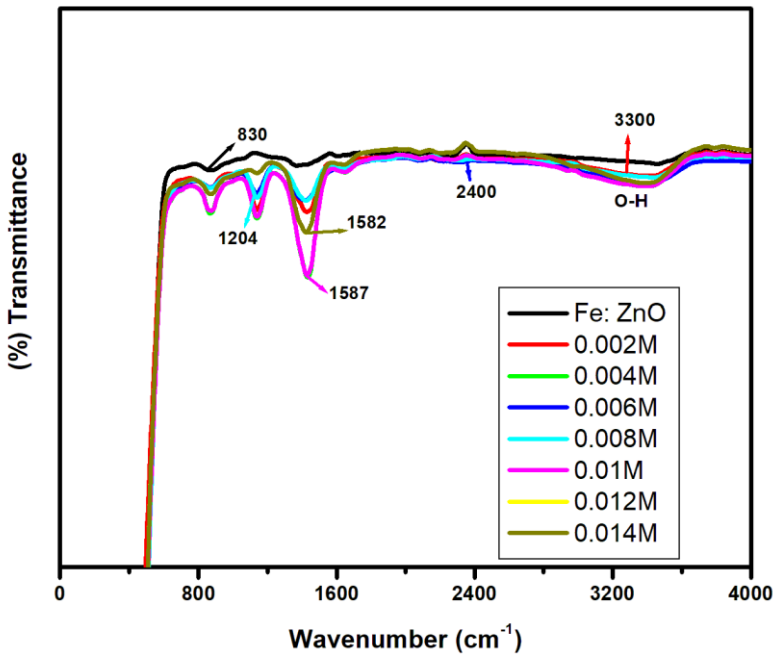


Figure 4.20: FTIR spectra of GSH-capped Fe: ZnO NPs at Different Capping Concentrations

There is a noticeable absorption band at 830 cm^{-1} from Zn–O and Fe-O, likely forming part of the weaker shoulders in this region (Kaningini *et al.,* 2022). This band was found in all parts of the spectra and showed noticeable modulation as GSH concentration increased, indicating that capping influences the local bonding environment within the lattice. The peak does not change with GSH concentration, confirming that the main structure of ZnO is maintained post-functionalization. After adding glutathione, the spectra showed a rise in new peaks, mainly in the range of 1200–1700 cm^{-1}. In particular, absorbance was seen at 1582 cm^{-1} and 1587 cm^{-1}, representing the C=O vibration from glutathione's carboxyl group and the N–H vibration of the primary amines (Andrade *et al.,* 2018). These observations prove that glutathione has been successfully attached to Fe: ZnO NPs. As the GSH concentration rises, the bio-functionalized layer becomes thicker and the bonds between GSH and the nanoparticle surface become stronger. A characteristic peak at 2400 cm^{-1} signals asymmetric stretching of COO^- groups, showing that the carboxylic acid group has been deprotonated and can take part in either binding to metals or covalent bonds on the surface (Max & Chapados, 2002). Also, O–H stretching features appear in all spectra from 3300 to 3500 cm^{-1} and are related to hydroxyl groups and hydrogen

bonds forming on GSH. They increase the tendency of the capped nanoparticles to bond with water and make them more suitable for use in the body (Iyer *et al.,* 2020). Since lipids are kept on the surface at most GSH concentrations, this means capping does not remove necessary properties, but rather adds them to a more active exterior (Yang *et al.,* 2025). In brief, increased GSH levels lead to forming and intensifying specific GSH peaks (N–H, C=O, COO^{-}) without changing the intensity of the Zn–O and Fe–O bond vibrations. The results indicate that glutathione is bonded to the surface of the nanoparticles with its thiol and carboxylate parts, which helps in structural stability and colloidal control. The results match the findings of (Battocchio *et al.,* 2014) who noticed the same change in wavelength when GSH was used to coat gold nanoparticles. Similarly, (Kusworo *et al.*, 2021) found that GSH treatment of ZnO-based materials improved surface functional groups and made them more stable, further proving their suitability for bioimaging. For bioimaging, it is greatly beneficial that the GSH-capped Fe: ZnO NPs have amine, carboxyl, and hydroxyl groups on their outer layer because they enable easy conjugation with biomolecules, thus making them fit for targeted imaging (Kaymaz *et al.,* 2023).

4.7 Summary

This thesis investigated the synthesis and characterization of Iron-doped zinc oxide nanoparticles (Fe: ZnO NPs), focusing on the effects of Fe doping concentration, Growth temperature, and Glutathione (GSH) capping concentration on structural, optical, and photoluminescence (PL) properties. Characterization by X-ray diffraction (XRD) confirmed that all samples retained the hexagonal wurtzite ZnO phase with no secondary phases, indicating successful Fe^{3+} incorporation. Variations in lattice parameters, crystallite size, and microstrain across doping levels and synthesis conditions reflected changes in crystallinity. Optimal Fe doping at 0.45 % yielded balanced crystallinity, reduced lattice defects, a narrowed bandgap of 3.67 eV to 3.02 eV, and enhanced PL, favouring visible-light absorption for bioimaging. Growth temperature strongly influenced particle quality, with 65 °C producing the highest crystallinity, controlled defect levels, a crystallite size of 18.26 nm, strong PL emission of 454 nm, and a reduced bandgap of 3.0 eV. Surface modification with GSH further improved optical performance and biocompatibility, with 0.008 M GSH capping minimizing non-radiative defects, maximizing PL intensity (1.997 a.u),

narrowing the bandgap from 4.14 eV to 3.0 eV, and attaching functional groups including thiol, amine, and carboxyl for enhanced stability. Collectively, the study identifies 0.45% Fe doping, 65 °C growth temperature, and 0.008 M GSH capping as the optimal combination for producing Fe: ZnO nanoparticles with superior structural integrity, defect control, and optical properties suited to bioimaging applications.

CHAPTER FIVE

CONCLUSION AND RECOMMENDATIONS

5.1 Conclusion

This work dealt with the drawbacks of pure ZnO nano-particles ZnO NPs as a good bioimaging material, including low PL intensity, poor structural stability, and uncertain optical properties in the living structure through rational optimization of Fe doping concentration, growth temperature, and GSH capping concentration. The changes were carried out in terms of structural analysis by XRD, optical analysis by UV-Vis and Tauc plots, photoluminescence by (PL), and chemical bonding by FTIR.

On the first objective of varying Fe doping concentration, XRD results showed that all the Fe: ZnO samples had the single-phase hexagonal wurtzite structure with no secondary phases, which indicated the successful Fe^{3+} substitution into the ZnO lattice. Due to the tensile strain caused by increasing concentration of Fe, shifting the peaks to lower 2θ angles and reducing the crystallinity due to defect generation. With doping, crystallite size only shrank with the exception of a temporary resurgence at 0.45% Fe; FWHM was also minimized, peak strength was maximized, and strain partially indicated ideal lattice ordering. The PL spectra revealed quenching of the NBE emission at low Fe doping, 0.15-0.3 % by non-radiative defects, but highly enhanced at 0.45 % Fe, associated with a partial passivation of defects. UV-Vis and Tauc analysis showed a decrease of the bandgap to 3.67 eV for pure ZnO and 3.02 eV at 0.45% Fe, enhancing visible light absorption. The structural integrity was corroborated by FTIR to confirm that the retention of Zn-O stretching was occurring in the presence of Fe without the formation of secondary oxides. These results indicate that the 0.45% Fe doping balances the defect concentration, crystallinity, and optical responses, addressing ZnO low efficiencies of light emission and insufficient absorption bands in bioimaging ranges.

Secondly, on the effect of growth temperature on Fe: ZnO properties, all synthesized samples maintained a hexagonal wurtzite structure throughout the range of 25 to 95°C, as observed in the whole XRD patterns. The crystallinity of the samples also showed an increase with increasing temperature to 65°C, as the peaks were sharper, more intense, and exhibited a small FWHM. At 65°C, the crystallite size decreased to 18

nm, and the microstrain and the dislocation density were very small, resulting in fewer structural defects. The PL intensity was the highest at 65°C, and no strong deep-level emissions were observed, indicating a reduced number of non-radiative centers. UV-Vis demonstrated a decrease in bandgap to 3.0eV at 65 °C, which has been attributed to the enhancement in the crystallinity level and optimization of the defects in the devices. Redshifts and quenching of the PL were observed subsequently at temperatures above 65°C, indicating defect clustering. ZnO and FeO vibrations were better at 65 to 85°C, and fewer organic residues and surface hydroxyls survived, indicating a higher stability with FTIR. Hence, the growth at 65°C produces the optimum compromise of crystallinity, optical absorption, and PL performance that deal directly with the stability and optical tuning problems of ZnO in bioimaging.

Finally, on the effect of GSH capping on Fe: ZnO NPs. XRD confirmed that the GSH capping did not alter the hexagonal wurtzite structure. The GSH broadening below 0.008 M GSH capping signified increased strain and reduced crystallites in consequence of partial surface passivation, whereas the best capping concentration was at 0.008 M, reducing strain and defects. The defect passivation and inhibition of non-radiative recombination caused the increment of the PL intensity with defect passivation and inhibition of the non-radiative recombination up to 0.008M GSH, but restricted the carrier mobility at a thick capping layer, contributing to the drop of PL intensity at higher GSH concentrations. Optical analysis through UV-Vis and Tauc analysis indicated a decrease in band gap to 4.14 eV for pure ZnO and 3.0 eV at 0.008 M GSH, signaling an increase in visible absorption. Effective functionalization of the surface by N-H, C=O, and COO^- groups was confirmed by FTIR and which contributed to the enhanced colloidal stability and biocompatibility. Optimum capping of 0.008 M GSH, therefore, addresses the drawbacks associated with the low dispersion of ZnO and dissolution in biological environments.

Therefore, through systematic optimization, 0.45% Fe doping, 65°C growth temperature, and 0.008 M GSH capping. Fe: ZnO NPs with high crystallinity, optimal defect concentration, a narrower bandgap of 3.0 eV, and strong NBE PL emission intensity were synthesized. Structural stability, optical tunability, and surface compatibility were significantly enhanced, directly addressing the shortcomings of

pure ZnO established in the problem statement. These Fe: ZnO demonstrate great potential for high-contrast, stable, and bio-compatible bioimaging.

5.2 Recommendations

5.2.1 Recommendations for Practice

- Optimized synthesis parameters (0.45 % Fe, 65 ^{0}C, 0.008 M GSH) to be used to synthesize Fe: ZnO NPs to be used as bioimaging agents.
- The anchoring strength between GSH and Fe: ZnO is to be evaluated at various physiological pH levels to determine stability and surface passivation under different biological conditions.

5.2.2 Recommendations for Future

It is possible in future works to co-dope Fe: ZnO with other transition elements or rare-earth elements, e.g., Eu^{3+}, Mn^{2+}, to increase optical emission and control defect states with the aim of bioimaging.

Other properties like surface passivation, optical performance, and biocompatibility should be compared among other biocompatible capping agents, e.g., cysteine, polyethylene glycol.

5.2.3 Recommendations for Policy

Optimization of Synthesis Parameters of Fe: ZnO nanoparticle. Regulatory agencies ought to put in place regulations governing the synthesis of Fe-doped ZnO nanoparticles, such as the ideal concentration of Fe doping, heating temperature, and concentrations of capping materials.

Mandate comprehensive safety reviews: It has been recommended that the government policies provide stringent characterization of toxicity and biocompatibility studies of Fe: ZnO nanoparticles in advance before medical devices and clinical product is accepted. This is essential to determine long-term safety and external effects.

REFERENCES

Abd-Elkader, O. H., Nasrallah, M., Aleya, L., & Nasrallah, M. (2023). Biosynthesis, Optical and Magnetic Properties of Fe-Doped ZnO/C Nanoparticles. *Surfaces*, *6*(4), 410–429. https://doi.org/10.3390/surfaces6040028

Ahammed, N., Hassan, M. S., & Hassan, M. (2018). Effects of aluminum (Al) incorporation on structural, optical and thermal properties of ZnO nanoparticles. *Materials Science-Poland*, *36*(3), 419–426. https://doi.org/10.1515/msp-2018-0018

Akhil, K., Jayakumar, J., Gayathri, G., & Khan, S. S. (2016). Effect of various capping agents on photocatalytic, antibacterial and antibiofilm activities of ZnO nanoparticles. *Journal of Photochemistry and Photobiology B: Biology*, *160*, 32–42. https://doi.org/10.1016/j.jphotobiol.2016.03.015

Alagiri, M., Muthamizhchelvan, C., & Ponnusamy, S. (2011). Structural and magnetic properties of iron, cobalt and nickel nanoparticles. *Synthetic Metals*, *161*(15–16), 1776–1780. https://doi.org/10.1016/j.synthmet.2011.05.030

Alsaad, A. M., Ahmad, A. A., Al-Bataineh, Q. M., Bani-Salameh, A. A., Abdullah, H. S., Qattan, I. A., Albataineh, Z. M., & Telfah, A. D. (2020). Optical, Structural, and Crystal Defects Characterizations of Dip Synthesized (Fe-Ni) Co-Doped ZnO Thin Films. *Materials*, *13*(7), 1737. https://doi.org/10.3390/ma13071737

Amin, L. (2023). Influence of Fe substitution on structural and morphological properties of Zn1-xFexO thin films for varies applications. *Sohag Journal of Sciences*, *0*(0), 0–0. https://doi.org/10.21608/sjsci.2022.153658.1017

Andrade, J., Pereira, C. G., Ranquine, T., Azarias, C. A., Bell, M. J. V., & De Carvalho Dos Anjos, V. (2018). Long-Term Ripening Evaluation of Ewes' Cheeses by Fourier-Transformed Infrared Spectroscopy under Real Industrial Conditions. *Journal of Spectroscopy*, *2018*, 1–9. https://doi.org/10.1155/2018/1381864

Aragón, F. F. H., Villegas-Lelovsky, L., Parizaka, J. G., Zela, E. G., Bendezu, R., Gallegos, R. O., Pacheco-Salazar, D. G., Da Silva, S. W., Cohen, R., Nagamine, L. C. C. M., Coaquira, J. A. H., & Morais, P. C. (2023). Evidence of progressive Fe^{2+} to Fe^{3+}oxidation in Fe^{2+}-doped ZnO nanoparticles. *Materials Advances*, *4*(5), 1389–1402. https://doi.org/10.1039/d3ma00053b

Ayon, S. A., Billah, M. M., & Hossain, M. N. (2023). Effect of annealing temperature on structural, optical, and photocatalytic properties of modified sol–gel-driven ZnO nanoparticles. *Surface and Interface Analysis*, *55*(6–7), 443–449. https://doi.org/10.1002/sia.7203

Bahari, N., Hashim, N., Abdan, K., Md Akim, A., Maringgal, B., & Al-Shdifat, L. (2023). Role of Honey as a Bifunctional Reducing and Capping/Stabilizing Agent: Application for Silver and Zinc Oxide Nanoparticles. *Nanomaterials*, *13*(7), 1244. https://doi.org/10.3390/nano13071244

Battocchio, C., Porcaro, F., Mukherjee, S., Magnano, E., Nappini, S., Fratoddi, I., Quintiliani, M., Russo, M. V., & Polzonetti, G. (2014). Gold Nanoparticles Stabilized with Aromatic Thiols: Interaction at the Molecule–Metal Interface and Ligand Arrangement in the Molecular Shell Investigated by SR-XPS and NEXAFS. *The Journal of Physical Chemistry C*, *118*(15), 8159–8168. https://doi.org/10.1021/jp4126057

Beato-López, J. J., Domínguez, M., Ramírez-del-Solar, M., & Litrán, R. (2020). Glutathione-magnetite nanoparticles: Synthesis and physical characterization for application as MRI contrast agent. *SN Applied Sciences*, *2*(7), 1202. https://doi.org/10.1007/s42452-020-3010-y

Bett, K., Kiprotich, S., Ungula, J., & Andayi, W. (2024). Structural and Optical Properties of ZnO:Al:Ga Co-Doped Nanoparticles: Investigation on the Effects of pH of the Precursor Solution via a Simple Sol-Gel Route. *American Journal of Materials Science*, *14*(2), 21–30.

Bokov, D., Turki Jalil, A., Chupradit, S., Suksatan, W., Javed Ansari, M., Shewael, I. H., Valiev, G. H., & Kianfar, E. (2021). Nanomaterial by Sol-Gel Method: Synthesis and Application. *Advances in Materials Science and Engineering*, *2021*, 1–21. https://doi.org/10.1155/2021/5102014

Carofiglio, M., Barui, S., Cauda, V., & Laurenti, M. (2020). Doped Zinc Oxide Nanoparticles: Synthesis, Characterization and Potential Use in Nanomedicine. *Applied Sciences*, *10*(15), 5194. https://doi.org/10.3390/app10155194

Carofiglio, M., Laurenti, M., Vighetto, V., Racca, L., Barui, S., Garino, N., Gerbaldo, R., Laviano, F., & Cauda, V. (2021). Iron-Doped ZnO Nanoparticles as

Multifunctional Nanoplatforms for Theranostics. *Nanomaterials*, *11*(10), 2628. https://doi.org/10.3390/nano11102628

Chakrabarti, S., Mukherjee, P., Khan, G., Adhikari, A., Patra, P., Bal, J., Roy, A., Ghosh, S., Maitra, S., & Chakrabarti, S. (2016). *Sonochemical Synthesis and Characterization of Iron (Fe) Doped Zinc Oxide (ZnO) Nanoparticles* (pp. 55–61).

Chen, Y., Xue, Q., Luo, W., Sun, Y., Zhang, X., Lu, D., Qian, X., Chen, C.-C., Li, M., & Hang, T. (2022). Sol–Gel-Derived Biodegradable Er-Doped ZnO/Polyethylene Glycol Nanoparticles for Cell Imaging. *ACS Applied Nano Materials*, *5*(5), 7103–7112. https://doi.org/10.1021/acsanm.2c01049

Cheng, W., & Ma, X. (2009). Structural, optical and magnetic properties of Fe-doped ZnO. *Journal of Physics: Conference Series*, *152*, 012039. https://doi.org/10.1088/1742-6596/152/1/012039

Cheng, Z., Janakiraman, A. K., Gunasekaran, B., Lim Siew Ying, C., Mohamad Hanif, E. A. B., Jayasingh Chellammal, H. S., & Djearamane, S. (2024). Unveiling the Biomedical Applications of Zinc Oxide (ZnO) Nanoparticles: A Review Fostering on the Synthesis, Therapeutics and Imaging with Recent Developments. *Pharmaceutical Sciences*, *30*(4), 398–422. https://doi.org/10.34172/PS.2024.24

Choudhury, B., Bayan, S., Choudhury, A., & Chakraborty, P. (2016). Narrowing of band gap and effective charge carrier separation in oxygen deficient TiO 2 nanotubes with improved visible light photocatalytic activity. *Journal of Colloid and Interface Science*, *465*, 1–10. https://doi.org/10.1016/j.jcis.2015.11.050

Cintrón, M., & Hinchliffe, D. (2015). FT-IR Examination of the Development of Secondary Cell Wall in Cotton Fibers. *Fibers*, *3*(1), 30–40. https://doi.org/10.3390/fib3010030

Das, A., Nandi, C. K., & Chakraborty, T. (2003). Structure and electronic spectroscopy of naphthalene–acenaphthene van der Waals dimer: Hole-burning, dispersed fluorescence, and quantum chemistry calculations. *The Journal of Chemical Physics*, *118*(21), 9589–9595. https://doi.org/10.1063/1.1569476

Dasuki, D., Habanjar, K., & Awad, R. (2023). Effect of Growth and Calcination Temperatures on the Optical Properties of Ruthenium-Doped ZnO Nanoparticles. *Condensed Matter*, *8*(4), 102. https://doi.org/10.3390/condmat8040102

Davoodi, Y., & Shafeeyan, M. S. (2024). Tailoring photocatalytic performance through Fe-doped TiO2/ZnO for effective remediation of organic contaminants. *Water Resources and Industry*, *31*, 100239. https://doi.org/10.1016/j.wri.2024.100239

Dejene, F. B. (2022). Characterization of low-temperature-grown ZnO nanoparticles: The effect of temperature on growth. *Journal of Physics Communications*, *6*(7), 075011. https://doi.org/10.1088/2399-6528/ac8049

Dey, A., Guha Ray, P., Dhara, S., & Neogi, S. (2022). Optically engineered ZnO Nanoparticles: Excitable at visible wavelength and lowered cytotoxicity towards bioimaging applications. *Applied Surface Science*, *592*, 153303. https://doi.org/10.1016/j.apsusc.2022.153303

Djurišić, A. B., & Leung, Y. H. (2006). Optical Properties of ZnO Nanostructures. *Small*, *2*(8–9), 944–961. https://doi.org/10.1002/smll.200600134

Djurišić, A. B., Ng, A. M. C., & Chen, X. Y. (2010). ZnO nanostructures for optoelectronics: Material properties and device applications. *Progress in Quantum Electronics*, *34*(4), 191–259. https://doi.org/10.1016/j.pquantelec.2010.04.001

Eixenberger, J. E., Anders, C. B., Wada, K., Reddy, K. M., Brown, R. J., Moreno-Ramirez, J., Weltner, A. E., Karthik, C., Tenne, D. A., Fologea, D., & Wingett, D. G. (2019). Defect Engineering of ZnO Nanoparticles for Bioimaging Applications. *ACS Applied Materials & Interfaces*, *11*(28), 24933–24944. https://doi.org/10.1021/acsami.9b01582

Esbergenova, A., Hojamberdiev, M., Kadirova, Z. C., Sugai, Y., Mamatkulov, S., Jalolov, R., Kong, D., Qin, X., Daminova, S. S., Ruzimuradov, O., & Shaislamov, U. (2024). Interlinking the Fe doping concentration, optoelectronic properties, and photocatalytic performance of ZnO nanostructures. *Current Applied Physics*, *67*, 18–29. https://doi.org/10.1016/j.cap.2024.07.009

Fakhari, S., Jamzad, M., & Kabiri Fard, H. (2019). Green synthesis of zinc oxide nanoparticles: A comparison. *Green Chemistry Letters and Reviews*, *12*(1), 19–24. https://doi.org/10.1080/17518253.2018.1547925

Fan, Q., Cui, X., Guo, H., Xu, Y., Zhang, G., & Peng, B. (2020). Application of rare earth-doped nanoparticles in biological imaging and tumor treatment. *Journal of Biomaterials Applications*, *35*(2), 237–263. https://doi.org/10.1177/0885328220924540

Fathima, F., Mani, R. J., Kathiresan, S., Manimala, K., & Hossain, A. (2020). Enhanced Antifungal Activity of Pure and Iron-Doped ZnO Nanoparticles Prepared in the Absence of Reducing Agents. *Journal of Inorganic and Organometallic Polymers and Materials*, *30*, 1–9. https://doi.org/10.1007/s10904-019-01400-z

Flannigan, J. M., MacIver, D., Jolliffe, H., Haw, M. D., & Sefcik, J. (2023). Nucleation and Growth Kinetics of Sodium Chloride Crystallization from Water and Deuterium Oxide. *Crystals*, *13*(9), 1388. https://doi.org/10.3390/cryst13091388

George, S., Pokhrel, S., Xia, T., Gilbert, B., Ji, Z., Schowalter, M., Rosenauer, A., Damoiseaux, R., Bradley, K. A., Mädler, L., & Nel, A. E. (2010). Use of a Rapid Cytotoxicity Screening Approach To Engineer a Safer Zinc Oxide Nanoparticle through Iron Doping. *ACS Nano*, *4*(1), 15–29. https://doi.org/10.1021/nn901503q

Gorokhova, E. I., Anan'eva, G. V., Demidenko, V. A., Rodnyĭ, P. A., Khodyuk, I. V., & Bourret-Courchesne, E. D. (2008). Optical, luminescence, and scintillation properties of ZnO and ZnO:Ga ceramics. *Journal of Optical Technology*, *75*(11), 741. https://doi.org/10.1364/JOT.75.000741

Gudla, U. R., Suryanarayana, B., Raghavendra, V., Emmanuel, K. A., Murali, N., Taddesse, P., Parajuli, D., Chandra Babu Naidu, K., Ramakrishna, Y., & Chandramouli, K. (2020). Optical and luminescence properties of pure, iron-doped, and glucose capped ZnO nanoparticles. *Results in Physics*, *19*, 103508. https://doi.org/10.1016/j.rinp.2020.103508

Hadimani, P. L., Ghosh, S. S., & Sil, A. (2018). Preparation of Fe doped ZnO thin films and their structural, magnetic, electrical characterization. *Superlattices*

and Microstructures, *120*, 199–208. https://doi.org/10.1016/j.spmi.2018.05.029

Hasnidawani, J. N., Azlina, H. N., Norita, H., Bonnia, N. N., Ratim, S., & Ali, E. S. (2016). Synthesis of ZnO Nanostructures Using Sol-Gel Method. *Procedia Chemistry*, *19*, 211–216. https://doi.org/10.1016/j.proche.2016.03.095

Hu, S., Li, Y., Kim, D., Liu, M., Lee, L. Y. S., & Wong, K. (2022). Surface modulated Fe doping of β-Ni(OH)$_2$ nanosheets for highly promoted oxygen evolution electrocatalysis. *EcoMat*, *4*(6), e12256. https://doi.org/10.1002/eom2.12256

Ilican, S., Özdemir, Y., Caglar, M., & Caglar, Y. (2016). Temperature dependence of the optical band gap of sol-gel derived Fe-doped ZnO films. *Optik*, *127*(20), 8554–8561. https://doi.org/10.1016/j.ijleo.2016.06.074

Iqbal, T., Hassan, A., Ijaz, M., Salim, M., Farooq, M., Zafar, M., & Tahir, M. B. (2021). Chromium incorporated copper vanadate nano-materials for hydrogen evolution by water splitting. *Applied Nanoscience*, *11*(5), 1661–1671. https://doi.org/10.1007/s13204-021-01786-8

Ivchenko, V. (2024). Theory of Burstein-Moss effect in semiconductors with anisotropic energy bands. *Physica Scripta*, *99*(3), 035952. https://doi.org/10.1088/1402-4896/ad28e5

Iyer, R., Nguyen, T., Padanilam, D., Xu, C., Saha, D., Nguyen, K. T., & Hong, Y. (2020). Glutathione-responsive biodegradable polyurethane nanoparticles for lung cancer treatment. *Journal of Controlled Release*, *321*, 363–371. https://doi.org/10.1016/j.jconrel.2020.02.021

Jagannatha Reddy, A., Kokila, M. K., Nagabhushana, H., Rao, J. L., Shivakumara, C., Nagabhushana, B. M., & Chakradhar, R. P. S. (2011). EPR, thermo and photoluminescence properties of ZnO nanopowders. *Spectrochimica Acta Part A: Molecular and Biomolecular Spectroscopy*, *81*(1), 59–63. https://doi.org/10.1016/j.saa.2011.06.048

Jamdagni, P., Khatri, P., & Rana, J. S. (2018). Green synthesis of zinc oxide nanoparticles using flower extract of Nyctanthes arbor-tristis and their antifungal activity. *Journal of King Saud University - Science*, *30*(2), 168–175. https://doi.org/10.1016/j.jksus.2016.10.002

Janek, T., Sałek, K., Burger, J., Czyżnikowska, Ż., & Euston, S. R. (2020). Investigating the biomolecular interactions between model proteins and

glycine betaine surfactant with reference to the stabilization of emulsions and antimicrobial properties. *Colloids and Surfaces B: Biointerfaces*, *194*, 111226. https://doi.org/10.1016/j.colsurfb.2020.111226

Javed, R., Sajjad, A., Naz, S., Sajjad, H., & Ao, Q. (2022). Significance of Capping Agents of Colloidal Nanoparticles from the Perspective of Drug and Gene Delivery, Bioimaging, and Biosensing: An Insight. *International Journal of Molecular Sciences*, *23*(18), 10521. https://doi.org/10.3390/ijms231810521

Javed, R., Usman, M., Tabassum, S., & Zia, M. (2016). Effect of capping agents: Structural, optical and biological properties of ZnO nanoparticles. *Applied Surface Science*, *386*, 319–326. https://doi.org/10.1016/j.apsusc.2016.06.042

Jenish, S. L., Valanarasu, S., Prakash, B., Veerathangam, K., Vinoth, S., Al-Enizi, A. M., Ubaidullah, M., Reddy, V. R. M., & Karim, A. (2022). Improved optical and electrical properties of Fe doped ZnO nanostructures facilely deposited by low-cost SILAR method for photosensor applications. *Surfaces and Interfaces*, *31*, 102071. https://doi.org/10.1016/j.surfin.2022.102071

Jeyachitra, R., Senthilnathan, V., & Senthil, T. S. (2018). Studies on electrical behavior of Fe doped ZnO nanoparticles prepared via co-precipitation approach for photo-catalytic application. *Journal of Materials Science: Materials in Electronics*, *29*(2), 1189–1197. https://doi.org/10.1007/s10854-017-8021-0

Jha, S., Rani, R., & Singh, S. (2023). Biogenic Zinc Oxide Nanoparticles and Their Biomedical Applications: A Review. *Journal of Inorganic and Organometallic Polymers and Materials*, *33*(6), 1437–1452. https://doi.org/10.1007/s10904-023-02550-x

Ji, H., Cai, C., Zhou, S., & Liu, W. (2018). Structure, photoluminescence, and magnetic properties of Co-doped ZnO nanoparticles. *Journal of Materials Science: Materials in Electronics*, *29*(15), 12917–12926. https://doi.org/10.1007/s10854-018-9411-7

Jiang, J., Pi, J., & Cai, J. (2018). The Advancing of Zinc Oxide Nanoparticles for Biomedical Applications. *Bioinorganic Chemistry and Applications*, *2018*, 1062562. https://doi.org/10.1155/2018/1062562

Julita, M., Shiddiq, M., & Khair, M. (2022). Determination of Band Gap Energy of ZnO/Au Nanoparticles Resulting in Laser Ablation in Liquid. *Indo. J. Chem. Res.*, *10*(2), 83–87. https://doi.org/10.30598//ijcr.2022.10-mar

Kaningini, A. G., Azizi, S., Sintwa, N., Mokalane, K., Mohale, K. C., Mudau, F. N., & Maaza, M. (2022). Effect of Optimized Precursor Concentration, Temperature, and Doping on Optical Properties of ZnO Nanoparticles Synthesized via a Green Route Using Bush Tea (*Athrixia phylicoides* DC.) Leaf Extracts. *ACS Omega*, *7*(36), 31658–31666. https://doi.org/10.1021/acsomega.2c00530

Kavita, Singh, K., Kumar, S., & Bhatti, H. S. (2014). Glutathione-assisted synthesis of star-shaped zinc oxide nanostructures and their photoluminescence behavior. *Journal of Luminescence*, *149*, 112–117. https://doi.org/10.1016/j.jlumin.2014.01.001

Kayani, Z. N., Bashir, Z., Riaz, S., Naseem, S., & Saddiqe, Z. (2020). Transparent boron-doped zinc oxide films for antibacterial and magnetic applications. *Journal of Materials Science: Materials in Electronics*, *31*(14), 11911–11926. https://doi.org/10.1007/s10854-020-03745-5

Kaymaz, S. V., Nobar, H. M., Sarıgül, H., Soylukan, C., Akyüz, L., & Yüce, M. (2023). Nanomaterial surface modification toolkit: Principles, components, recipes, and applications. *Advances in Colloid and Interface Science*, *322*, 103035. https://doi.org/10.1016/j.cis.2023.103035

Kumar, P., Kumar, S., Tapwal, A., Nimesh, S., & Thakur, N. (2024). Water purification and biological efficacy of green synthesized Co/Zn-Doped α-Fe2O3 nanoparticles. *Sustainable Chemistry for the Environment*, *8*, 100160. https://doi.org/10.1016/j.scenv.2024.100160

Kumar, S., Kavita, Bhatti, H. S., Singh, K., Gupta, S., Sharma, S., Kumar, V., & Choubey, R. K. (2021). Effect of glutathione capping on the antibacterial activity of tin doped ZnO nanoparticles. *Physica Scripta*, *96*(12), 125807. https://doi.org/10.1088/1402-4896/ac1eb3

Kumawat, A., Chattopadhyay, S., Verma, R. K., & Misra, K. P. (2022). Eu doped ZnO nanoparticles with strong potential of thermal sensing and bioimaging. *Materials Letters*, *308*, 131221. https://doi.org/10.1016/j.matlet.2021.131221

Kurul, F., Turkmen, H., Cetin, A. E., & Topkaya, S. N. (2025). Nanomedicine: How nanomaterials are transforming drug delivery, bio-imaging, and diagnosis. *Next Nanotechnology*, *7*, 100129. https://doi.org/10.1016/j.nxnano.2024.100129

Kusworo, T. D., Dalanta, F., Aryanti, N., & Othman, N. H. (2021). Intensifying separation and antifouling performance of PSf membrane incorporated by GO and ZnO nanoparticles for petroleum refinery wastewater treatment. *Journal of Water Process Engineering*, *41*, 102030. https://doi.org/10.1016/j.jwpe.2021.102030

LeCompte, M. C., & Brawley, O. W. (2023). The Cause of Death in Patients With Cancer. *JACC: CardioOncology*, *5*(1), 67. https://doi.org/10.1016/j.jaccao.2023.01.004

Lin, H., Huang, C., Li, W., Ni, C., Shah, S., & Tseng, Y. (2006). Size dependency of nanocrystalline TiO2 on its optical property and photocatalytic reactivity exemplified by 2-chlorophenol. *Applied Catalysis B: Environmental*, *68*(1–2), 1–11. https://doi.org/10.1016/j.apcatb.2006.07.018

Liu, C., Ding, Y., Li, Q., & Lin, Y. (2017). Photochemical synthesis of glutathione-stabilized silver nanoclusters for fluorometric determination of hydrogen peroxide. *Microchimica Acta*, *184*(7), 2497–2503. https://doi.org/10.1007/s00604-017-2302-4

Liu, C., Meng, D., Pang, H., Wu, X., Xie, J., Yu, X., Chen, L., & Liu, X. (2012). Influence of Fe-doping on the structural, optical and magnetic properties of ZnO nanoparticles. *Journal of Magnetism and Magnetic Materials*, *324*(20), 3356–3360. https://doi.org/10.1016/j.jmmm.2012.05.054

Liu, Y., Ai, K., Yuan, Q., & Lu, L. (2011). Fluorescence-enhanced gadolinium-doped zinc oxide quantum dots for magnetic resonance and fluorescence imaging. *Biomaterials*, *32*(4), 1185–1192. https://doi.org/10.1016/j.biomaterials.2010.10.022

Liu, Y., Luo, W., Li, R., & Chen, X. (2010). Optical Properties of Nd^{3+} Ion-Doped ZnO Nanocrystals. *Journal of Nanoscience and Nanotechnology*, *10*(3), 1871–1876. https://doi.org/10.1166/jnn.2010.2140

Madkhali, N. (2022). Analysis of Structural, Optical, and Magnetic Properties of (Fe,Co) Co-Doped ZnO Nanoparticles Synthesized under UV Light. *Condensed Matter*, *7*(4), 63. https://doi.org/10.3390/condmat7040063

Mahmood, M. A., Jan, S., Shah, I. A., & Khan, I. (2016). Growth Parameters for Films of Hydrothermally Synthesized One-Dimensional Nanocrystals of Zinc Oxide. *International Journal of Photoenergy*, *2016*, 1–12. https://doi.org/10.1155/2016/3153170

Manzoor, U., Tuz Zahra, F., Rafique, S., Moin, M. T., & Mujahid, M. (2015). Effect of Synthesis Temperature, Nucleation Time, and Postsynthesis Heat Treatment of ZnO Nanoparticles and Its Sensing Properties. *Journal of Nanomaterials*, *2015*(1), 189058. https://doi.org/10.1155/2015/189058

Max, J.-J., & Chapados, C. (2002). Infrared Spectroscopy of Aqueous Carboxylic Acids: Malic Acid. *The Journal of Physical Chemistry A*, *106*(27), 6452–6461. https://doi.org/10.1021/jp014377i

Maysinger, D., Ji, J., Hutter, E., & Cooper, E. (2015). Nanoparticle-Based and Bioengineered Probes and Sensors to Detect Physiological and Pathological Biomarkers in Neural Cells. *Frontiers in Neuroscience*, *9*. https://doi.org/10.3389/fnins.2015.00480

Mohamed Basith, N., Judith Vijaya, J., John Kennedy, L., Bououdina, M., Shenbhagaraman, R., & Jayavel, R. (2016). Influence of Fe-Doping on the Structural, Morphological, Optical, Magnetic and Antibacterial Effect of ZnO Nanostructures. *Journal of Nanoscience and Nanotechnology*, *16*(2), 1567–1577. https://doi.org/10.1166/jnn.2016.10756

Molla, A., Hoque, M. M., Richi, F. T., Kabir, M. H., Alam, S., Ahmed, N. U., Emon, N. U., Shao, C., Zeng, C., Wang, S., Geng, P., & Mamun, A. A. (2025). Biosynthesis and Characterization of ZnO Nanoparticles Using Citrus reticulata Peel Followed by Photocatalytic, Antibacterial, and Antioxidative Nanotherapeutic Attributes Assessment Supported by Computer Simulation. *International Journal of Nanomedicine*, *Volume 20*, 4803–4829. https://doi.org/10.2147/IJN.S493905

Mote, V., Purushotham, Y., & Dole, B. (2012). Williamson-Hall analysis in estimation of lattice strain in nanometer-sized ZnO particles. *Journal of Theoretical and Applied Physics*, *6*(1), 6. https://doi.org/10.1186/2251-7235-6-6

Mufti, N., Laila, I. K. R., Idiawati, R., Fuad, A., Hidayat, A., Taufiq, A., & Sunaryono. (2018). The Effect of Growth Temperature on The Characteristics Of ZnO Nanorods And Its Optical Properties. *Journal of Physics: Conference Series*, *1057*, 012005. https://doi.org/10.1088/1742-6596/1057/1/012005

Munirah, Khan, Z. R., Aziz, A., Khan, Mohd. S., & Khandaker, M. U. (2017). Influence of zinc concentration on band gap and sub-band gap absorption on ZnO nanocrystalline thin films sol-gel grown. *Materials Science-Poland*, *35*(1), 246–253. https://doi.org/10.1515/msp-2017-0039

Murkute, P., Ghadi, H., Sreedhara, S., & Chakrabarti, S. (2019). Detailed investigation of photoluminescence, structural, and elemental properties of ZnO thin films under various annealing ambient. *Superlattices and Microstructures*, *136*, 106310. https://doi.org/10.1016/j.spmi.2019.106310

Musa, I., Qamhieh, N., & Mahmoud, S. T. (2017). Synthesis and length dependent photoluminescence property of zinc oxide nanorods. *Results in Physics*, *7*, 3552–3556. https://doi.org/10.1016/j.rinp.2017.09.035

Nabil, M., Perez-Quintana, I. V., Acosta, M., Mendez-Gamboa, J. A., & Castro-Rodriguez, R. (2021). Morphological, Structural, and Optical Bandgap Characterization of Extracted ZnO Nanoparticles from Commercial Paste. *Advances in Materials Science and Engineering*, *2021*(1), 9926544. https://doi.org/10.1155/2021/9926544

Naik, E. I., Naik, H. S. B., Swamy, B. E. K., Viswanath, R., Gowda, I. K. S., Prabhakara, M. C., & Chetankumar, K. (2021). Influence of Cu doping on ZnO nanoparticles for improved structural, optical, electrochemical properties and their applications in efficient detection of latent fingerprints. *Chemical Data Collections*, *33*, 100671. https://doi.org/10.1016/j.cdc.2021.100671

Nguyen, H., Tinet, E., Chauveau, T., Geinguenaud, F., Lalatonne, Y., Michel, A., Aid-Launais, R., Journé, C., Lefèbvre, C., Simon-Yarza, T., Motte, L., Jouini, N., Tualle, J.-M., & Chaubet, F. (2019). Bimodal Fucoidan-Coated Zinc Oxide/Iron Oxide-Based Nanoparticles for the Imaging of Atherothrombosis. *Molecules*, *24*(5), 962. https://doi.org/10.3390/molecules24050962

Nyabadza, A., McCarthy, É., Makhesana, M., Heidarinassab, S., Plouze, A., Vazquez, M., & Brabazon, D. (2023). A review of physical, chemical and biological synthesis methods of bimetallic nanoparticles and applications in sensing,

water treatment, biomedicine, catalysis and hydrogen storage. *Advances in Colloid and Interface Science*, *321*, 103010. https://doi.org/10.1016/j.cis.2023.103010

Pal Singh, R. P., Hudiara, I. S., & Bhushan Rana, S. (2016). Effect of calcination temperature on the structural, optical and magnetic properties of pure and Fe-doped ZnO nanoparticles. *Materials Science-Poland*, *34*(2), 451–459. https://doi.org/10.1515/msp-2016-0059

Panigrahy, B., Aslam, M., & Bahadur, D. (2012). Effect of Fe doping concentration on optical and magnetic properties of ZnO nanorods. *Nanotechnology*, *23*(11), 115601. https://doi.org/10.1088/0957-4484/23/11/115601

Panwar, K., Jassal, M., & Agrawal, A. K. (2015). In situ synthesis of Ag–SiO2 Janus particles with epoxy functionality for textile applications. *Particuology*, *19*, 107–112. https://doi.org/10.1016/j.partic.2014.06.007

Parashar, M., Shukla, V. K., & Singh, R. (2020). Metal oxides nanoparticles via sol–gel method: A review on synthesis, characterization and applications. *Journal of Materials Science: Materials in Electronics*, *31*(5), 3729–3749. https://doi.org/10.1007/s10854-020-02994-8

Parveen, A., Thakur, P., Sharma, N., Kumar, A. S., Lekha, C. S. C., Kumar, P., & Lal, M. (2024). Microstructural, optical, dielectric, and magnetic properties of multifunctional Zn1-x FexO nanoparticles. *Journal of Optics*. https://doi.org/10.1007/s12596-024-02377-w

Perveen, R., Shujaat, S., Qureshi, Z., Nawaz, S., Khan, M. I., & Iqbal, M. (2020). Green versus sol-gel synthesis of ZnO nanoparticles and antimicrobial activity evaluation against panel of pathogens. *Journal of Materials Research and Technology*, *9*(4), 7817–7827. https://doi.org/10.1016/j.jmrt.2020.05.004

Pratomo, U., Fransisca, N., Adzani, M. D., Irkham, I., Sulaeman, A. P., Eddy, D. R., Mulyana, J. Y., & Primadona, I. (2025). Doping of rare earth element: The effects in elevated physical and optical properties of ZnO. *Talanta Open*, *11*, 100411. https://doi.org/10.1016/j.talo.2025.100411

Pupilli, F., Tavoni, M., Drouet, C., Tampieri, A., & Sprio, S. (2024). Iron-doped hydroxyapatite by hydrothermal synthesis: Factors modulating the Fe2+, Fe3+ content. *Open Ceramics*, *18*, 100610. https://doi.org/10.1016/j.oceram.2024.100610

Raciti, R., Bahariqushchi, R., Summonte, C., Aydinli, A., Terrasi, A., & Mirabella, S. (2017). Optical bandgap of semiconductor nanostructures: Methods for experimental data analysis. *Journal of Applied Physics*, *121*(23), 234304. https://doi.org/10.1063/1.4986436

Radoń, A., Drygała, A., Hawełek, Ł., & Łukowiec, D. (2017). Structure and optical properties of Fe 3 O 4 nanoparticles synthesized by co-precipitation method with different organic modifiers. *Materials Characterization*, *131*, 148–156. https://doi.org/10.1016/j.matchar.2017.06.034

Raja, K., Ramesh, P. S., & Geetha, D. (2014). Structural, FTIR and photoluminescence studies of Fe doped ZnO nanopowder by co-precipitation method. *Spectrochimica Acta Part A: Molecular and Biomolecular Spectroscopy*, *131*, 183–188. https://doi.org/10.1016/j.saa.2014.03.047

Rasmussen, J. W., Martinez, E., Louka, P., & Wingett, D. G. (2010). Zinc oxide nanoparticles for selective destruction of tumor cells and potential for drug delivery applications. *Expert Opinion on Drug Delivery*, *7*(9), 1063–1077. https://doi.org/10.1517/17425247.2010.502560

Rathore, M. S., Verma, H., Akhani, S. B., Pathak, J., Joshi, U., Joshi, A., Prakash, C., Kaur, K., & Oza, A. (2024). Photoluminescence and antibacterial performance of sol–gel synthesized ZnO nanoparticles. *Materials Advances*, *5*(8), 3472–3481. https://doi.org/10.1039/D3MA01096A

Reddy, M. V., Cherian, C. T., Ramanathan, K., Jie, K. C. W., Daryl, T. Y. W., Hao, T. Y., Adams, S., Loh, K. P., & Chowdari, B. V. R. (2014). Molten synthesis of ZnO.Fe3O4 and Fe2O3 and its electrochemical performance. *Electrochimica Acta*, *118*, 75–80. https://doi.org/10.1016/j.electacta.2013.11.125

Restrepo, C. V., & Villa, C. C. (2021). Synthesis of silver nanoparticles, influence of capping agents, and dependence on size and shape: A review. *Environmental Nanotechnology, Monitoring & Management*, *15*, 100428. https://doi.org/10.1016/j.enmm.2021.100428

Rizwan, M., Ali, S., Ali, B., Adrees, M., Arshad, M., Hussain, A., Zia Ur Rehman, M., & Waris, A. A. (2019). Zinc and iron oxide nanoparticles improved the plant growth and reduced the oxidative stress and cadmium concentration in

wheat. *Chemosphere*, *214*, 269–277. https://doi.org/10.1016/j.chemosphere.2018.09.120

Rodnyi, P. A., & Khodyuk, I. V. (2011). Optical and luminescence properties of zinc oxide (Review). *Optics and Spectroscopy*, *111*(5), 776–785. https://doi.org/10.1134/S0030400X11120216

Rosowska, J., Kaszewski, J., Witkowski, B., Wachnicki, Ł., Kuryliszyn-Kudelska, I., & Godlewski, M. (2020). The effect of iron content on properties of ZnO nanoparticles prepared by microwave hydrothermal method. *Optical Materials*, *109*, 110089. https://doi.org/10.1016/j.optmat.2020.110089

Roy, S., Ghosh, M. P., & Mukherjee, S. (2021). *Introducing the magnetic properties in Fe doped ZnO nanoparticles for spintronics application*. https://doi.org/10.21203/rs.3.rs-180286/v1

Ruiz Peralta, Ma. D. L., Pal, U., & Zeferino, R. S. (2012). Photoluminescence (PL) Quenching and Enhanced Photocatalytic Activity of Au-Decorated ZnO Nanorods Fabricated through Microwave-Assisted Chemical Synthesis. *ACS Applied Materials & Interfaces*, *4*(9), 4807–4816. https://doi.org/10.1021/am301155u

Saha, H., Dastider, A., Ferdous Anik, M. J., Mim, S. R., Talapatra, S., Das, U., Jamal, M., & Billah, M. M. (2024). Photocatalytic performance of CuO NPs: An experimental approach for process parameter optimization for Rh B dye. *Results in Materials*, *24*, 100614. https://doi.org/10.1016/j.rinma.2024.100614

Sahoo, R. K., Rani, S., Kumar, V., & Gupta, U. (2021). Zinc oxide nanoparticles for bioimaging and drug delivery. In *Nanostructured Zinc Oxide* (pp. 483–509). Elsevier. https://doi.org/10.1016/B978-0-12-818900-9.00021-8

Salaken, S. M., Farzana, E., & Podder, J. (2013). Effect of Fe-doping on the structural and optical properties of ZnO thin films prepared by spray pyrolysis. *Journal of Semiconductors*, *34*(7), 073003. https://doi.org/10.1088/1674-4926/34/7/073003

Samanta, S., Muralidhar, M., Sankaranarayanan, V., Sethupathi, K., Ramachandra Rao, M. S., & Murakami, M. (2017). Band gap reduction and redshift of lattice vibrational spectra in Nb and Fe co-doped PLZT. *Journal of Materials Science*, *52*(22), 13012–13022. https://doi.org/10.1007/s10853-017-1425-7

Sandmann, A., Kompch, A., Mackert, V., Liebscher, C. H., & Winterer, M. (2015). Interaction of L -Cysteine with ZnO: Structure, Surface Chemistry, and Optical Properties. *Langmuir*, *31*(21), 5701–5711. https://doi.org/10.1021/la504968m

Santhi, V., Acharjya, D. P., & Ezhilarasan, M. (Eds.). (2016). *Emerging Technologies in Intelligent Applications for Image and Video Processing:* IGI Global. https://doi.org/10.4018/978-1-4666-9685-3

Sarf, F., & Kızıl, H. (2021). Defect Emission Energy and Particle Size Effects in Fe:ZnO Nanospheres Used in Li-Ion Batteries as Anode. *Journal of Electronic Materials*, *50*(11), 6475–6481. https://doi.org/10.1007/s11664-021-09191-1

Schubert, U. (2015). Chemistry and Fundamentals of the Sol–Gel Process. In D. Levy & M. Zayat (Eds.), *The Sol-Gel Handbook* (1st ed., pp. 1–28). Wiley. https://doi.org/10.1002/9783527670819.ch01

Seshadri, R. (2005). Zinc oxide-based diluted magnetic semiconductors. *Current Opinion in Solid State and Materials Science*, *9*(1–2), 1–7. https://doi.org/10.1016/j.cossms.2006.03.002

Sharma, N., Jandaik, S., Kumar, S., Chitkara, M., & Sandhu, I. S. (2016). Synthesis, characterisation and antimicrobial activity of manganese- and iron-doped zinc oxide nanoparticles. *Journal of Experimental Nanoscience*, *11*(1), 54–71. https://doi.org/10.1080/17458080.2015.1025302

Sharma, P. K., Dutta, R. K., Pandey, A. C., Layek, S., & Verma, H. C. (2009). Effect of iron doping concentration on magnetic properties of ZnO nanoparticles. *Journal of Magnetism and Magnetic Materials*, *321*(17), 2587–2591. https://doi.org/10.1016/j.jmmm.2009.03.043

Shrivastava, V., Pritam, A., & Joshi, A. (2018). Integrating third phase transition and CO/CO2 contamination in microwave tailored Bi2Mo1−xWxO6 nano materials. *Journal of Materials Science: Materials in Electronics*, *29*(20), 17388–17396. https://doi.org/10.1007/s10854-018-9836-z

Singh, M., Atkins, T., Muthuswamy, E., Kamali-Moghaddam, S., Tu, C., Louie, A., & Kauzlarich, S. (2012). Development of Iron-Doped Silicon Nanoparticles As Bimodal Imaging Agents. *ACS Nano*, *6*, 5596–5604. https://doi.org/10.1021/nn301536n

Sobiyi, K., & Akinlabi, E. (2017). Microstructural Investigation Of Ti Coating On Ti6al4v By Laser Cladding. *Materials Today: Proceedings*, *4*(2), 244–249. https://doi.org/10.1016/j.matpr.2017.01.018

Srinivasulu, T., Saritha, K., & Reddy, K. T. R. (2017). Synthesis and characterization of Fe-doped ZnO thin films deposited by chemical spray pyrolysis. *Modern Electronic Materials*, *3*(2), 76–85. https://doi.org/10.1016/j.moem.2017.07.001

Srivastava, A., Kumar, N., & Khare, S. (2014). Enhancement in UV emission and band gap by Fe doping in ZnO thin films. *Opto-Electronics Review*, *22*(1). https://doi.org/10.2478/s11772-014-0179-x

Suchea, M., Christoulakis, S., Katharakis, M., Vidakis, N., & Koudoumas, E. (2009). Influence of thickness and growth temperature on the optical and electrical properties of ZnO thin films. *Thin Solid Films*, *517*(15), 4303–4306. https://doi.org/10.1016/j.tsf.2008.11.143

Sun, X., Song, L., Liu, N., Shi, J., & Zhang, Y. (2021). Chromium-Doped Zinc Gallate Near-Infrared Persistent Luminescence Nanoparticles in Autofluorescence-Free Biosensing and Bioimaging: A Review. *ACS Applied Nano Materials*, *4*(7), 6497–6514. https://doi.org/10.1021/acsanm.1c01115

Sun, Y., Zhang, W., Li, Q., Liu, H., & Wang, X. (2023). Preparations and applications of zinc oxide based photocatalytic materials. *Advanced Sensor and Energy Materials*, *2*(3), 100069. https://doi.org/10.1016/j.asems.2023.100069

Taunk, P. B., Das, R., Bisen, D. P., & Tamrakar, R. K. (2015). Structural characterization and photoluminescence properties of zinc oxide nano particles synthesized by chemical route method. *Journal of Radiation Research and Applied Sciences*, *8*(3), 433–438. https://doi.org/10.1016/j.jrras.2015.03.006

Teodorescu, M., Bercea, M., & Morariu, S. (2018). Biomaterials of Poly(vinyl alcohol) and Natural Polymers. *Polymer Reviews*, *58*(2), 247–287. https://doi.org/10.1080/15583724.2017.1403928

Thakur, D., Wu, J.-R., Chandel, A., Cheng, K.-J., Chiang, S.-E., Cai, K.-B., Chen, S.-H., Yang, C.-C., Zhong, Y.-L., Yuan, C.-T., Shen, J.-L., & Chang, S. H. (2021). Structural, optical and excitonic properties of urea grading doped CH3NH3PbI3 thin films and their application in inverted-type perovskite solar

cells. *Journal of Alloys and Compounds*, *858*, 157660. https://doi.org/10.1016/j.jallcom.2020.157660

Tsay, C.-Y., & Huang, T.-T. (2013). Improvement of physical properties of IGZO thin films prepared by excimer laser annealing of sol–gel derived precursor films. *Materials Chemistry and Physics*, *140*(1), 365–372. https://doi.org/10.1016/j.matchemphys.2013.03.051

Üzar, N. (2025). Effect of 15% Fe doping on the structural, optical, electrical, and thermoelectric properties of ZnO thin films. *Physica B: Condensed Matter*, *704*, 417045. https://doi.org/10.1016/j.physb.2025.417045

Vanheusden, K., Warren, W. L., Seager, C. H., Tallant, D. R., Voigt, J. A., & Gnade, B. E. (1996). Mechanisms behind green photoluminescence in ZnO phosphor powders. *Journal of Applied Physics*, *79*(10), 7983–7990. https://doi.org/10.1063/1.362349

Verma, D., Kole, A. K., & Kumbhakar, P. (2015). Red shift of the band-edge photoluminescence emission and effects of annealing and capping agent on structural and optical properties of ZnO nanoparticles. *Journal of Alloys and Compounds*, *625*, 122–130. https://doi.org/10.1016/j.jallcom.2014.11.102

Vishwakarma, A. (2020). Synthesis of Zinc Oxide Nanoparticle by Sol-Gel Method and Study its Characterization. *International Journal for Research in Applied Science and Engineering Technology*, *8*(4), 1625–1627. https://doi.org/10.22214/ijraset.2020.4265

Viswanathamurthi, P., Bhattarai, N., Kim, H. Y., & Lee, D. R. (2003). The photoluminescence properties of zinc oxide nanofibres prepared by electrospinning. *Nanotechnology*, *15*(3), 320. https://doi.org/10.1088/0957-4484/15/3/015

Vorontsov, A. V., & Tsybulya, S. V. (2018). Influence of Nanoparticles Size on XRD Patterns for Small Monodisperse Nanoparticles of Cu^0 and TiO_2 Anatase. *Industrial & Engineering Chemistry Research*, *57*(7), 2526–2536. https://doi.org/10.1021/acs.iecr.7b04480

Wang, J., Lee, J. S., Kim, D., & Zhu, L. (2017). Exploration of Zinc Oxide Nanoparticles as a Multitarget and Multifunctional Anticancer Nanomedicine. *ACS Applied Materials & Interfaces*, *9*(46), 39971–39984. https://doi.org/10.1021/acsami.7b11219

Wiengnon, S., & Anuragudom, P. (2019). Synthesis, and characterization of Iron-doped Zinc Oxide nanoparticles; Influence of drying. *Materials Today: Proceedings*, *17*, 1479–1486. https://doi.org/10.1016/j.matpr.2019.06.171

Winarsih, S., Jatmika, J., Roza, L., Risdiana, R., & Watanabe, I. (2024). Effect of cobalt and aluminum doping on the structural and magnetic properties of zinc oxide nanoparticles. *AIP Advances*, *14*(4), 045044. https://doi.org/10.1063/5.0181275

Yadav, M. S., Singh, N., & Kumar, A. (2018). Synthesis and characterization of zinc oxide nanoparticles and activated charcoal based nanocomposite for supercapacitor electrode application. *Journal of Materials Science: Materials in Electronics*, *29*(8), 6853–6869. https://doi.org/10.1007/s10854-018-8672-5

Yang, Z., Lyu, J., Qian, J., Wang, Y., Liu, Z., Yao, Q., Chen, T., Cao, Y., & Xie, J. (2025). Glutathione: A naturally occurring tripeptide for functional metal nanomaterials. *Chemical Science*, *16*(16), 6542–6572. https://doi.org/10.1039/D4SC08599J

Yu, F., Hu, H., Wang, B., Li, H., Song, T., Xu, B., He, L., Wang, S., & Duan, H. (2019). Effects of Al doping on defect behaviors of ZnO thin film as a photocatalyst. *Materials Science-Poland*, *37*(3), 437–445. https://doi.org/10.2478/msp-2019-0050

Yu, X., Meng, D., Liu, C., Xu, K., Chen, J., Lu, C., & Wang, Y. (2014). Enhanced photocatalytic activity of Fe-doped ZnO nanoparticles synthesized via a two-step sol–gel method. *Journal of Materials Science: Materials in Electronics*, *25*(9), 3920–3923. https://doi.org/10.1007/s10854-014-2107-8

Zak, A. K., Majid, W. H. Abd., Darroudi, M., & Yousefi, R. (2011). Synthesis and characterization of ZnO nanoparticles prepared in gelatin media. *Materials Letters*, *65*(1), 70–73. https://doi.org/10.1016/j.matlet.2010.09.029

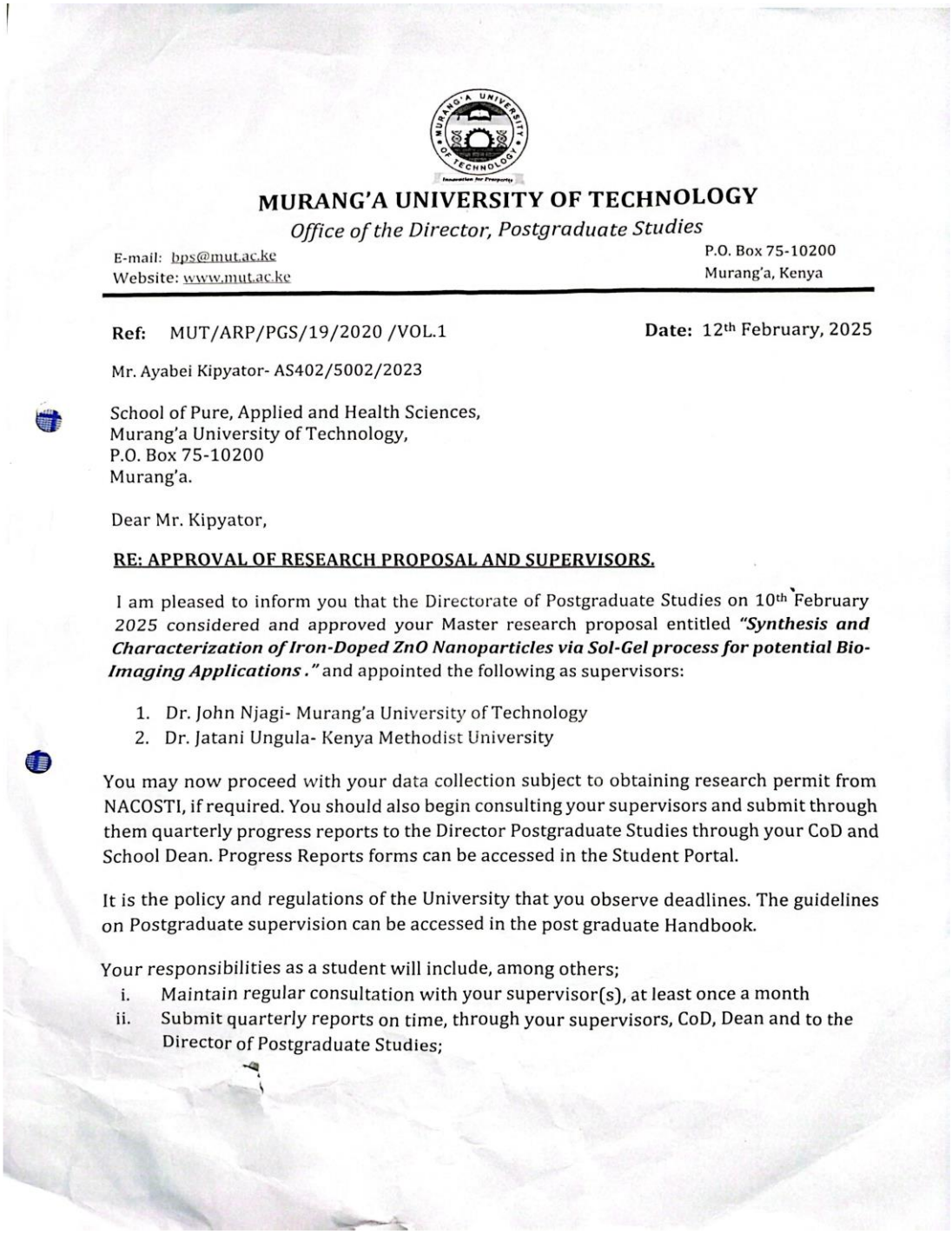
Zhang, C., Yan, L., Wang, X., Zhu, S., Chen, C., Gu, Z., & Zhao, Y. (2020). Progress, challenges, and future of nanomedicine. *Nano Today*, *35*, 101008. https://doi.org/10.1016/j.nantod.2020.101008

Zheng, Y., Gao, S., & Ying, J. Y. (2007). Synthesis and Cell-Imaging Applications of Glutathione-Capped CdTe Quantum Dots. *Advanced Materials*, *19*(3), 376–380. https://doi.org/10.1002/adma.200600342

Zhu, P., Weng, Z., Li, X., Liu, X., Wu, S., Yeung, K. W. K., Wang, X., Cui, Z., Yang, X., & Chu, Paul. K. (2016). Biomedical Applications of Functionalized ZnO Nanomaterials: From Biosensors to Bioimaging. *Advanced Materials Interfaces*, *3*(1), 1500494. https://doi.org/10.1002/admi.201500494

APPENDICES

Appendix 1: Research Authorization



MURANG'A UNIVERSITY OF TECHNOLOGY

Office of the Director, Postgraduate Studies

E-mail: bps@mut.ac.ke
Website: www.mut.ac.ke

P.O. Box 75-10200
Murang'a, Kenya

Ref: MUT/ARP/PGS/19/2020 /VOL.1 **Date:** 12th February, 2025

Mr. Ayabei Kipyator- AS402/5002/2023

School of Pure, Applied and Health Sciences,
Murang'a University of Technology,
P.O. Box 75-10200
Murang'a.

Dear Mr. Kipyator,

RE: APPROVAL OF RESEARCH PROPOSAL AND SUPERVISORS.

I am pleased to inform you that the Directorate of Postgraduate Studies on 10th February 2025 considered and approved your Master research proposal entitled ***"Synthesis and Characterization of Iron-Doped ZnO Nanoparticles via Sol-Gel process for potential Bio-Imaging Applications."*** and appointed the following as supervisors:

1. Dr. John Njagi- Murang'a University of Technology
2. Dr. Jatani Ungula- Kenya Methodist University

You may now proceed with your data collection subject to obtaining research permit from NACOSTI, if required. You should also begin consulting your supervisors and submit through them quarterly progress reports to the Director Postgraduate Studies through your CoD and School Dean. Progress Reports forms can be accessed in the Student Portal.

It is the policy and regulations of the University that you observe deadlines. The guidelines on Postgraduate supervision can be accessed in the post graduate Handbook.

Your responsibilities as a student will include, among others;

i. Maintain regular consultation with your supervisor(s), at least once a month
ii. Submit quarterly reports on time, through your supervisors, CoD, Dean and to the Director of Postgraduate Studies;

iii. Ensure quality work all through;
iv. Present your research findings at 2-3 seminars/conferences prior to thesis examination.
v. Publish one article from your research findings in a refereed journal prior to thesis examination.

For any further clarification please contact the undersigned.

Yours Sincerely,

Prof. Geoffrey Muchiri, PhD
Director, Postgraduate Studies
CM/MMK

DIRECTORATE OF POSTGRADUATE STUDIES
MURANG'A UNIVERSITY OF TECHNOLOGY
27 MAR 2025
P. O. Box 75 - 10200, MURANG'A
Tel: 0771403515, Email: info@mut.ac.ke

Copy to:
1. Registrar – Academics and Students Affairs
2. Dean, School of Pure, Applied and Health Sciences

Appendix 2: Publications

The following papers have been published from this thesis.

Ayabei, S., Njagi, J., Ungula, J., & Kiprotich, S. (2025). Effects of glutathione concentration used as a capping agent on the structural, optical, and photoluminescence properties of Fe: ZnO NPs. American Journal of Condensed Matter Physics, 14(1), 8–17. https://doi.org/10.5923/j.ajcmp.20251401.02

Ayabei, S., Kiprotich, S., Njagi, J., & Ungula, J. (2025). Effects of varying growth temperature on optical and structural properties of iron-doped zinc oxide nanoparticles. Nanoscience and Nanotechnology, 14(1), 1–8. https://doi.org/10.5923/j.nn.20251401.01